Print ISSN 0033-9008
Online ISSN 1880-1765

QUARTERLY REPORT of RTRI

Aug. 2023 Vol. 64 No. 3

CONTENTS

RAILWAY TECHNICAL RESEARCH INSTITUTE

QUARTERLY REPORT of RTRI

Print ISSN 0033-9008
Online ISSN 1880-1765

August 2023 Vol. 64 No. 3

CONTENTS

Research and Development Trends Related to Vehicle Technology at RTRI

Makoto ISHIGE
Vehicle Technology Division

In the organizational reform of RTRI on April 1, 2022, Vehicle Structure Technology Division and Vehicle Control Technology Division were merged into a new Vehicle Technology Division. The aim of this new division is to respond efficiently and promptly to the increasing sophistication and diversification of needs, such as the application of digital technology in vehicle technology, response to decarbonization, and overseas expansion including international standards. To this end, this division is conducting research and development by integrating mechanical and electrical systems. This paper gives an overview of the status of recent activities related to vehicle technology at RTRI.

Key words**:** *vehicle technology, driving safety, decarbonization, anomaly detection, ride comfort*

1. Introduction

The Railway Technical Research Institute (RTRI) was restructured on April 1, 2022. The Vehicle Structure Technology Division and Vehicle Control Technology Division, which were previously in charge of vehicle-related research and development, were integrated to establish the Vehicle Technology Division. Mechanical and electrical systems, which were previously separated into two research divisions, now work together in research and development in order to respond to the sophistication and diversification of needs efficiently and promptly, such as the application of digital technology in vehicle technology, response to decarbonization, and expansion into overseas fields including international standards.

In this paper, an overview is given of vehicle technology initiatives for each of the R&D goals of RESEARCH 2025, which are safety improvement, cost reduction, harmony with the environment, and improvement of convenience.

2. Safety improvement

2.1 Running safety evaluation

The evaluation of running safety against derailment of a new line or new vehicle type is conducted by attaching a strain gauge to a dedicated wheel, measuring the wheel load and lateral force, and using the derailment coefficient (lateral force / wheel load), but the preparation of the wheelsets and installation on the bogie are costly and require labor, so a simple running safety evaluation method is needed. One such method that is under investigation involves estimating wheel load and lateral force using bogie motion data that could be measured by inertial measurement devices and displacement sensors [1].

The problem with the conventional method for measuring wheel load and lateral force is that the lateral force measurement accuracy can decrease when the contact position shifts in the lateral direction. Therefore, instead of the conventional method, where the lateral force is measured using the bending strain on the side surface of the wheel, the proposed method involves reducing the effect of the wheel load by using the shear strain inside the wheel load measurement holes as a measure of lateral force [2].

When evaluating running safety, the derailment coefficient may exceed the evaluation criteria, but this does not necessarily lead to derailment. Therefore, a new evaluation indicator for running safety is proposed that considers the time-series history of the derailment coefficient. This may allow more accurate evaluation of the safety margin against flange climb derailment [3]. We have also proposed a flange climb derailment evaluation method that evaluates both the derailment coefficient and amount of wheel rise [4].

Furthermore, new processing equipment and slip-ring equipment are being developed since the equipment for the new continuous wheel/rail contact force measurement method, which conducts arithmetic processing on the strain gauge output and conducts continuous measurements, is obsolete [5].

2.2 Running stability evaluation [6, 7]

When evaluating the high-speed running stability of a vehicle, a hunting motion test is conducted in order to determine the critical hunting speed using a rolling stock test stand. It is empirically known that the critical hunting speed can vary depending on the excitation mode, and results of evaluating the effect of the difference in excitation method on the critical hunting speed showed that there is a critical hunting curve that expresses the relationship between the initial lateral amplitude of wheelsets after excitation and the speed led to hunting. A method is being developed to efficiently obtain the critical hunting curve through analysis.

2.3 Longitudinal vibration of train set [8]

The force acting on the coupler between vehicles in the train set (i.e., coupler force) is a key parameter for trainset buckling. Meanwhile, the transmission of longitudinal vehicle vibration through the coupler also affects ride comfort, so the numerical analysis method for the coupler force was expanded to create an analysis model for the longitudinal vibration acceleration of the carbody when varying driving force was applied due to re-adhesion control and other factors. This analysis model could be used in the design of traction control systems that consider the longitudinal vibration of the carbody caused by torque fluctuations.

2.4 Non-destructive inspection

Applications of the phased-array ultrasonic testing method, which visualizes the results of flaw detection as a cross-sectional image was investigated for ultrasonic flaw detection. The flaw de-

tection performance was verified when the phased-array ultrasonic testing method was applied to steel sheets, and the results showed that it was superior to the conventional flaw detection method when detecting inclined flaws [9].

2.5 Crashworthiness

In Japan, no indices have been specified for evaluating collision scenarios or vehicle crashworthiness. Therefore, the collision scenarios based on previous examples of level-crossing accidents were set, collision analysis and passenger injury analysis were conducted to verify the correlation between vehicle impact deceleration and passenger injury value, and an evaluation method was proposed for vehicle crashworthiness [10].

2.6 Train fire

Understanding the characteristics of fires in vehicles is important for developing measures to ensure safe passenger evacuation and prevent vehicle structures causing damage or injury in the event of a train fire. As a basic examination of this, assuming a fire in a vehicle cabin was assumed, combustion tests were conducted in order to understand the combustion characteristics of combustible materials and the scale of the fire source, and a reproduction analysis of the combustion test was conducted using a computational fluid dynamics code [11].

2.7 Brake control

In order to stabilize brake distance, deceleration control was improved: the deceleration of the train is fed back into the current braking system in order to follow a fixed target value, and a distance-based deceleration control, where a function was added to successively update the deceleration target value based on the braking distance, was proposed. Results of running tests confirmed that the braking distance accuracy was high even when the braking force was intentionally reduced. Future studies will investigate how speed accuracy influences control performance as well as aim for control stabilization, with the ultimate goal of practical use [12].

3. Harmony with the environment

3.1 Decarbonization

Contributing to a sustainable society requires diversification of energy sources for railway vehicles, and research and development of fuel cell hybrid trains is being conducted. Fuel cell and storage battery output has been increased and main circuit systems have been made smaller in order to improve the acceleration performance to that of an electric train and securing passenger space. Future tasks include sophistication of power flow control and energy evaluations such as those for fuel consumption and efficiency through simulated route driving using a rolling stock test stand [13].

3.2 EMC

There are many combinations of signal devices and inverter devices, which makes it difficult to predict the results of radiative emission tests, which is one of the final inspections of railway vehicles. Therefore, a method was created in which quantitative modeling of the effect of radiative emission on the signal device was conducted, and measurements and comparisons of the upper limit of leakage current in the combination test of the inverter and motor before completing the vehicle were conducted in order to enable advance confirmation of radiative emission testing [14].

3.3 Noise

One measure to reduce the fluctuating force caused by gear meshing, which is thought to be the main vibration source of gear noise in the driving device, is optimization of the shape of the gear contact surface, but this has the disadvantage of increasing processing costs. Therefore, a gear is being developed that uses high-strength ferrum casting ductile, which has high damping performance and good conformability of tooth surface, in order to omit the final gear grinding process, which accounts for a large part of the manufacturing cost, and this has resulted in a significant reduction in noise when using actual gears [15].

4. Cost reduction

4.1 Battery degradation prediction method [16]

Securing the reliability of lithium-ion batteries that are used for the drive and control circuits of railway vehicles requires accurately predicting degradation and replacing them at the appropriate time. A capacity prediction formula that considers battery temperature fluctuations under actual usage conditions was proposed in order to predict degradation with high accuracy, and an accelerated aging test using an actual battery confirmed that the battery capacity and internal resistance could be predicted with a high accuracy over long periods of time. In the future, a prediction method will be investigated for cycle degradation that cannot be ignored in drive applications.

4.2 Anomaly detection method

There have been active initiatives related to anomaly detection of vehicle equipment. Detecting anomalies requires capturing some kind of physical quantity, and if there are existing sensors for the operation and control of equipment, then that data could be used. One example of these initiatives includes the proposal of a method for automatically judging anomalies from vehicle condition monitoring data using deep learning techniques. Results of attempts to apply this to engine stop events and engine overheating events of diesel railcars showed that it was possible to determine the anomaly before the event occurred [17].

One initiative to detect anomalies by adding or temporarily installing sensors to acquire physical quantities is the development of a condition monitoring methods that combine octave band analysis of vibration and machine learning. One case study is the detection of the occurrence of anomalous vibrations due to anomalous internal wear that is caused by foreign bodies entering the hydraulic torque converter. Results of anomaly simulation tests confirmed that an anomaly could be detected in a high-frequency band regardless of the concentration of foreign bodies, and that an anomaly could be detected regardless of the vibration measurement point [18]. Another case study is the anomaly diagnosis of traction motor bearings, where it was confirmed in stationary tests after applying to the leakage current of traction motors instead of bearing vibration that anomalies in bearings could be detected under specific no-load conditions [19].

4.3 Evaluation of friction material properties

Implementation of full-scale bench tests is essential when evaluating the final performance of brake friction materials, but when focusing on the evaluation of friction materials at high temperatures, it can be seen that the tests require a large amount of time and effort. Therefore, a method that experimentally investigated and analyzed the relationship between the thermal change of the solid lubricant contained in the friction material and friction coefficient and where the heat resistance of the base material was evaluated was proposed as a simple method for evaluating friction materials [20]. In the future, this will be used as a basic test for selecting friction materials in the brake friction material development process.

5. Improved convenience

5.1 Improved ride comfort

5.1.1 Carbody tilting control

In order to reduce motion sickness in a controlled natural tilting vehicle, the target pattern of tilt angle that matches the shape of the actual curve instead of the conventional step pattern, and a tilting control actuator that can achieve it, has been in development [21]. Furthermore, a train positioning system that uses track curvature collation instead of the positioning system based on the conventional ATS beacon and the tachometer generator cumulative distance has been in development [22], and these were combined to construct a tilting control system. There are plans to install them in actual vehicles in the future, and they are expected to improve the ride comfort of the tilting vehicle.

Additionally, a tilt control system with the active torsion bar has been developed as a new carbody tilting mechanism [23]. This achieves tilting performance that is comparable to that of a tilting bogie with a bogie configuration that is almost the same as a general bogie, with good tilting control performance and safety in the event of actuator failure verified in bench tests. Its performance is expected to be confirmed in actual vehicles.

5.1.2 Vertical vibration reduction control system

Shinkansen trains have become much more comfortable in the lateral direction than in the past, and passengers tend to feel more vibration in the vertical direction than in the lateral direction. Reducing the vertical vibration of the car body is thought to be an effective way for improving ride comfort. Therefore, a vertical vibration reduction control system has been in development that combines variable hydraulic vertical dampers in primary and secondary suspension. A single-vehicle test using rolling stock test stand confirmed that vibrations in the vertical rigid body mode, vertical flexural mode, and roll mode could be reduced simultaneously, and that the ride comfort could be improved [24].

5.1.3 Reduction of carbody elastic vibration

Carbody elastic vibration needs to be reduced in order to further improve the ride comfort of railway vehicles. An extended box model that could handle elastic vibration accompanied by three-dimensional deformed shape of the carbody and a method for mechanically and efficiently determining the parameters in this model by using particle swarm optimization have been proposed in order to efficiently investigate vibration reduction methods [25].

Specific methods for reducing vibration include not only the previously mentioned vertical vibration reduction control system but also methods that use active mass dampers [26] and methods that use elastically supported mass of underfloor equipment as a dynamic vibration absorber [27].

5.1.4 Interior noise reduction

Interior noise in railway vehicles is generated by structure-borne sound and transmitted sound. For structure-borne sound, floating floor structures have been put to practical use in order to reduce floor plate vibration, but there are problems in the low-frequency range. Therefore, a structure was developed in which the floor plates were suspended from the side structure, which is less prone to vibration (i.e., suspended floor structure), and stationary vibration tests confirmed the vibration reduction effect of floor plates in the frequency range of several hundred Hz or less [28].

5.2 Increased speed

5.2.1 Active bogie-steering system

In order to achieve both high-speed running stability and curving performance, an active bogie-steering system was developed that functions as a yaw damper when running at high speeds and acts as an actuator when running on sharp curves in order to generate a yaw moment between the carbody and the bogie. Running tests on test track confirmed that it reduced the lateral force, and running tests using rolling stock test stand confirmed that it did not affect the high-speed running stability [29].

5.2.2 Brake disk

Laser metal deposition welding, which enables the formation of heat resistant layers, was applied to the friction surface in order to improve the heat resistance of forged steel brake disks. Bench tests of a full-scale disk confirmed that it had higher high-temperature strength and improved wear resistance than the currently used disk [30].

6. Conclusion

This paper introduced recent vehicle-related research and development initiatives from RTRI. Future tasks include aiming to combine mechanical and electrical research and development to achieve safer and more comfortable railway vehicles, achieve decarbonization through more efficient railway systems, achieve reduced maintenance labor through the application of digital technologies.

References

[1] Iida,T., “Method for evaluating running safety of railway vehicle by measuring bogie motion,” *RTRI Report*, Vol. 34, No. 5, pp. 23-28, 2020 (in Japanese).

[2] Hondo, T., Kuniyuki, S., Tanaka, T., Suzuki, M., “Method for Measuring Lateral Force Utilizing Shear Strains inside Wheel Load Measuring Holes of Instrumented Wheelset,” *QR of RTRI*, Vol. 63, No. 2, pp. 139-144, 2022.

[3] Doi, H., Ishida, H., Miyamoto, T., “Running Safety Assessment for Flange climbing at Low Speeds based on Derailment Quo-

tient and Wheel Rise," *RTRI Report*, Vol. 34, No. 8, pp. 29-34, 2020 (in Japanese).
[4] Nakahashi, J., Sannomiya, D., Fukumura, M., "Evaluation Method of the Flange Climb Derailment Considering the Wheel Rise," *RTRI Report*, Vol. 33, No. 3, pp. 5-10, 2019 (in Japanese).
[5] Suzuki, M., Totake, T., Hondou, T., Kuniyuki, S., "Development of Measuring System for Wheel and Rail Contact Forces to be Realized Labor Saving of Operation, Using Commercial Measurement Instrument," *RTRI Report*, Vol. 33, No. 8, pp. 17-22, 2019 (in Japanese).
[6] Yamanaga, Y., Kido, K., "Influence of Excitation Condition on Evaluating Critical Hunting Speed," *QR of RTRI*, Vol. 60, No. 2, pp. 97-102, 2019.
[7] Yamanaga, Y., "Analysis of Hunting Stability Using Method for Calculating Periodic Solution," *RTRI Report*, Vol. 36, No. 2, pp. 5-10, 2022 (in Japanese).
[8] Sakamoto, Y., Yamashita, M., "Analysis of Longitudinal Vibration in Train Sets Caused by Tractive Force Variation," *QR of RTRI*, Vol. 62, No. 1, pp. 28-33, 2021.
[9] Makino, K., "Comparative Analysis between Conventional and Phased-array testing in Ultrasonic Inspection of Inclined Surface Flaws on Steel Plates," *Welding Technology*, Vol. 41, No. 10, 2021 (in Japanese).
[10] Okino, T., Nagata, K., Nakai, K., Kobayashi, H., "Evaluation Method for Crashworthiness Using Integrated Value of Deceleration of Railway Vehicles Showing High Correlation with Degree of Passenger Injury," *QR of RTRI*, Vol. 62, No. 3, pp. 185-190, 2021.
[11] Takano, J., Ishizuki, M., Yamauchi, Y., Yamanaka, S., Toyohara, T., "Combustion Tests on Train Seats and Reproduction Analysis," presented at the *J-Rail2019*, Tokyo, Japan, December 4-6, 2019, S6-4-4 (in Japanese).
[12] Nakazawa, S., "Accuracy Improvement of Braking Distance by Deceleration Feedback Function Applying to Brake System," *QR of RTRI*, Vol. 62, No. 3, pp. 167-172, 2021.
[13] Ogawa, K., Yoneyama, T., Sudo, T., Kashiwagi, T., Yamamoto, T., "Performance Improvement of Fuel Cell Hybrid Powered Test Railway Vehicle," *QR of RTRI*, Vol. 62, No. 1, pp. 16-21, 2021.
[14] Hatsukade, S., "Development of Pre-test for Electromagnetic Emission from Traction Inverters on Railway Vehicles," *RTRI Report*, Vol. 35, No. 8, pp. 41-46, 2021 (in Japanese).
[15] Sasakura, M., "Performance Evaluation of Low Noise Gears Using H-FCD," *RTRI Report*, Vol. 34, No. 5, pp. 17-22, 2020 (in Japanese).
[16] Taguchi, Y., Kadowaki, S., Yoshikawa, G., "Degradation Prediction Method for Lithium-Ion Battery for Railway Vehicle Considering Temperature Variation," *RTRI Report*, Vol. 36, No. 2, pp. 29-34, 2022 (in Japanese).
[17] Yokouchi, T., Takashige, T., Kondo, M., "Anomaly Detection for Railway Vehicle Equipment Using Condition Monitoring Data," *QR of RTRI*, Vol. 63, No. 4, pp. 238-243, 2022.
[18] Takashige, T., Sakaidani, Y., Yamamoto, S., Yokouchi, T., "Verification of Abnormal Wear Condition Monitoring Method Using Vibration of Transmission," *RTRI Report*, Vol. 34, No. 12, pp. 17-22, 2020 (in Japanese).
[19] Sakaidani, Y., Kondo, M., Takahashi, K., "Fault Detection for Railway Traction Motor Bearing through Leakage Current," *QR of RTRI*, Vol. 60, No. 4, pp. 256-261, 2019.
[20] Nishimori, H., Karino, Y., Tsuji, T., Sakai, S., "Heat Resistance Effect Evaluation Method of Copper-based Sintered Alloy Base Material on Friction Coefficient," *QR of RTRI*, Vol. 63, No. 2, pp. 88-94, 2022.
[21] Ishiguri, K., Kazato, A., Gejyo, T., Ajioka, M., Kubo, H., "Pneumatic Actuator for Pendulum Type Tilting Railway Vehicle that Combines Responsiveness and Stability," presented at the *Spring Fluid Power System Lecture 2022*, online, Japan, May 26-27, 2022(in Japanese).
[22] Harada, K., Maki, Y., Ishiguri, K., Kazato, A., "Development of Train Positioning System Using Track Curvature Collation Applied with Spatial Filtering," *QR of RTRI*, Vol. 61, No. 3, pp. 178-183, 2020.
[23] Kazato, A., Kojima, T., "Tilt Control Mechanism with Rotary Actuator and Anti-roll Bar," *QR of RTRI*, Vol. 60, No. 4, pp. 249-255, 2019.
[24] Sugahara, Y., Sannomiya, D., Miyahara, K., Amano, A., "Suppression of Vertical Vibrations in Railway Vehicles Using Variable Primary and Secondary Hydraulic Dampers," presented at the *J-Rail2021*, Tokyo, Japan, December 1-3, 2021, SS1-3-3, No. 21-72 (in Japanese).
[25] Akiyama, Y., Takigami, T., Aida, K., "Parameter Determination Method of Three-dimensional Analytical Models for Elastic Vibration of Railway Vehicle Carbodies," *QR of RTRI*, Vol. 62, No. 1, pp. 22-27, 2021.
[26] Akiyama, Y., Takigami, T., Makita, Y., "Method for Reducing Vibration Generated by Rotating Machinery of Railway Vehicle Carbody Using an Active Mass Damper," *RTRI Report*, Vol. 35, No. 8, pp. 29-34, 2021 (in Japanese).
[27] Aida, K., Takigami, T., Akiyama, Y., "Verification of Reduction Effect of Vertical Vibration of Car-body by High-damping Elastic Support of Under-floor Equipment," *QR of RTRI*, Vol. 63, No. 4, pp. 251-256, 2022.
[28] Goto, T., Yamamoto, K., Asahina, M., "Suspended Floor Structure for Reducing Structure-borne Sound of Interior Noise," *QR of RTRI*, Vol. 59, No. 1, pp. 29-36, 2018.
[29] Kojima, T., Umehara, Y., Hondo, T., "Development of Active Bogie Steering System to Improve Curving Performance," *QR of RTRI*, Vol. 63, No. 2, pp. 95-100, 2022.
[30] Saga, S., Takami, H., Sakamoto, Y., "Development of Braking System to Cope with Increased Speed of Shinkansen," *RTRI Report*, Vol. 35, No. 8, pp. 11-16, 2021 (in Japanese).

Author

Makoto ISHIGE
Director, Head of Vehicle Technology Division
Research Areas: Bogie Structure

R&D Activities and Future Perspectives in Material Technology

Motohide MATSUI
Materials Technology Division

Various kinds of materials are used as components of systems not only in railways but also in other industrial fields. So far, advances in material technology for structural and functional materials have contributed greatly to the development of railways. Current R&D activities mostly focus on materials with longer service life, the clarification of material deterioration mechanisms and so on. However, the pandemic of COVID-19 and rapid changes in the environment with climate change will have a significant impact on future railways. It is necessary that material technology will adapt to this drastic transition in order to keep contributing to the sustainable development of railways.

***Key words*:** *railway materials, structural materials, functional materials, material development, phenomenon elucidation, deterioration state analysis*

1. Introduction

Materials are used for a variety of applications and purposes in the construction of not only railways but also systems. Materials can be broadly classified into structural materials that emphasize material strength and durability in order to maintain the structure of the system; and functional materials emphasizing the enhancement of electrical, magnetic, optical, mechanical, and other properties in order to impart new properties through the generation of characteristic functions. The characteristics required for structural materials and functional materials are generally trade-offs with each other and are often difficult to achieve simultaneously. Hence, for example, when imparting new functionality to a structural material, it is necessary to investigate the feasibility of imparting the desired functionality by applying surface treatment to the necessary parts.

Focusing on railways, use of the following materials is distinguished according to structural and functional requirements and purposes: metal materials such as steel, aluminum, and copper; inorganic materials such as concrete and ceramics; organic materials such as rubber, paints, and lubricants; and composite materials such as carbon. It would not be an overstatement to say that these materials have developed over the 150-year long history of railways, repeatedly undergoing the challenge of resolving insufficient durability and meeting the demands for the addition of new functions. However, the environment surrounding railways in recent years has changed significantly compared to the past due to workforce shortage caused by population decline, changes in the working environment due to the novel coronavirus disease (COVID-19) pandemic, and digital technology innovations. Additionally, starting with the Paris Agreement that was adopted in COP21 in December 2015, the realization of carbon neutrality has been advocated for climate change measures, which are one of the Sustainable Development Goals (SDGs). It is expected that the knowledge and experience cultivated over multiple years may not be able to respond to such changes in the surrounding environment, and it is thought that future materials technology will be required to adapt in a flexible manner and with a willingness to take on new challenges.

In this paper, recent efforts in the field of materials technology will be introduced, mainly the research and development of new materials, elucidation of the deterioration mechanism of structural materials, methods for evaluating the evolution of deterioration, and countermeasures against damage and deterioration using functional materials. Such topics are introduced along with future prospects.

2. Research and development of recent materials

The Railway Technical Research Institute (RTRI) has conducted research and development on a variety of topics such as vehicles, tracks, electric power, signal communication, and civil engineering structures. Additionally, the properties of materials used in railways often deteriorate and change during the period of service, so methods to quantitatively evaluate the state of the material at that point in time, elucidation of the deterioration mechanism based on that evaluation method, and countermeasures using new materials have been examined, with the aim of providing on-site feedback at railways. Several of these methods are introduced here.

2.1 Development of Shinkansen axle bearing oil for cold regions [1]

A bearing is a member that supports a rotating wheelset on both sides, with the inside of the bearing lubricated with oil or the like. As the Shinkansen route network has expanded to cold regions, there were concerns that the current oil would lose its fluidity at low temperatures. In order to resolve this problem, synthetic oil was initially used to improve low-temperature fluidity. However, its red discoloration over time made it difficult for on-site workers to judge the soundness of the oil, and it had become a maintenance issue (comparison oil). Therefore, as shown in Fig. 1, additives were adjusted based on highly refined mineral oil in order to develop a Shinkansen axle bearing oil where red discoloration due to aging and maintenance issues were avoided, while ensuring low-temperature fluidity.

Figure 2 shows the low-temperature fluidity of the developed oil. A lower pour point shown on the vertical axis of the figure indicates a higher fluidity at low temperatures. It was shown that, compared to the current bearing oil, the developed oil had fluidity even at temperatures below -40°C. Results of laboratory tests using actual axle bearing also showed that no abnormalities were found in the developed oil even after an endurance test that was equivalent to 800,000 km. Results showed good durability.

For the gear oil used in the gear system as well, a product is being developed that is suitable for cold climates, has improved low-temperature fluidity, and has improved starting acceleration;

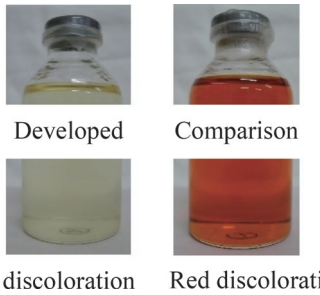

Fig. 1 Developed oil with red discoloration suppressed

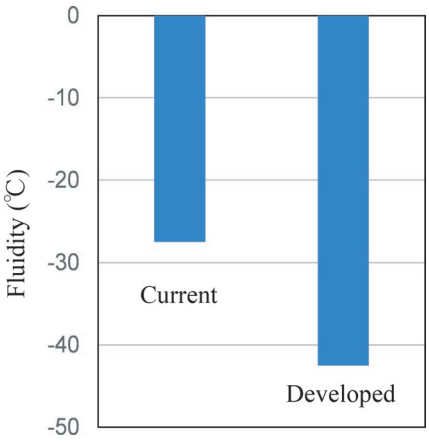

Fig. 2 Comparison of fluidity between current and developed oil

and it is thought that these results will contribute to the stable running of the Shinkansen in cold regions.

2.2 Development of repair materials using geopolymers

Compared to cement, geopolymers can not only utilize a large amount of industrial byproducts during their production, but also reduce CO_2 emissions, so they are a structural material that is expected to be an effective means of reducing the environmental load. Geopolymers are also characterized by high resistance to alkali-silica reactions, acid corrosion, etc., which are factors of cement deterioration. As shown in Fig. 3, these features were utilized to develop PC sleepers and short sleepers using geopolymers [2].

The high resistance of this material has been utilized in recent years to develop a geopolymer mortar for plastering work [3]. This is expected to be applied to places where ordinary cement mortar could not be easily repaired under corrosive environments.

2.3 Elucidation of mechanism of increased contact wire wear rate near Shinkansen pantograph stop position [4]

In the Shinkansen, the wear rate of contact wires, which are structural materials that make up the contact line equipment, is sometimes higher in low-speed sections such as near stations than in high-speed sections. This leads to an increase in the frequency of contact wire replacement, which hinders efforts to reduce maintenance costs. In order to investigate the cause of this increased wear rate, the wear distribution of contact wires in a station was investigated alongside the running speed of vehicles running in that direction. Results, shown in Fig. 4, indicated that the contact wire wear rate increased sharply as the vehicle approached the stop position

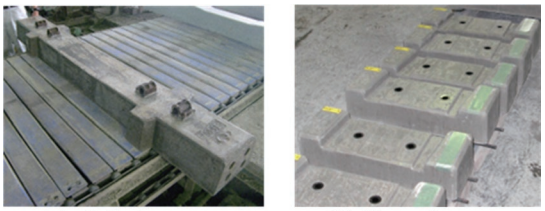

Fig. 3 Sleepers using geopolymers

and the running speed decreased. Therefore, as shown in Fig. 5, laboratory tests were conducted in order to investigate the speed dependence of the friction coefficient, where it was shown that the friction coefficient increased sharply as the speed decreased. As shown in Fig. 6, the cross-sectional metallographic observation of the contact wires after use indicated that this increase in the friction coefficient accelerated peeling wear.

Grease lubrication was tested as a lubrication method that can reduce the friction coefficient for suppressing peeling wear, where it was confirmed that the wear rate was greatly reduced, and in the future, we plan to study verification using actual equipment.

A detailed understanding of the mechanism of changes over time from initial properties such as fatigue and deterioration as well as friction, which must be considered when using materials, is thought to lead to effective countermeasures.

2.4 Concrete surface layer quality evaluation by water spray test

Reinforced concrete, which is one of the main structural materials for railways and is used in elevated bridges, etc., must not corrode the reinforcing bars that bear the tensile force. The concrete that protects these reinforcing bars must not only have a certain strength, but also a certain thickness and high resistance to water infiltration in order to prevent water penetration, which is the main cause of reinforcing bar deterioration. However, even if there are no defects in the appearance of the concrete in these parts, the finished state changes depending on the construction method. This finished state is referred to as "surface layer quality," and a water spray test method has been developed for the simple on-site evaluation of water permeation resistance, which affects surface layer quality [5].

The water spray test is a method of spraying a small amount of water on the surface of dry concrete and visually evaluating the water absorption state of the surface layer. As shown in Fig. 7, the developed water spray test method (WIST) involves using a manual

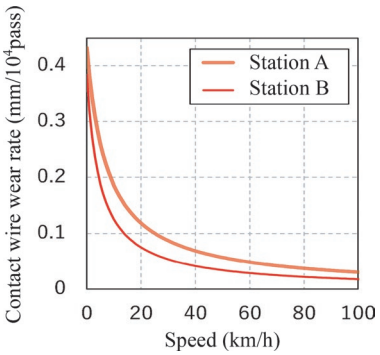

Fig. 4 Speed dependence of contact wire wear rate in Shinkansen line

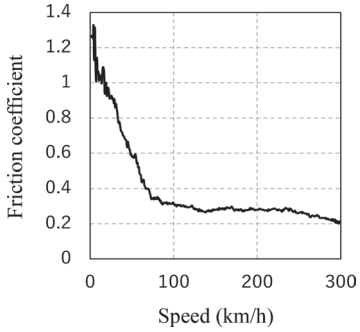

Fig. 5 Speed dependence of friction coefficient

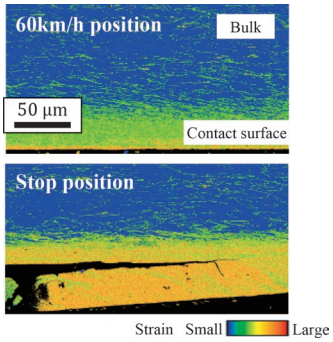

Fig. 6 Results of strain analysis of actual contact wire cross-section

sprayer to repeatedly spray small amounts of water at the same location at regular intervals. Water is sprayed in the shape shown in Fig. 7(a), and the measurement is finished when the flow of water after spraying is visually confirmed, as shown in Fig. 7(b). A denser concrete with a higher quality surface layer results in the flow of water with fewer sprays. However, since WIST was a method that was specialized for vertical members such as pillars and walls, and due to the recent increase in the need for measurements at horizontal points such as floor surfaces, a method that can be applied in these areas is being developed [6].

2.5 Examination of rail grinding amount using X-ray diffraction

Rolling fatigue occurs at the contact point (rolling surface) with the wheel on the rail as the wheel repeatedly rolls on the rail as a structural material. The accumulation of this rolling fatigue may lead to rail damage, such as shelling. One means of suppressing this rail damage involves using rail grinding vehicles to remove the surface layer that has suffered from rolling fatigue. However, although there are certain standards for this rail grinding, implementing efficient rail grinding requires understanding the fatigue state of the rail surface layer that has suffered from rolling fatigue.

Therefore, we analyzed the surface layer of the rail using X-ray diffraction (henceforth referred to as X-ray Fourier analysis). As shown in Fig. 8(a), a characteristic of the X-ray Fourier analysis is that plastic flow, in which the metal structure appears to flow in a certain direction, and refinement of the metal structure are observed near the surface of the cross-sectional metal structure of rails subjected to rolling fatigue as changes not seen in the original metal structure. The irradiation of X-rays to such changed parts yields a broader X-ray diffraction peak relative to that of an unused rail, as shown in Fig. 8(b). Quantifying this change with X-ray Fourier analysis makes it possible to evaluate the rolling fatigue state. So far, this analysis method has been applied to aged rails with no history of rail grinding, but rails with further aging have also been evaluated, and efficient rail grinding methods have been examined [7].

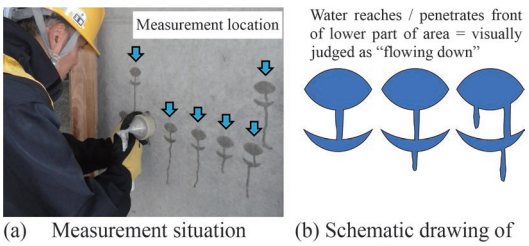

(a) Measurement situation (b) Schematic drawing of water flow

Fig. 7 Overview of water spray test

2.6 Application of diamond-like carbon (DLC) film to suppress fretting wear of axle bearings

Axle bearings used for railway vehicles are one of the vehicle component members that support the vehicle weight and maintain stable rotation of the wheelset. Fretting may occur in some of the parts of the axle bearing, which is one such component member. Fretting is damage such as wear caused by minute slippage that occurs at the contact area of two objects. In the case of axle bearings, the entry of abrasion dust that is generated by fretting into the axle bearing accelerates the wear of the bearing parts and the deterioration of the lubricating oil, etc., which becomes a problem in terms of maintenance.

Measures for suppressing this fretting wear were investigated from two directions. The first is the relaxation of the contact surface pressure at the contact part. The uneven surface pressure distribution that was generated at the contact area and the amplitude of the surface pressure due to rotation were found to be correlated with the

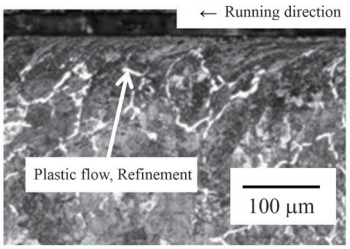

(a) Microstructure at longitudinal section subjected to rolling contact fatigue

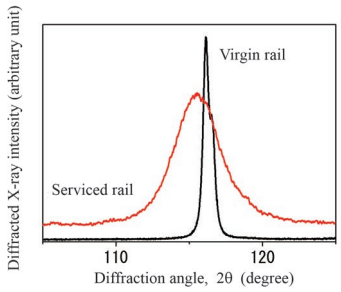

(b) Comparison between geometries of X-ray peaks

Fig. 8 Evolution in longitudinal microstructure of rail subjected to rolling fatigue and diffracted X-ray peak

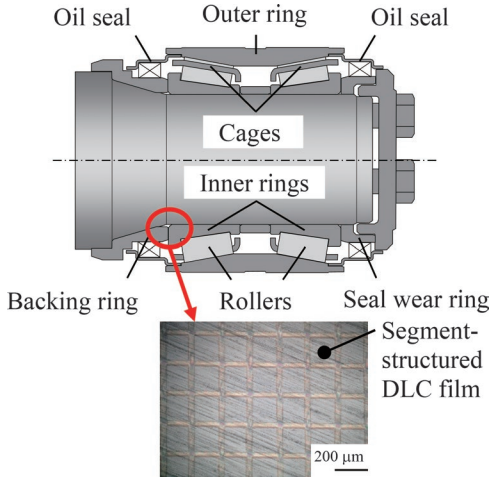

Fig. 9 Attached position of diamond-like carbon (DLC) film in axle bearing

occurrence of fretting wear, and finite element analysis and laboratory tests were conducted to develop a shape that could suppress the occurrence of fretting wear on the real axle bearings of existing axles. The second is to add a functional coating that reduces the friction coefficient to the contact area of the rear lid, as shown in Fig. 9. A segment-structured DLC film that could adhere to the rear lid and reduce the friction coefficient was investigated as a functional coating, and it was confirmed in laboratory tests using actual axle bearings that fretting wear could be suppressed [8].

3. Conclusion

Various materials are used as structural materials and functional materials in railways. Needless to say, research and development that was related to materials has contributed to the maintenance and development of railways, but high safety, reliability, durability, high functionality, etc., will continue to be required for the research and development of materials. However, it is expected that there will be an increasing need to adapt to the environment surrounding railways, which has undergone major changes in recent years, and more than ever before, an awareness of social demands such as reducing environmental impacts and being carbon neutral will be required. Furthermore, rapidly advancing digital technologies such as AI may greatly change the nature of research and development methods of materials in the future. The hope is to continue research and development so that a flexible response can be provided to these changes and continued sustainable development of railways can be achieved.

Author

Motohide MATSUI, Ph.D.
Director, Head of Materials Technology Division
Research Areas: Wheel/Rail interaction, Rolling Contact Fatigue and Wear, Track Materials

References

[1] https://www.rtri.or.jp/rd/seika/2021/1-10.html (in Japanese).
[2] https://www.rtri.or.jp/rd/seika/2012/02/02_06.html (in Japanese).
[3] Uehara, M. and Sato, T., "Development of Plastering Geopolymer Mortar," *RTRI Report*, Vol. 36, No. 11, pp. 5–10, 2022 (in Japanese).
[4] https://www.rtri.or.jp/rd/seika/2021/5-24.html (in Japanese).
[5] Nishio, S., "Influencing Factors of Water Intentional Spraying Test for the On-site Evaluation of Cover-concrete Quality," *RTRI Report*, Vol. 34, No. 10, pp. 11–16, 2020 (in Japanese).
[6] Nishio, S., "Evaluation Method for Water Penetration Resistance of Concrete Structures Applicable to Horizontal Surface," *RTRI Report*, Vol. 36, No. 11, pp. 11–16, 2022 (in Japanese).
[7] Matsui, M. and Kamiya, Y., "Evaluation of material deterioration of rails subjected to rolling contact fatigue using x-ray diffraction," *Wear*, Vol. 304, Issues 1-2, pp. 29–35, 2013.
[8] Okamura, Y., Suzuki, D., Ikoma, K. and Nagatomo, T., "Effects of Segment-structured Carbon Film on Fretting Wear Prevention of Axle Journal Bearings," *RTRI Report*, Vol. 36, No. 11, pp. 29–35, 2022 (in Japanese).

Trend on Research and Development Relating to Information and Communication Technology in Railway Fields

Mitsuyoshi FUKUDA
Information and Communication Technology Division.

In various industrial fields, innovation of systems and improvement of business operations through the use of information and communication technology, or so-called digital technology, have become urgent challenges. In railway industries, decline in the working-age population as well as changes in behavior triggered by the COVID-19 have led to unprecedented demands to save labor and lower costs. Digital technology innovation in railway systems is seen as a solution. This paper presents recent research and development using digital technology, in terms of data analytics, sensing and recognition, and information networks.

Key words**:** *digital technology, data analysis, image processing, AI, information network*

1. Introduction

System innovation and business improvement using information and communication technology are pressing issues in various industrial fields. In the railway fields, changes in behavioral patterns triggered by the COVID-19 pandemic in addition to the decline in the working-age population have resulted in increasingly stronger demands needed to save labor and reduce costs in the short term.

At the Railway Technical Research Institute (RTRI), one of the basic policies of activities in the basic plan RESEARCH 2025 is "innovation of the railway system by digital technology," which centers on research and development into labor-conserving technologies to address issues such as labor shortages at railway sites. This work concentrates, for example, on integration of information and communication technology to railways, autonomous train operations, and digital maintenance. Additionally, in April 2022, the Information and Communication Technology Division was newly established to boost cross-sectoral use of digital technology in railways. Innovation in railway systems focuses on three "cutting edge" perspectives: 1) technology which can be used to analyze data and support decision-making for maintenance, sales, and transportation services; 2) technology used to recognize and 'judge' output from sensing by cameras, LiDAR, etc., by image processing and AI, etc., in order reduce labor-intensity of maintenance and improve safety; and 3) fundamental technologies such as information networks and wireless communications that transmit and aggregate data for the use of digital technology. A total of three laboratories for Data Analytics, Image Analysis, and Telecommunications and Networking that correspond to each perspective were established. In order to obtain practical results, it is important to collaborate with technologies in each section of the railway system, so research and development is being promoted in collaboration with researchers in each section.

In this paper, recent research and development of the perspectives 1–3 mentioned above are introduced.

2. Data analysis and decision making

Regarding the maintenance of equipment, various data analysis initiatives are underway in each system since it is becoming possible to automatically measure and aggregate data from multiple locations at high frequency, and due to the evolution of data analysis technology [1, 2]. Meanwhile, there are some facilities where direct data measurement and high-frequency automatic measurements are difficult. It may also be difficult to estimate equipment deterioration tendencies with high accuracy. Therefore, research and development are being conducted of a method for data analysis using not only the measurement data of the own system but also the measurement data of other systems in order to improve the efficiency and sophistication of maintenance.

Railway operators can evaluate sales and transportation services using multiple indicators, such as transportation revenue as well as passenger convenience. Improvements in convenience may not lead directly to an increase in income, but various effects can be expected, such as stimulated demand, strengthened competitiveness with other modes of transportation, and improved corporate image. Being able to collect, analyze, and evaluate various data related to train operations, as well as being able to evaluate and propose ways to improve them, can help improve the quality of transportation services and strengthen sales capabilities.

Below, recent research and development from these two perspectives are introduced. For both perspectives, data analysis is a means to an end, and it is important to be able to produce results that contribute to decision-making, such as extending inspection intervals, changing maintenance systems, and deciding on sales strategies.

2.1 Cross-sectoral data analysis

A railway system consists of various systems such as vehicles, tracks, and electric power. The data required for maintenance is measured, aggregated, and analyzed for each system. However, facilities in different systems influence each other, and cross-sectoral analysis can be considered an effective means of improving maintenance efficiency. For example, the measurement data obtained from a vehicle is affected by the conditions of the track and power equipment, so it can be said that they are mutually influencing each other, as shown in Fig. 1 [3]. Data formats and position standards (kilometers) differ for each business system, so not only examinations of methods for standardizing these but also research on methods for integrating and analyzing data from multiple systems are being conducted [4]. For example, if it is possible to find data in the other system data that shows a similar change tendency to the main data of the own system, then if the data measurement cycle is long or if there is data loss, then the soundness may be able to be confirmed from the other system data. There are also high expectations for cross-sectoral analysis, such as the detection of signs of deteriora-

tion that could not be previously detected.

The first aim would be to show that the above-mentioned effects could be obtained by building an integrated analysis platform for cross-sectoral analysis and deepening the examination of the analysis methods.

2.2 Evaluation of sales and transportation services

Examples of research and development related to the evaluation of sales and transportation services include the evaluation of the convenience of clock-face scheduling for regional railways [5], disaster countermeasures for freight railway networks [6], and quantification of the relationship between the image of railway routes and the intention of living along the routes in urban railways [7].

A timetable in which trains depart at regular intervals is called a clock-face schedule. Reference 5 shows that the expected waiting time of passengers can be reduced by changing the schedule pattern, and that customers' evaluation of convenience could be improved by changing the schedule pattern without increasing the number of services.

Reference 6 shows a method for evaluating measures to improve the robustness of transportation services as part of formulating a business continuity plan (BCP) in the event of a disaster. The aim of this method is to enable evaluations of advance measures and recovery procedure following a disaster (e.g., which section should be prioritized for recovery) from the perspectives of the costs required for advance equipment repair (i.e., investment cost), transport volume when there are unserviceable sections after a disaster (i.e., transport volume during disruption), and the costs required for the operation of this transport volume (i.e., disaster cost).

Reference 7 involves the analysis and discussion of the results of a questionnaire survey on the relationship between the brand and image of an urban railway line and the intention of residents (i.e., intention to continue living along the line, intention to move to the line). The results were intended to be used for decision-making when formulating measures to increase and maintain the number of residents living along the railway line. At the current stage, only a qualitative image can be shown, but if this can be associated with quantitative factors that change the image, then it will be possible to use it for policies of railway operators.

Additionally, by researching and organizing candidate factors that can influence fluctuations in passenger transportation revenues, and by quantifying the causal relationship between each factor candidate and revenue fluctuations, attempts are being made to clarify the factors behind income fluctuations and their effects [8]. This is research that applies a new method called causal impact, and the aim is to estimate future transportation revenues and achieving sales measures to increase transportation revenues.

3. Sensing and recognition / judgment

To date, sensing used in the railway field has been to measure physical quantities such as voltage and displacement. It is possible to directly and indirectly measure the physical quantities necessary for equipment monitoring, so in many cases, it is possible to recognize and judge the state without advanced processing. Meanwhile, if there are many points to be measured, then it may become impractical in terms of cost and reliability. Additionally, it is often difficult to substitute simple physical quantity measurements for phenomena whose states have been judged visually.

Sensing and recognition / judgment technologies that use cameras and LiDAR are attracting attention as a way to solve this problem. These sensors can collectively acquire 2D or 3D data for the target range, so there is no need to attach a sensor to each measurement point, and information that is equivalent to that obtained by visual observation could be acquired as data. The background to the interest in these technologies is the improvement in the performance and price reduction of sensors such as cameras and LiDAR, as well as the evolution of processing technologies such as image processing and AI.

Here, recent research and development is introduced from the perspective of processing technology.

3.1 Object recognition

The main purpose of using sensors such as cameras and LiDAR is to determine the presence and type of objects. To date, it was possible to determine the presence and type of an object by embedding image processing technology and algorithms specialized for the characteristics of the object, but the use of AI has significantly improved this performance. Figure 2 shows an example of AI being used in a system that extracts registered equipment from images taken from a driver's train and classifies them by type [9]. The orange frame indicates that it has been extracted as registered equipment, and the numbers above it indicate the type of equipment and the likelihood of recognition. If training data could be created, then it can be applied to various equipment without changing the algo-

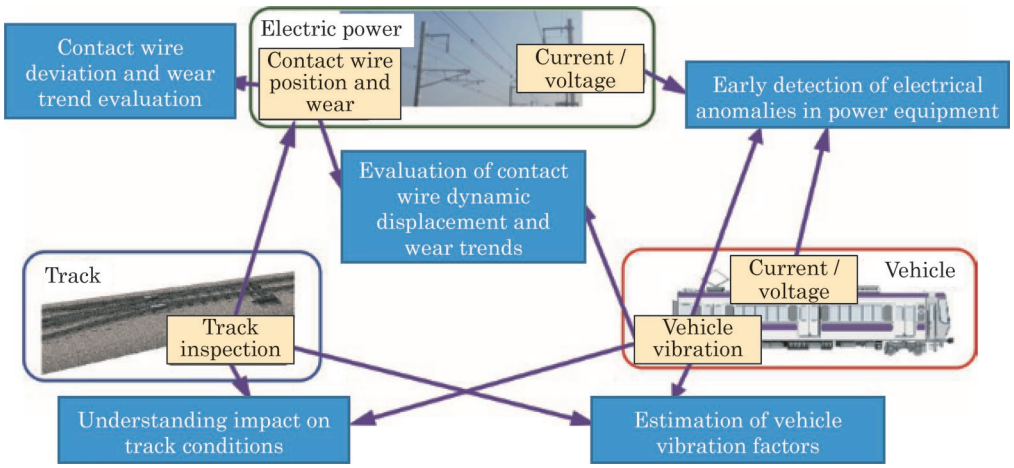

Fig. 1 Example of mutual relationships among multiple systems

rithm. Additionally, AI for object recognition is used in a system that recognizes sleepers and determines their deterioration state [10].

3.2 Conversion of bird's-eye view image

The size and shape of an object in an image change depending on the position and angle of the object and the camera. If the camera can face the object directly and shoot at a fixed distance, then the size and shape can be unified, and processing can be simplified. However, when using existing cameras or when prioritizing the ease of shooting, then this condition cannot always be met. An effective method in such a case is the method of obtaining a front-facing image (e.g., bird's-eye view image) by projective transformation [11].

Figure 3 shows an example of projective transformation. The image on the left side of Fig. 3 involves a set that simulated the tactile blocks on the platform, passengers, and the side of a vehicle, with an image taken from a camera installed on the side of the vehicle. The image on the right side of Fig. 3 is a bird's-eye view image that is converted by projective transformation. The size of the tactile block is known, so the distance between the person and the edge of the platform can be calculated by calculating the length per pixel [12]. As a result, the image from the camera installed on the side of the vehicle can be used to detect the approach of passengers, alert the driver, and count the number of people getting on and off the train.

The application in Fig. 2 also uses bird's-eye view images to calculate the amount of movement of the sleepers between frames, making it possible to calculate the traveled distance.

3.3 Frequency analysis

There are technologies that detect objects and events by detecting specific frequencies in images.

In an application that detects the blinking of an obstruction warning signal, a blinking pattern (bit string) is obtained by binarizing each frame of the moving image to 1 or 0 (lit or unlit) by threshold processing, and superimposing the continuous video frames. The blinking of the obstruction warning signal is detected by searching for the bit string that represents the frequency of the obstruction warning signal from the superimposed image [13].

Additionally, in an application that detects broken barriers at level crossings, the spatial frequencies in a single image are analyzed in order to determine whether or not level crossing rods are broken [14]. "black" and "yellow" are repeated at regular intervals on the rods, so this repeating state is discriminated using frequency analysis, and deviations from a predetermined range are judged to be a broken level crossing rod.

4. Information network

Railways have long focused on the research and development of wireless and wired communication technology, and there have been some cases where it led the way in domestic communication technology. Additionally, many of the communication systems used for railway operations have been installed as private lines. However, there has been remarkable evolution in information network technologies, including these communication technologies, and the use of general-purpose technologies and public communication lines has become beneficial in terms of both performance and cost. In response to such circumstances, there has been active research and development of general-purpose technologies and systems that use public communication lines.

4.1 Utilization of public communication lines

Currently, many of the communication systems used in railway operations are privately-operated networks that are designed, constructed, and maintained by railway operators themselves. Meanwhile, mobile communication technology has shown remarkable development in recent years. In particular, the 5th generation mobile communication system (5G) enables communication not only with the features of "ultra-high speed and large capacity," but also with the features of "high reliability and ultra-low latency" or "multiple simultaneous connections." The utilization of 5G services that allow the selection of these features is expected to result in the creation of new applications in addition to improving the functionality of conventional railway applications [15, 16]. However, as applications that individually apply 5G are implemented, the various specifications and unique handling that arise for each case need to be addressed, and many processes and costs are required for introduction studies and system design for both railway operators and telecommunications carriers. Therefore, guidelines are being created on how to define the requirements for achieving the functions of traffic control systems, basic system design at the time of introduction, and basic concepts for operation [17]. Plans for these guidelines are to

Fig. 2 Example of equipment recognition result

Fig. 3 Example of projective transformation

outline judgments of the necessity of applying 5G to operation control systems, basic policies for designing systems and equipment for introduction, and precautions regarding maintenance during operation, all from the perspective of railway operators that are considering the introduction of 5G. The customization of descriptions in the guidelines also allows railway operators to formulate the required specifications.

4.2 Utilization of public communication lines

As previously mentioned, the use of new technologies such as 5G and public networks can improve the functionality of railway applications and reduce the maintenance and management costs of communication equipment. Meanwhile, from the perspective of individual railway applications, these technologies are ultimately just means to an end, and they are sufficient so long as they can exchange information with a predetermined communication quality, regardless of the communication medium. Research and development are being conducted from this perspective on methods for trains to communicate while switching between various media [18]. Currently, an independent communication system is also being constructed for each railway application or each technical system, but if these communication systems can be integrated, then the reduced equipment necessary for communication as well as the sharing of information between technical systems will lead to the efficient maintenance described in Section 2.1. In order to achieve such a communication system, multiple communication media and multiple railway applications have been integrated. Furthermore, a railway information transfer protocol (RITP) has been proposed for switching communication media and routes according to requirements such as the degree of importance and priority of information, which differ for each railway application [19, 20].

5. Conclusions

In this paper, recent research and development was introduced from the perspectives of data analysis and decision making, sensing and recognition / judgment, and information networks. These technologies are ultimately shared technologies, and their effects can only be obtained when they are combined with the technologies of each operational system of the railway system. It is hoped that continued guidance and cooperation of railway operators and other associates will be provided to these endeavors.

References

[1] Hisada, T., "The current status of our efforts to realize smart maintenance," *JR EAST Technical Review*, No. 67, pp. 5-10, 2022 (in Japanese).

[2] Takatsuki, S., "Promoting IoT for condition monitoring of equipment along railway lines," *JR West Technical Journal*, No. 46, pp. 9-12, 2022 (in Japanese).

[3] Ryuo, S., "Development of an Integrated Analysis Platform for Cross-sectional Railway Maintenance Data," presented at the *IEEE 8th World Forum on Internet of Things (WF-IoT) 2022*, November 9, 2022.

[4] Kawamura, Y., Hada, A., Hosokawa, Y., Ryuo, S., "A Quantification Method of Trends for Maintenance Data in Railway," *Proceedings of 2022 IEE-Japan Industry Applications Society Conference*, 2022 (in Japanese).

[5] Suzuki, T., Watanabe, T., Okuda, D., Fukasawa, N., "Convenience Evaluation of Clock-face Local Railway Timetables," *RTRI Report*, Vol. 36, No. 12, pp. 35-40, 2022 (in Japanese).

[6] Okuda, D., Watanabe, T., Nakagawa, S., Suzuki, T., Fukasawa, N., "Evaluation Method for Implementation Effect of Disaster Countermeasures on a Freight Railway Network," *RTRI Report*, Vol. 36, No. 12, pp. 41-46, 2022 (in Japanese).

[7] Watanabe, T., Fukasawa, N., Okuda, D., Suzuki, T., "Quantification of Relationship between Image of Urban Railway Services and Residential Location Preference," *RTRI Report*, Vol. 36, No. 12, pp. 47-52, 2022 (in Japanese).

[8] Matsumoto, R., Nakagawa, S., Suzuki, T., Watanabe, T., Fukasawa, N., "A study on the effect of the opening of large shopping complex on rail transport revenues," Proceedings of the Jointed railway technology symposium (*J-RAIL2021*), 2021 (in Japanese).

[9] Mukojima, H., Nagamine, N., "Development of Signal Facilities Management Support System Using Camcorder Video on Train Cab," *RTRI Report*, Vol. 36, No. 8, pp. 45-50, 2022 (in Japanese).

[10] Miwa, M., "Track Technology for Reducing Maintenance Cost and Labor Work," *RTRI Report*, Vol. 36, No. 3, pp. 1-4, 2022 (in Japanese).

[11] Nagamine, N., Tsubokawa, Y., Goda, W., Maeda, R., Kato, S., Itoi, K., "Inspection Method of Track Facilities using Image Analysis of Images in Front of Trains," *RTRI Report*, Vol. 36, No. 12, pp. 7-12, 2022 (in Japanese).

[12] Goda, W., Nagamine, N., Mukojima, H., "Station Platform Safety Check Method for Driver Using Side Camera on Rolling Stock," *RTRI Report*, Vol. 35, No. 10, pp. 23-28, 2021 (in Japanese).

[13] Mukojima, H., Nagamine, N., Nomura, T., Ichikawa, T., "Blinking Detection for Obstruction Warning Signal using Front Camera," *Quarterly Report of RTRI*, Vol. 62, No. 2, pp. 118-123, 2021.

[14] Kageyama, R., Nagamine, N., Takasaki, T., Shindo, T., "Verification of dependence on time for the application of the crossing rod breakage detection using monitoring camera in real environment," *Proc. of the IEE-Japan TER / MSS Joint Technical Meeting,* TER-22-040, 2022 (in Japanese).

[15] Nakamura, K., Kitano, T., Kawasaki, K., Oomi, T., Fujishima, K., Ichikawa, S., "Verification of the Applicability of Fifth Generation Mobile Communication Systems to Railway Operations," *Quarterly Report of RTRI*, Vol. 64, No. 2, pp. 103-108, 2023.

[16] Nakamura, K., Kitano, T., Takeuchi, K., Ryuo, S., Kawasaki, K., "Study on the utilization of Public 5G for Railway Operations using Local 5G," *Proc. of the IEICE RCS Technical Meeting*, 2022 (in Japanese).

[17] Kitano, T., Iwasawa, N., Nakamura, K., Takeuchi, K., Kawasaki, K., "A Study for establishment of guideline for 5G Applying Guideline for Railway Operation Systems," *Proc. of the IEICE Society Conferencce,* 2022 (in Japanese).

[18] "Adaptable Communications System Field Test Strategy," http://projects.shift2rail.org/download.aspx?id=1f74972f-8a50-4564-bf18-af560414d90d (Reference on 21th September, 2022).

[19] Ryuo, S., Hada, A., Nakamura, K., Kawasaki, K., "Functional Verification Test of a Protocol to Integrate Information Network for Train Operation," *Proc. of the IEE-Japan CMN Technical Meeting,* 2022 (in Japanese).

[20] Ryuo, S., Hada, A., Yamaguchi, D., Nakamura, K., Kawasaki, K., "Proposal for Transmission Media Usage Functions in

Transmission Protocol for Railway System," *RTRI Report*, Vol. 36, No. 12, pp. 13-19, 2022 (in Japanese).

Author

Mitsuyoshi FUKUDA
Director, Head of Information and Communication Technology Division
Research Areas: Signalling System, Safety Engineering

Development of Longitudinal Excitation Suppression Devices for Reducing Car-body Elastic Vibrations in Bullet Trains

Ken-ichiro AIDA
Vehicle Noise and Vibration Laboratory, Vehicle Technology Division

Tadao TAKIGAMI
Vehicle Noise and Vibration Laboratory, Vehicle Technology Division (Former)

Yuki AKIYAMA **Yasunobu MAKITA**
Vehicle Noise and Vibration Laboratory, Vehicle Technology Division

This study proposes a method to reduce car body elastic vibrations in bullet trains caused by longitudinal excitation via traction devices and yaw dampers. We devised two vibration reduction devices—"displacement-dependent rubber bushes" and "mesh springs" to suppress the longitudinal excitation force. We conducted excitation tests using a Shinkansen (bullet train) type test vehicle in a rolling stock testing plant to examine the running stability and car body vibrations suppression performance when mounting the developed devices. Subsequently, we confirmed that these devices meet the required performance for running stability and reduce the elastic vibrations in the car body.

Key words**:** *bullet train, car body, elastic vibration, traction device, yaw damper, rubber bush*

1. Introduction

When a railway vehicle is running, it generates car body vibrations, which sometimes need to be reduced as they affect ride comfort. As far as the improvement of ride comfort is concerned, in addition to vibration suppression measures, such as active suspension and semi-active suspension [1], vibrations isolation measures in the vibration transfer paths have been implemented. Vibration isolation measures that have been investigated include vibration insulation using air springs [2] as well as measures focused on traction devices and yaw dampers, which connect members in the longitudinal direction of the vehicle. To date, measures to modify the spring characteristics of rubber bushes in a single-link type traction device [3, 4] and the damping characteristics of a yaw damper [5] have been proposed.

In this study, we propose two devices for suppressing the longitudinal excitation force transmitted from the bogie to the car body to reduce the elastic vibrations of car body and ensure improved ride comfort in bullet trains. Specifically, we propose a displacement-dependent rubber bush, which has been verified for its effectiveness in improving ride comfort by conducting running tests on multiple conventional railway vehicles, and investigate its novel application to bullet trains [6]. Moreover, we investigate the application of a mesh spring, made of fibrous stainless-steel wires, to the area where the single-link type traction device and yaw damper are mounted on the vehicle [7]. Here, we report the results obtained by our prototype displacement-dependent rubber bushes and mesh springs, which are applicable to single link-type traction devices and yaw dampers on bullet trains. We conducted excitation tests on the prototypes mounted on a test vehicle owned by RTRI. Finally, we report the results of an evaluation into the running stability and reduction of the car body elastic vibrations.

2. Excitation mechanism of car body elastic vibrations

Figure 1 illustrates a schematic representation of the vibration transmission paths for the elastic vibrations of the car body caused by the vertical track irregularity. For convenience, Fig. 1 expresses the state in which the car body vibrates in the modal shape of the primary bending deformation of the elastic beam. However, in practice, the car body also vibrates in various other modal shapes.

Figure 1(a) shows that the vertical vibrations of the wheelsets generated by the vertical track irregularity is transmitted to the bogie frames via the axle springs and then to the car body via the air springs, causing the car body to vibrate vertically. Here, the transfer path is only vertical. In contrast, Fig. 1(b) shows that the vertical vibrations of the wheelsets due to the vertical track irregularity causes the pitching vibrations of the bogie frames via the axle springs, which is transmitted to the car body as an excitation force in the longitudinal direction via the traction devices or yaw dampers. If the pitching motions of the front and rear bogies are anti-phase, a bending force is exerted on the car body, resulting in elastic vibrations of the car body in the vertical direction.

To reduce the car body vibrations by the mechanisms shown in Fig. 1(a), improvements to the vertical suspension system are being considered. Accordingly, developments of devices, such as variable primary and secondary hydraulic dampers for bullet trains, are currently underway [8]. In contrast, our research focuses on the mechanism shown in Fig. 1(b) and aims to suppress the transfer of the excitation force in the longitudinal system. Note that in the "vertical motion of bogies (in-phase)" shown in Fig. 1(a) and "pitching motion of bogies (anti-phase)" shown in Fig. 1(b), the frequency at which the maximum motion occurs is determined by the distance between two bogies and running speed. The two motion components are inversely related: when one is maximal, the other is minimal [9, 10]. As an example, Fig. 2 shows the results of calculating the frequency at which the bogie motion components are maximized with respect to running speed when the distance between two bogies is 17.5 m, typical for bullet trains. The blue line represents the frequency at which the in-phase bogie vertical motion component is maximized, while the red line represents the frequency at which the bogies' anti-phase pitching component is maximized. For example, at a speed of 240 km/h, the vertical motion component is maximized

at 11.4 Hz (blue circle), while the pitching component is maximized at 13.3 Hz (red circle).

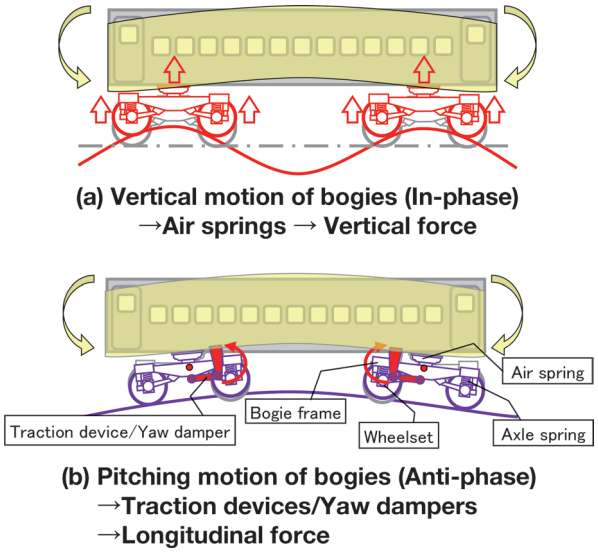

Fig. 1 Excitation transfer paths that induce elastic vibrations in the car body

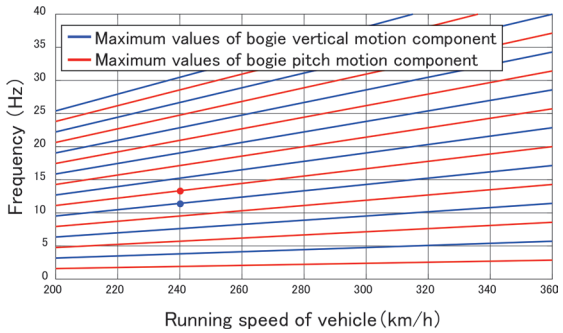

Fig. 2 Maximum values of bogie vibration derived from the distance between two bogies and running speed

The device proposed in this study is expected to reduce car body vibrations near the frequency band represented by red lines in Fig. 2. Especially, the application of the proposed device is expected to significantly affect the reduction of car body vibrations when these frequencies are closest to the natural frequency of the car body.

3. Fabrication of longitudinal excitation suppression devices

We proposed two devices for suppressing longitudinal excitation between bullet train bogies and car bodies: displacement-dependent rubber bushes and mesh springs. In this chapter, we present the results of investigating the prototype structure and characteristics.

3.1 Displacement-dependent rubber bush

So far, we have been developing a displacement-dependent rubber bush aiming to reduce the car body elastic vibrations caused by wheelset mass imbalance on conventional (non-bullet) train lines [3, 4]. It is a rubber bush for a single-link type traction device and yaw damper whose spring characteristics (stiffness) are different from devices designed for commercial vehicles (hereinafter referred to as "original devices"). The structure of the displacement-dependent rubber bush is shown in Fig. 3. In the original device, the inner fixture and rubber are bonded together. On the other hand, there is a small gap between the rubber and the inner fixture in our developed device. The small gap can be manufactured by skipping the bonding process between the rubber and the inner fixture. The transmission of excitation forces at high frequencies with small-amplitude relative displacement between the bogies and car body is isolated by the gap. In the case of large-amplitude relative displacement, the gap disappears, resulting in stiffness equivalent to that of the original device; accordingly, the single-link type traction device and yaw damper exhibit their original characteristics. Note that to prevent the separation of the rubber and the inner fixture when the lateral displacement and the rotation angle between the car body and the bogie occurs at a curve or similar situation, a through hole filled with rubber is provided in the center of the inner fixture.

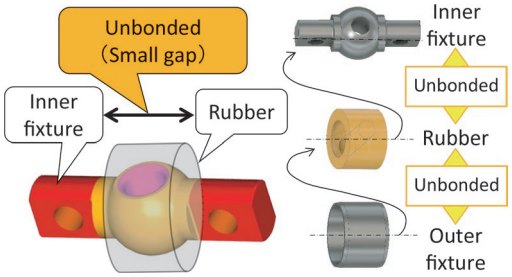

Fig. 3 Structure of the displacement-dependent rubber bush

We adopted the same structure as shown in Fig. 3 for the displacement-dependent rubber bush on the bullet train and built a prototype for a single-link type traction device. Figure 4 shows the prototype and its incorporation into a single-link type traction device. Generally, the stiffness of the rubber bush on the bullet train is set higher than that set on a conventional train line. To incorporate this requirement in the prototype, based on the designing processes of existing devices for conventional train lines, we changed the rubber composition and shape of the inner fixture to obtain a static stiffness equivalent to that of the original device. As the vehicle mounting dimensions of the prototype are the same as those of the original device, the installation does not require modifications on the vehicle.

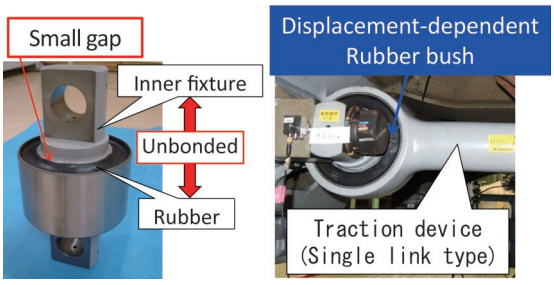

Fig. 4 Displacement-dependent rubber bush for bullet trains

We conducted an excitation test on the rubber bush alone to exam the stiffness of the prototype. Figure 5 shows the relationship

between the load and displacement in the direction perpendicular to the axis (the longitudinal direction when mounted on the vehicle) based on measured results. The slope of the plot presented in Fig. 5 corresponds to the stiffness. In the prototype, the slope is small near the neutral position (displacement is zero) but increases as the displacement increases. These results indicate that the stiffness of the prototype is a displacement-dependent property.

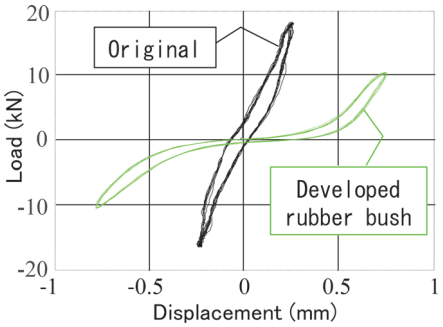

Fig. 5 Relationship between the load and displacement for rubber bush (bench test results)

In addition, when the prototype is mounted on a vehicle, it is necessary to confirm that the rubber and the inner fixture do not separate when relative displacement occurs between the car body and the bogie, such as in a curve. Therefore, we investigated the resilience under maximum lateral displacement between the bogie and the car body.

We incorporated the prototype into a single-link type traction device and used the damper test equipment at RTRI [11] to conduct a test in which displacement was applied in the axial direction of the rubber bush (the lateral direction when mounted on the vehicle). During the test, we observed the external appearance of the rubber bush and measured the amount of deformation in the rubber. The applied displacement was set to 51 mm, derived from the design value of the maximum relative lateral displacement and the rotation angle between the car body and the bogie. Figure 6 shows the situation when the displacement of 51 mm was applied. The test results showed that the rubber and inner fixture were not separated and no abnormal deformation of the rubber was observed. Therefore, we concluded that resilience was not affected during lateral displacement and the rotation angle between car body and the bogie in a curve or similar situation.

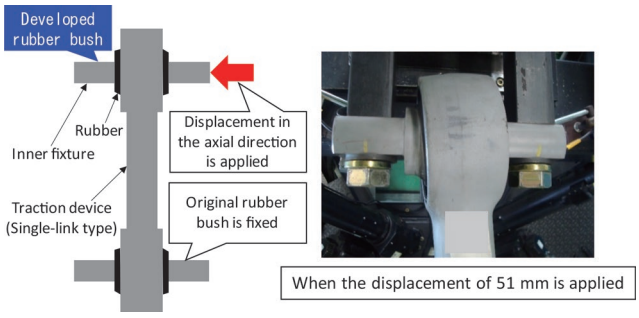

Fig. 6 Appearance of the rubber bush in the resilience test

3.2 Mesh spring

We investigated the application of the mesh springs shown in Fig. 7 to the area where the single-link type traction device and the yaw damper were mounted on the vehicle as a device for suppressing the excitation that does not require changes in the characteristics of the rubber bush. Subsequently, we manufactured a circular ring-shaped prototype device that is applied to the bolts. Figure 7 shows the application of this device to a yaw damper. For the prototype, we considered a thickness (natural length) of 10 mm. For the single-link type traction device, the outer diameter was 49 mm and inner diameter was 35 mm. For the yaw damper, the outer diameter was 45 mm and inner diameter was 34 mm. Mesh springs are made of fibrous stainless-steel wires that are braided and compression-molded. They do not exhibit the hardening and deterioration seen in anti-vibration rubber. In addition to being rust-resistant, they exhibit certain damping characteristics not found in ordinary sheet metals, such as a certain amount of damping due to the friction between fibers. When the mesh springs are compressed perpendicular to the mounting surface, in regions where the displacement is small, the stiffness is low owing to the gaps between the fibers. As the displacement increases, the gap decreases and stiffness gradually increases. Therefore, we expect the mesh springs to exhibit characteristics similar to those of the displacement-dependent rubber bush shown in Fig. 5.

When applied to an actual vehicle, mesh springs are used in a pre-compressed state. Accordingly, their stiffness varies with the amount of compression. Therefore, we conducted the same excitation test as that reported in Fig. 5 using the mesh springs applied to a single-link type traction device to obtain the relationship between the load and displacement in the direction perpendicular to the axis of the rubber bush. The measurement results are shown in Fig. 8. In the excitation test, we started with an initial length of 82.8 mm, as shown in Fig. 8, and then took measurements in 0.5 mm increments. Notably, the test results indicated that if the initial length is large (precompression is low), the slope is small; however, the

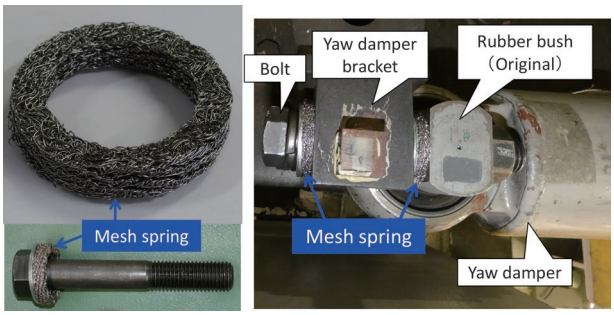

Fig. 7 Mesh spring for bullet trains

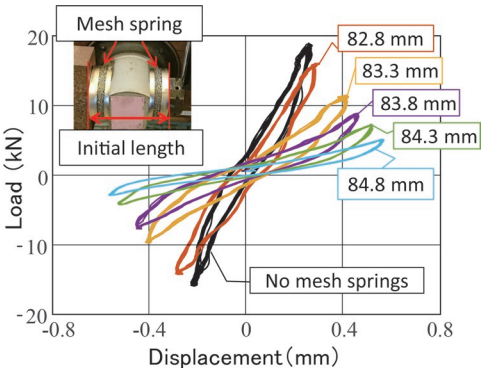

Fig. 8 Relationship between the load and displacement for a rubber bush fixed with mesh springs (bench test results)

slope gradually increases as the initial displacement decreases. When the initial length is 83.3 mm or 83.8 mm, the slope near the zero displacement is small, but the displacement dependence of the slope increases as the displacement increases. Based on this result, we used mesh springs with an initial length of 84.0 mm, close to the purple line in Fig. 8, during the test on an actual vehicle described below.

4. Verification of running stability and vibration reduction effect of a half car body equipped with the prototype rubber bushes

We verified the running stability of a half car body installed with the prototype displacement-dependent rubber bushes before conducting a verification test on an actual vehicle. We conducted a hunting stability test at the rolling stock testing plant at RTRI with the prototype mounted on a single-link type traction device on a bullet train bogie. Figure 9 outlines the test setup. We loaded the bogie with a load frame equivalent to a half car body and added deadweight to the load frame until the weight, including the bogie, reached 22.9 tons. In addition to the hunting stability test, we conducted excitation tests to investigate the possibility of reducing car body vibration. We installed a 3-axis accelerometer on the load frame corresponding to the car body to measure the vibration accelerations.

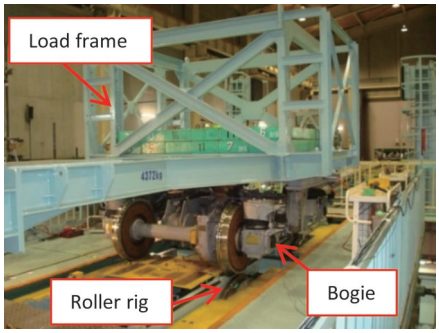

Fig. 9 Testing using a half car body in the rolling stock testing plant at RTRI

4.1 Running stability

Applying the prototype of rubber bushes, we conducted the hunting stability test to assess whether the hunting motion can be prevented at speeds up to 400 km/h. During the hunting stability test, we gradually increased the rotational speed of the roller rigs at the rolling stock testing plant. At intervals of 5 km/h or 10 km/h, we displaced the roller rigs in the lateral direction with three continuous sinusoidal waves with an amplitude of ±3 mm and a frequency of 1 Hz. Subsequently, we determined the critical hunting speed based on the lateral displacement of axle box of the bogie.

The test results demonstrated that when two yaw dampers (one on each side of the bogie) were mounted, no hunting motion due to divergence of lateral displacement was observed at speeds up to 400 km/h, the maximum speed tested.

4.2 Vibration reduction effect

We conducted an excitation test on the rubber bushes—covering both the prototype and the original device—mounted on a single-link type traction device on the test bogie using an excitation signal that reproduces the acceleration measured on both sides of the axle boxes of a wheelset while running on a commercial line (hereinafter referred to as "simulated running excitation"). Then, we compared the longitudinal, lateral, and vertical accelerations in the load frame. Note that the excitation was provided to displace the roller rigs simultaneously in the vertical and lateral directions in the rolling stock testing plant.

Figure 10 shows the acceleration power spectral densities (PSDs) on the load frame in the longitudinal, lateral, and vertical directions. Compared to the original device, the prototype exhibits lower acceleration PSD in the frequency range above 5 Hz in both longitudinal and vertical directions. On the other hand, in the lateral direction, corresponding to the axial direction of the rubber bush, there was no difference compared to the original device.

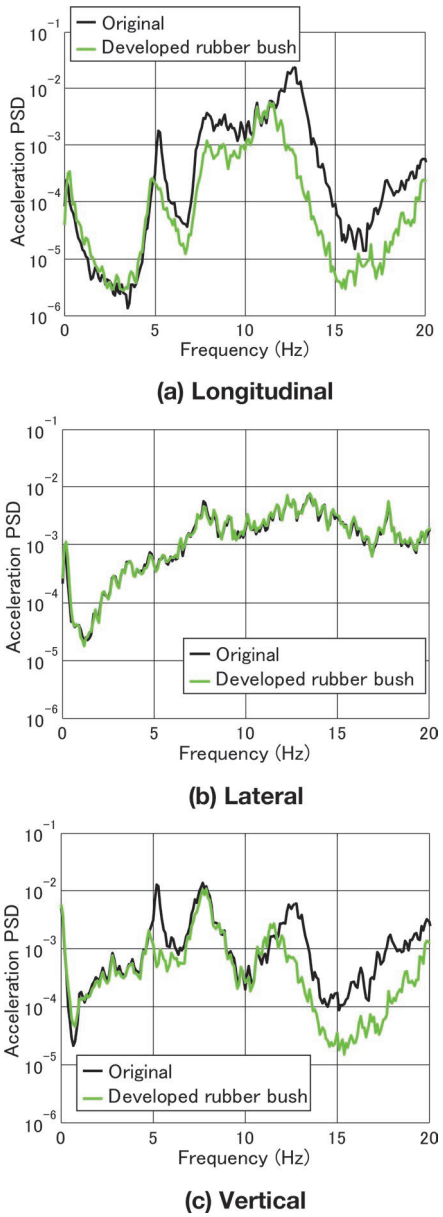

Fig. 10 Acceleration PSDs on the load frame (simulated excitation with the developed rubber bushes)

5. Verification of running stability of the test vehicle equipped with the prototype

The test results presented in chapter 4 demonstrated the possibility of ensuring running stability and reducing car body elastic vibrations. Subsequently, we conducted a test with the prototype installed on a Shinkansen-type test vehicle in the rolling stock testing plant at RTRI, shown in Fig. 11.

In this chapter, we conducted the hunting stability test using the same test method as that described in section 4.1 to verify running stability of the test vehicle equipped with the prototype. We set the two conditions for the single-link type traction device of the rear bogie: the displacement-dependent rubber bushes, and the mesh springs (on the car body side only). During the testing process, one yaw damper was operated near its failure condition, with the maximum test speed set to 360 km/h. To place the yaw damper in a failure condition, we intentionally mixed air into the damper to ensure that the damping force was approximately 1/20 of the specified value before it was used for the hunting stability test.

The test results indicated no lateral displacement divergence in the bogie axle box at speeds up to 360 km/h, which was the maximum test speed, under both the condition with the displacement-dependent rubber bushes and with the mesh springs applied. Based on these results, we concluded that no practical problems would arise regarding the running stability when the prototype displacement-dependent rubber bushes and mesh springs were applied.

Fig. 11 Testing with a Shinkansen-type test vehicle in the rolling stock testing plant at RTRI

6. Verification of vibration reduction effect of the test vehicle equipped with the prototype

We conducted excitation tests in the rolling stock testing plant under conditions in which displacement-dependent rubber bushes or mesh springs were applied to the test vehicle. We measured the vertical vibration accelerations of the car body floor to verify the reduction of elastic vibrations of the car body. With the condition where the displacement-dependent rubber bushes were applied, prototypes were used for the front bogie and the rear bogie. When testing the mesh springs, we targeted two conditions: one where we applied our prototype to the single-link type traction devices and another where we applied the prototype to the yaw dampers (on the car body side only).

Among the tests carried out under multiple excitation conditions, here we report the results of the anti-phase pitching excitation in the bogies and simulated running excitation corresponding to 240 km/h. In the case of the anti-phase pitching excitation in the bogies, the effect of the longitudinal excitation force is large; accordingly, it is assumed that the prototype has a significant effect on reducing the car body vibration.

6.1 Displacement-dependent rubber bushes application condition

In this section, we compare the case where the original device is used as the rubber bushes on a single-link type traction device with the case where the displacement-dependent rubber bushes are applied.

6.1.1 Anti-phase pitching excitation in the bogies

Figure 12 shows the longitudinal acceleration PSDs of the center pin (the car body side of the traction device) and the vertical acceleration PSD on the car body floor above the front bogie due to the anti-phase pitching excitation in the bogies. In the legend of Fig. 12(b), the number expressed in dB represents the difference (ΔL_T) in the ride quality level (L_T) [12] achieved with the original device and the prototype. A negative value means that the ride comfort was improved by the prototype.

Looking at the PSDs shown in Fig.12, we can see that the prototype exhibits lower acceleration PSD over a wide range of frequencies in the longitudinal direction of the center pin compared to the original device. Similarly, for the vertical vibrations of the car body floor, a reduction in acceleration PSD is seen at frequencies above approximately 7 Hz: an improvement of more than 3 dB in ride quality level was observed. Therefore, we confirmed in an actual vehicle that the longitudinal excitation force transmitted from the bogie to the car body was suppressed by displacement-dependent rubber bushes, thereby reducing the elastic vibrations of the car body.

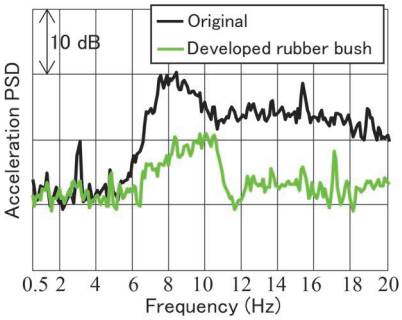

(a) Longitudinal acceleration of the center pin (car body side of traction device)

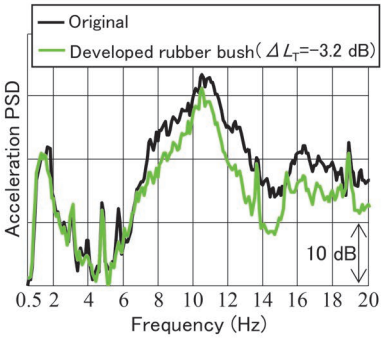

(b) Vertical acceleration of the car body floor above the front bogie

Fig. 12 Acceleration PSDs (anti-phase pitching excitation in the bogies with the developed rubber bushes)

6.1.2 Simulated running excitation

Figure 13 shows the vertical acceleration PSDs of the car body floor above the front bogie (the same as Fig. 12(b)) as a result of simulated running excitation. The legend in Fig. 13 denotes the difference in ride quality levels achieved with the original device and the prototype.

Looking at the PSDs shown in Fig.13, we can see that the peak value occurring near 13.3 Hz is reduced with the prototype. This frequency corresponds to the frequency at which the anti-phase pitching component, indicated by the red circle in Fig. 2, reaches its maximum. Therefore, we conclude that the prototype can effectively suppress the excitation transmission caused by this component. However, in terms of the evaluation of ride quality level, the improvement was small because of the slight increase in the peak value observed around 10.7 Hz when using the prototype. We speculate that the result is related to the dynamic vibration absorber effect of the bogie frame mass [13], which occurs when the resonance points of the car-body vertical vibration and bogie longitudinal vibration are close to each other. In the original device, the two resonance points are close to each other, which is assumed to reduce the vertical vibration of the car body. On the other hand, in the prototype, there was a greater difference between the two resonance points, which likely reduced the dynamic vibration absorber effect in the original device, resulting in larger vertical vibrations of the car body than that observed with the original device.

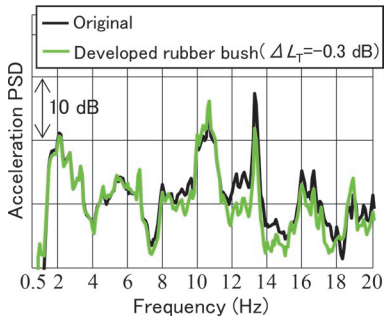

Fig. 13 Acceleration PSDs of the car body floor above the front bogie (simulated running excitation with the developed rubber bushes)

6.2 Mesh springs application condition

This section compares the condition in which mesh springs are applied to single-link type traction devices or yaw dampers with the original condition (no mesh springs).

6.2.1 Anti-phase pitching excitation in the bogies

Figure 14 shows the vertical acceleration PSDs of the car body floor above the front bogie as a result of the anti-phase pitching excitation in the bogies. The legend in Fig. 14 shows the difference in ride quality levels achieved under the original conditions and after applying the prototype.

Compared to the original conditions, when the prototype was applied to the yaw damper, a reduction in acceleration PSD was observed around 7 to 15 Hz. Moreover, an improvement of more than 2 dB in ride quality level was observed. When the prototype was applied to the single-link type traction device, the improvement in ride quality level was only 0.5 dB, which was small compared to when the prototype was applied to the yaw damper.

Since the relationship between the vibration reduction effect of the prototype when applied to a single-link type traction device or yaw damper also depends on the vehicle and the excitation conditions, we intend to continue with our investigation on this point in the future to clarify the underlying mechanism.

6.2.2 Simulated running excitation

Figure 15 shows the vertical acceleration PSDs of the car body floor above the front bogie as a result of simulated running excitation. The legend in Fig. 15 shows the difference in ride quality levels achieved under the original condition and when the prototype application.

As with the application of the displacement-dependent rubber bushes shown in Fig. 13, no significant vibration reduction effect over a wide frequency range was obtained with the prototype. However, focusing on the peak around 13.3 Hz, where the anti-phase pitching component is at its maximum, it is observed that the peak height is smaller in the condition where the prototype is applied to the yaw damper than that in the original condition. This confirms that the mesh springs has the same effect of suppressing the transfer of the longitudinal excitation force as the displacement-dependent rubber bushes. The reason why the vibration reduction effect was not obtained over a wide frequency range is that, as explained in chapter 2, there are vibration transfer paths other than the single-link type traction devices and yaw dampers. Accordingly, we consider that the prototype cannot be expected to reduce the vibration caused by the mechanism shown in Fig. 1 (a).

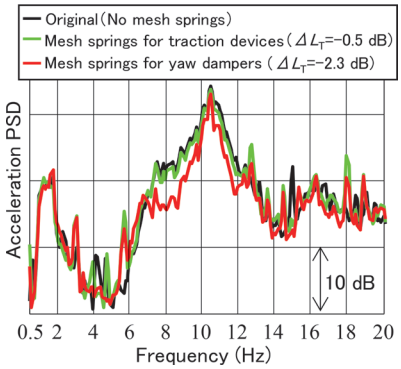

Fig. 14 Acceleration PSDs of the car body floor above the front bogie (anti-phase pitching excitation in the bogies with mesh springs)

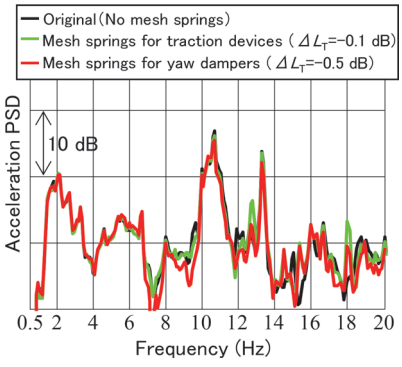

Fig. 15 Acceleration PSDs of the car body floor above the front bogie (simulated running excitation with mesh springs)

7. Conclusion

We proposed to apply a displacement-dependent rubber bush to bullet trains as a device to suppress the transfer of the longitudinal excitation force between the bogie and the car body to reduce the car body elastic vibrations. Subsequently, we fabricated a prototype for a single-link type traction device. In addition, we proposed mesh springs, which are made of fibrous stainless-steel wires, as a method that does not require changes in the characteristics of the rubber bush and produced a prototype that can be applied to the single-link type traction device and yaw damper of bullet trains. To verify running stability, we applied the prototype on a Shinkansen-type test vehicle owned by RTRI. The results of the hunting stability test, which simulated the failure of the yaw damper, demonstrated that there was no problem with running stability at speeds up to 360 km/h which was the maximum speed tested. Furthermore, as a result of verifying the reductions in car body vibrations, we confirmed that the elastic vibrations of the car body were reduced under the excitation condition where the longitudinal excitation force from the bogie was large.

From the obtained results, we were able to demonstrate the effectiveness of the proposed longitudinal excitation suppression devices. However, in terms of evaluating the ride quality level under excitation conditions simulating actual driving, the improvement was small. Therefore, we plan to continue our investigations regarding the optimal values of the device stiffness and other factors.

References

[1] Fu, B., Giossi, R. L., Persson, R., Stichel, S., Bruni, S. and Goodall, R., "Active suspension in railway vehicles: a literature survey," *Railway Engineering Science*, 28(1), pp. 3-35, 2020.

[2] Koyanagi, S., "A Design Method for the Vibration Isolation System of an Air Spring Suspended Vehicle," *Quarterly Report of RTRI*, Vol. 32, No. 1, pp. 2-7, 1991.

[3] Tomioka, T. and Takigami, T., "Development of Displacement-Dependent Rubber Bush to Reduce Carbody Vibration Induced by Mass-Imbalanced Wheelsets through Traction Links," *Quarterly Report of RTRI*, Vol. 52, No. 3, pp. 141-148, 2011.

[4] Aida, K., Tomioka, T., Akiyama, Y. and Takigami, T., "Development of Displacement-dependent Rubber Bush for Yaw Damper to Prevent Carbody Vertical Vibration," *Quarterly Report of RTRI*, Vol. 58, No. 3, pp. 182-188, 2017.

[5] Suciu, B. and Tomioka, T., "Experimental investigation on the dissipative and elastic characteristics of a yaw colloidal damper destined to carbody suspension of a bullet train," *Journal of Physics: Conference Series*, Vol. 744, No. 1, 012142, 2016.

[6] Aida, K., Takigami, T., Akiyama, Y. and Makita, Y., "Displacement-dependent rubber bush for Shinkansen to improve ride comfort," *Proceedings of 28th Jointed railway technology symposium (J-RAIL2021)*, 2021, No. SS4-1-3 (in Japanese).

[7] Takigami, T., Akiyama, Y., Makita, Y. and Sato, Y., "Reducing Bending Vibration of Railway Vehicle Carbodies by longitudinal Isolation Effect of "Mesh Springs"," *Proceedings of 26th Jointed railway technology symposium (J-RAIL2019)*, 2019, No. S4-1-4 (in Japanese).

[8] Sugahara, Y., Sannomiya, D., Miyahara, K. and Amano, A., "Suppression of Vertical Vibrations in Railway Vehicles Using Variable Primary and Secondary Hydraulic Dampers," *Proceedings of 28th Jointed railway technology symposium (J-RAIL 2021)*, 2021, No. SS1-3-3 (in Japanese).

[9] The Japan Society of Mechanical Engineers (Ed.), *Railway Vehicle Dynamics and Modeling*, Maruzen Publishing Co. Ltd., pp. 122-126, 2017 (in Japanese).

[10] Dumitriu, M., "Considerations on the geometric filtering effect of the bounce and pitch movements in railway vehicles," *Annals of the Faculty of Engineering Hunedoara-International Journal of Engineering*, Vol. 12, No. 3, pp. 155-164, 2014.

[11] Watanabe, N., Iida, T., Umehara, Y., Asahina, M., Koganei, R. and Yamanaga, Y., "Development of Oil Damper Test Equipment Capable of Simulating the Actual Conditions of Railway Vehicles," *Quarterly Report of RTRI*, Vol. 49, No. 1, pp. 1-6, 2008.

[12] Suzuki, H., "Research trends on riding comfort evaluation in Japan," *Proceedings of the Institution of Mechanical Engineers, Part F: Journal of Rail and Rapid Transit*, Vol. 212, Issue 1, pp. 61-72, 1998.

[13] Tomioka, T. and Takigami, T., "Reduction of bending vibration in railway vehicle carbodies using carbody-bogie dynamic interaction," *Vehicle System Dynamics*, 48, pp. 467-486, 2010.

Authors

Ken-ichiro AIDA
Senior Researcher, Vehicle Noise and Vibration Laboratory, Vehicle Technology Division
Research Areas: Carbody Structure, Ride Comfort Evaluation

Tadao TAKIGAMI, Ph.D.
Senior Chief Researcher, Head of Vehicle Noise and Vibration Laboratory, Vehicle Technology Division (Former)
Research Areas: Flexural Vibration of Carbody, Vibration Analysis, Ride Comfort Evaluation

Yuki AKIYAMA, Ph.D.
Senior Researcher, Vehicle Noise and Vibration Laboratory, Vehicle Technology Division
Research Areas: Carbody Vibration of Control, Vibration Analysis, Ride Comfort Evaluation

Yasunobu MAKITA
Researcher, Vehicle Noise and Vibration Laboratory, Vehicle Technology Division
Research Areas: Vibration Analysis, Ride Comfort Evaluation, Interior Noise Evaluation

Proposal for Energy-saving Driving Method for Freight Trains Combining Constant-speed Operation and Coasting Operation

Tomoyuki OGAWA
Hydrogen and Sustainable Energy Laboratory, Vehicle Technology Division

This paper presents energy-saving driving methods for freight trains. First, we discuss a driving strategy that conserves energy considering running resistance and motor efficiency. Secondary, we confirm energy consumption and maneuverability, conducting running tests on several energy-saving driving methods. We also establish an energy simulation method by reproducing running tests. Finally, we verify the proposed driving method for energy-saving conducting energy simulation. This paper proposes a driving method combining constant-speed operation and coasting, which is expected to reduce energy consumption in terms of running resistance and motor efficiency.

***Key words*:** *energy consumption, constant-speed operation, saw-toothed operation*

1. Introduction

Various research and developments have been conducted in order to reduce energy consumption associated with railway operation [1]. This research and development is broadly divided into methods for introducing energy-saving technologies into power supply equipment and rolling stock equipment, and energy-saving methods for devising train driving methods. Of these, the latter method, energy-saving driving, has the difficulty that needs to be considered for maneuverability, which is a human factor. Therefore, although many theoretical studies have been conducted, there are a limited number of practical examples, and they may be expected to have a large energy-saving effect if properly achieved in the future.

It has long been known that the lowest energy consumption is theoretically achieved by the driving of maximum powering, constant-speed running, coasting, and maximum braking (Fig. 1) [1, 2]. However, even when applying this theory, energy-saving driving cannot be realized unless applied to the actual driving maneuverability of drivers. As an example of this, even though maximum braking saves energy, this cannot be applied to actual driving unless the brake can adjust the stopping position, so the maximum braking needs to be considered in terms of actual maneuverability rather than in terms of rolling stock performance. Additionally, it is well known that gradually changing the traction or braking force rather than switching the notches instantaneously is desirable to prevent impulsive shock. As these examples illustrate, there are various issues in applying energy-saving driving to actual driving, and proper combinations of theory and experimentation are necessary. Therefore, in this report, we first theoretically study energy-saving driving methods, after which we study the possibility of applying these methods to actual maneuverability, and we propose an energy-saving driving method for freight trains that combines constant-speed operation and coasting operation.

2. Background

2.1 Characteristics of freight train driving

Freight trains have very different characteristics from passenger trains. Freight trains have few stops at stations, no clock-face scheduling, the train mass varies from day to day, and have a very limited number of locomotives that regenerate electric power. Freight trains have powering notches divided into multiple stages because they use a concentrated traction system from the locomotive; they commonly operate by incrementing powering notches stepwise for impulsive shock and slipping prevention. The deceleration of freight vehicles varies significantly day to day due to the difference in the number and mass of freight wagons. Since freight trains have significantly different driving characteristics to passenger trains, the application and evaluation of energy-saving driving used for passenger trains is difficult to apply to freight trains. Additionally, timetables have for freight trains train large time margins because they share the line and time slots with other trains. Furthermore, compared to cases where the trains are running at close-to-maximum speeds or at the speed limit, there is often a greater degree of freedom in driving. As such, there are many options available when considering energy-saving driving methods for freight trains, increasing the degree of difficulty in theoretical studies. While various energy-saving driving methods can be considered for freight trains, in majority of cases, most of the driving time is in cruising mode. In cruising mode freight trains require less use of brakes, except for when they are subject to signal aspects and station-passing time restrictions, and traditionally, freight train operation is energy efficient in terms of travel distance and mass of freight. This would suggest that current driving is already low energy consuming when cruising; and to achieve energy-saving driving that consumes even less energy than now means that other actual freight train parameters need to be considered. Therefore, we fo-

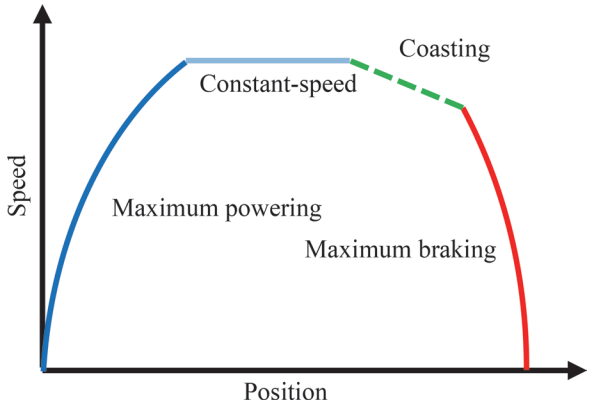

Fig. 1 Basic theory of energy-saving operation [3]

cused on the cruising operation of freight trains, and we studied energy-saving operation methods through running tests and energy simulations based on the running resistance characteristics and motor efficiency characteristics that have been measured for freight trains and locomotives in recent years. Based on these results, we propose a combination of constant-speed operation and coasting as an energy-saving driving method for freight trains.

2.2 Basic theory of energy-saving driving

We theoretically studied energy-saving driving methods for freight trains. For freight trains that do not use regenerated electric power, energy consumption is the integrated value of power consumption during powering (including constant-speed operation), and the energy consumption needs to be reduced. Theoretical calculations confirm the idea that energy saving driving consists of maximum powering, constant-speed running, coasting, and maximum braking minimize energy consumption [2], as shown in Fig. 1. In this report, this is referred to as the basic theory of energy-saving driving. The basic theory of energy-saving driving assumes that the running resistance is expressed by a quadratic formula with respect to speed, and that vehicle equipment efficiency is constant. Therefore, when considering vehicle equipment efficiency according to speed and power, there is a possibility that energy consumption could be reduced by driving methods that differ from the basic theory of energy-saving driving.

2.3 Cruising operation method

In freight trains, specific passing times are designated at most of non-stop stations. And most freight trains run between designated non-stop stations within a specified time. There is a certain amount of margin given to the specified time, and there are many cases of cruising at a speed lower than the maximum speed limit of the line. In this report, we focus on the driving methods for this type of case.

Cruising can be broadly divided into saw-toothed operation and constant-speed operation. Figure 2 and Fig. 3 show the respective conceptual speed curves of saw-toothed operation and constant-speed operation. The saw-toothed operation repeats powering and coasting, and driving has a certain speed range. During powering, electric locomotives with traction converter have 10 or more notches to choose from, but in such cases, large notches that exceed the train resistance (sum of running resistance, gradient resistance, curve resistance, etc.) are used. Meanwhile, in constant-speed operation, trains run at an average speed that is calculated from the specified time and distance between the designated stations, and this can be achieved by using a powering notch that balances the train resistance or by using the constant-speed function of the traction converter. In recent years, electric locomotives with traction converter have a constant-speed operation function, so they are becoming easier to apply.

3. Evaluated train

3.1 Overview of evaluated train driving

The target train was a freight train in which an inverted-controlled DC electric locomotive towed tank wagons and container wagons loaded with tank containers (henceforth, referred to as the "evaluated train"). The evaluated train set has a mass that can be obtained with relatively high accuracy, so high reliability can be expected not only for comparisons of measurement results but also for the determination of running resistance and setting of simulation conditions.

The evaluated train ran non-stop for a section of about 70 [km]. In the section, about 20 stations have designated passage times and the train is required to drive in compliance with the passage time and speed limit. The target line partly includes gradients with a maximum gradient of 12 [‰], but the average gradient of the entire line was 1.0 [‰]; and the target line generally has many gradual uphill gradients (Fig. 4).

3.2 Estimation of running resistance characteristics

There are various types of train set for freight trains, and there are limits to the running resistance equations that can be determined by running tests. For this reason, it is desirable to estimate the running resistance according to the composition of the train set. Therefore, we collected train monitoring data of the evaluated train. Figure 5 shows the running resistance characteristics of the evaluated train.

3.3 Estimation of motor efficiency characteristics

Type test results of the relevant traction motor were used to estimate motor efficiency. We calculated the motor efficiency for each powering notch of the locomotive of the evaluated train, and we used it as a motor efficiency model for simulation. Figure 6

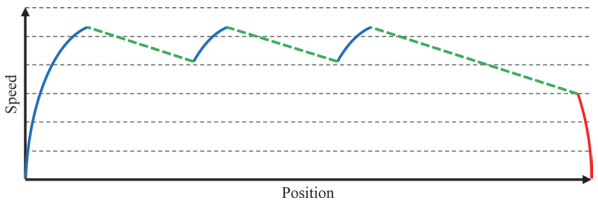

Fig. 2 Conceptual speed curve of saw-toothed operation [3]

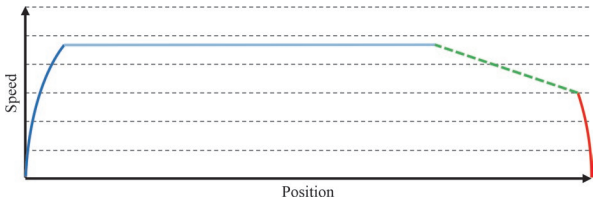

Fig. 3 Conceptual speed curve of constant-speed operation [3]

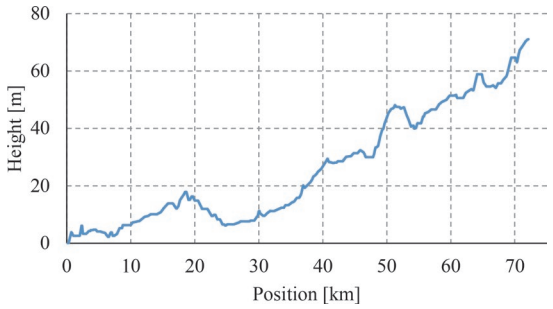

Fig. 4 Overview of running track

shows the results of calculating the motor efficiency for each powering notch of the locomotive. The motor efficiency was particularly high when the powering notch was between 8–9 N, with the motor efficiency dropping greatly when the powering notch was less than 6 N.

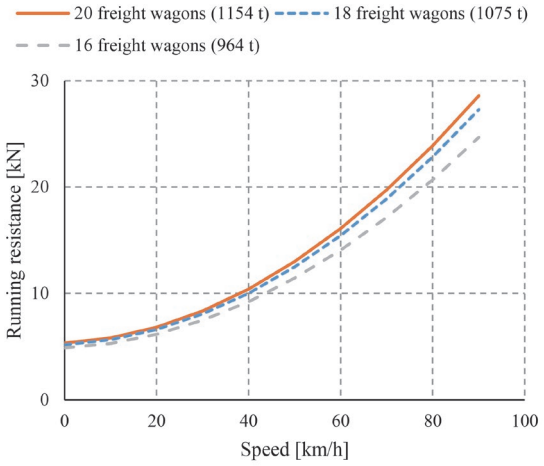

Fig. 5 Estimated running resistance characteristics [3]

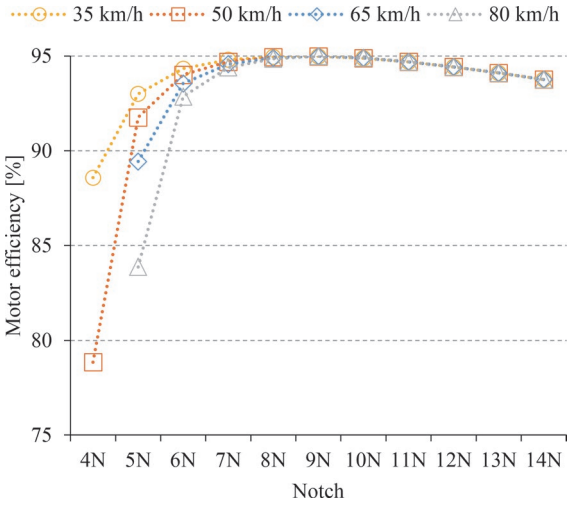

Fig. 6 Motor efficiency characteristics for power running notch [3]

4. Theoretical study of energy-saving driving

4.1 Overview of study

We conducted an energy-saving operation test in order to study energy-saving driving methods for freight trains. The energy-saving operation test adopted the driving method shown in Fig. 7. The theoretical basis for these is presented in this section. For cruising operation, which is the subject of this report, small-step saw-toothed operation and constant-speed operation were adopted, which almost certainly reduce energy consumption in terms of running resistance and motor efficiency. Specifically, we presented a theoretical study for adopting three types of driving methods: small-step saw-toothed operation, mainly constant-speed operation, and combined constant-speed operation. Additionally, in the energy-saving operation test, there are sections in which driving other than cruising is conducted, so prompt acceleration operation, constant-speed operation under the speed limit, and coasting toward the speed limit are implemented. Theoretical studies for implementing these are also presented.

4.2 Theoretical study of cruising operation

We studied the running resistance and motor efficiency during cruising operation.

4.2.1 Running resistance

In terms of running resistance, lowering running resistance when at high speeds contributes to energy-saving driving. This is because the running resistance increases in proportion to the square of the speed, so when running a certain section at the same running time, The smaller the change in speed, the smaller the losses due to running resistance, hence the loss due to running resistance is minimized when running at a constant speed. Therefore, in terms of running resistance, constant-speed operation is advantageous for energy-saving driving.

4.2.2 Motor efficiency

In terms of motor efficiency, operating with high-efficiency and large motor output contributes to energy-saving operation. Constant-speed operation, where a speed is held constant, is achieved by outputting a tractive force equal to the train resistance. Figure 8

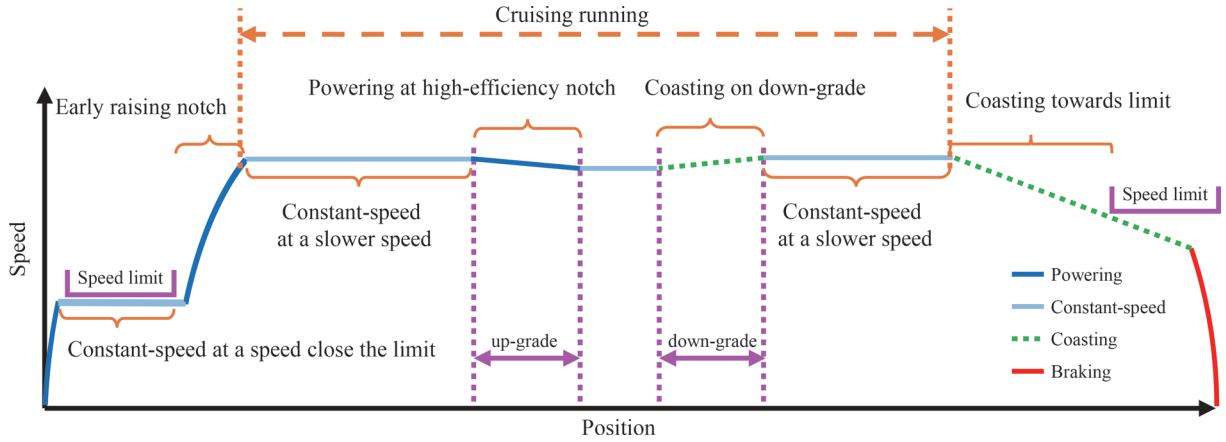

Fig. 7 Conceptual speed curve of energy-saving operation of freight train [3]

shows the motor efficiency characteristics during constant-speed operation. The motor efficiency varies depending on the speed during constant-speed operation, and the motor efficiency decreases as the gradient decreases in constant-speed operation. Meanwhile, in saw-toothed operation, the motor output is large, so the motor efficiency increases. Therefore, in terms of motor efficiency, saw-toothed operation is advantageous for energy-saving driving.

4.3 Study of small-step saw-toothed operation

When considering the running resistance characteristics and motor efficiency characteristics, it can be seen that both saw-toothed operation and constant-speed operation have advantages and disadvantages in terms of energy saving. Therefore, a small-step saw-toothed operation that repeats powering and coasting while approaching a constant speed is a candidate for energy-saving operation. Figure 9 shows a conceptual speed curve of small-step saw-toothed operation. In other words, small-step saw-toothed operation is saw-toothed operation with a small speed range.

4.4 Study of combined use of constant speed and coasting

Small-step saw-toothed operation involves frequent switching between powering and coasting, which causes difficulty in maneuverability. Therefore, we studied a driving method that did not use small-step saw-toothed operation. When we compared the respective influences of running resistance characteristics and motor efficiency characteristics on energy consumption in constant-speed operation and saw-toothed operation using an energy simulation, which will be described later, results showed that the running resistance characteristics had a larger influence. In other words, constant-speed operation seems to be the second-most energy-saving method for maintaining a constant speed, next to small-step saw-toothed operation. Therefore, when considering the change in gradient of actual routes, actively switching to coasting seems to be desirable in downhill gradients or near-flat sections, where the motor output during constant-speed operation decreases according to the running speed and the mass to be towed. In this report, the method of using constant-speed operation regardless of the gradient is called "mainly constant-speed operation," and the method of actively switching to coasting according to the gradient is called "combined constant-speed operation." Table 1 shows the energy-saving driving method during cruising.

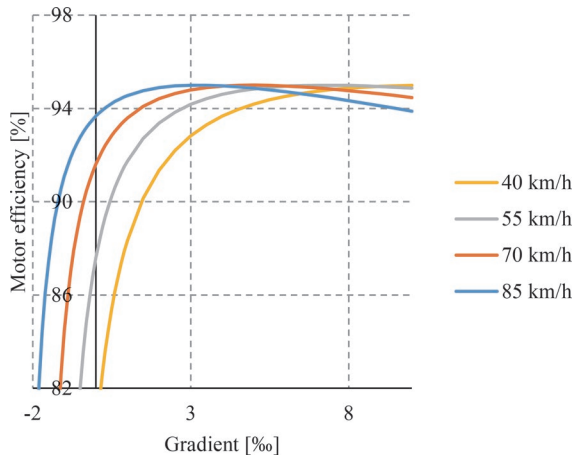

Fig. 8 Motor efficiency during constant-speed operation (at 20 freight wagons, 1154 [t])

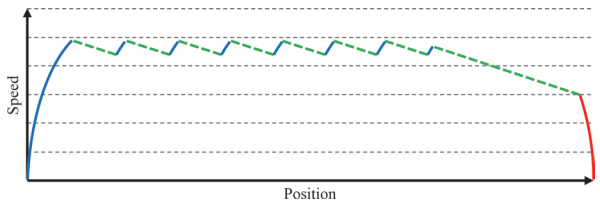

Fig. 9 Conceptual speed curve of small-step saw-toothed operation [3]

4.5 Energy-saving driving other than cruising

A qualitative argument is presented for sections where the driving is other than cruising.

4.5.1 Rapid acceleration operation

As stated in the basic theory of energy-saving driving, maximum powering during acceleration reduces energy consumption. This is because driving at low acceleration requires more time while the train is at low speed, and if it is necessary to travel the same distance in the same time, then more acceleration is required at higher speeds to compensate for time. Therefore, it is desirable that the powering notch is raised quickly within a range that does not cause wheel slip so that rapid acceleration could be achieved.

4.5.2 Constant-speed operation under speed limit

In sections where speed is significantly limited compared to other sections due to speed restrictions for curves, turnouts, signal aspects, etc., then the time required to travel through that section increases significantly. Running at faster speeds in order to compensate for the increase in running time results in a large amount of energy consumption. Therefore, the aim should be to drive at lower speeds in unrestricted sections closer to the limits in low-speed sections. In general, when coasting through sections with limited speed, speed decreases, so it is advantageous to operate as close as possible the speed limit while taking into account gradients.

4.5.3 Coasting toward speed limit

Prior to speed limits for curved sections, turnouts, signal aspects, etc., speed needs to be reduced accordingly. However, if brakes are used for this, the kinetic energy of the train is consumed,

Table 1 Energy-saving operation method for cruising [3]

<table>
<tr><th></th><th>Small-step saw-toothed</th><th>Mainly constant-speed operation</th><th>Combined constant-speed operation</th></tr>
<tr><td>Sharp uphill</td><td>High-efficiency notch power running</td><td rowspan="4">Constant-speed</td><td>High-efficiency notch power running</td></tr>
<tr><td>Gradual uphill</td><td rowspan="3">Small-step</td><td rowspan="2">Constant-speed</td></tr>
<tr><td>Flat</td></tr>
<tr><td>Gradual downhill</td><td rowspan="2">Coasting</td></tr>
<tr><td>Sharp downhill</td><td>Coasting</td><td>Coasting</td></tr>
</table>

which results in major energy loss. In other words, extra powering energy used prior to this is lost as kinetic energy coming into the limited-speed section. Therefore, deceleration through coasting can be used to avoid this loss, if running time permits.

5. Energy-saving driving test

5.1 Test running conditions

Energy-saving driving tests were conducted based on the theoretical study in the previous section. Figure 7 shows an overview of the driving method of the energy-saving driving test. In cruising mode, constant-speed operation or small-step saw-toothed operation was used to keep the speed generally constant, and we also implemented other driving methods that almost certainly reduce energy consumption. Additionally, since adjustments are made in consideration of maneuverability (including around the time of cruising) according to each driving method, the driving method is also partially different in areas other than cruising. Therefore, energy-saving driving tests do not simply show the differences in energy-saving driving methods. We also collected data from normal commercial running and compared it with these data.

As shown in Table 1, the following three driving methods for cruising were implemented: small-step saw-toothed operation, mainly constant-speed operation, and combined constant-speed operation. The powering during small-step saw-toothed operation was set to 8-9 N, which had a particularly high motor efficiency. In small-step saw-toothed operation, the speed range was set to be the average speed ± 2 [km/h]. The driving was specified to run between the stations with specified passing times in the time.

In addition, an analysis of energy consumption during normal running confirmed that wind had a large influence. Therefore, data with wind speed exceeding 2 [m/s] was excluded, regardless of the wind direction.

5.2 Test results

Figure 10 shows a comparison of energy consumption during test running. The mass to be towed of the evaluated train varies each day, so the value that was obtained by dividing the power consumption by the train set mass (sum of locomotive mass, towed cars mass, and their load) was used as the energy consumption for the evaluation. The average of seven test runs and 61 normal driving are shown in Fig.10. Note that the frequency distribution of 61 normal driving is shown in Fig. 11.

When comparing the energy consumption, the results of the energy-saving driving test were about 7-14% smaller than the average value of the normal driving. In the energy-saving driving test, since trains were operated with a strong awareness of energy-saving driving, it is almost certain that the high energy-saving effect was obtained due to the effects of both energy-saving driving during cruising and energy-saving driving other than during cruising. In the energy-saving driving test results, the energy consumption of constant-speed operation is large. The reason for this seems that, when proceeding to the terminal station, the mainly constant-speed operation maintained as constant a speed as possible, whereas other driving methods proceeded with coasting.

Additionally, although a quantitative evaluation of maneuverability was not yet achieved, there was frequent notch operation in small-step saw-toothed operation, and we observed that this created a maneuverability burden when trying to accurately match the target speed. In the energy-saving operation test, since there was an instructor-driver either driving or on the side, small-step saw-toothed operation was achieved. Therefore, it is necessary to carefully evaluate the maneuverability burden to achieve small-step saw-toothed operation in normal driving conditions where one person is on board.

6. Energy simulation

6.1 Reproduction of test run

In the energy-saving driving test, driving instructions were given based on energy simulations for the driving modes of small-step saw-toothed operation, mainly constant-speed operation, and combined constant-speed operation. However, there may be difference between the assumed energy simulation and actual driving. Therefore, to validate the simulation, we conducted energy simulation that replicated the results of the energy-saving driving test. Then, we compared the results of the combined constant-speed driving tests with the simulation that replicated the driving method. Figure 12 shows a comparison of energy consumption, and Fig. 13 shows a comparison of speed curves. The difference in energy consumption between the simulation and energy-saving driving test was about 2%. As the result, we confirmed the validity of the energy

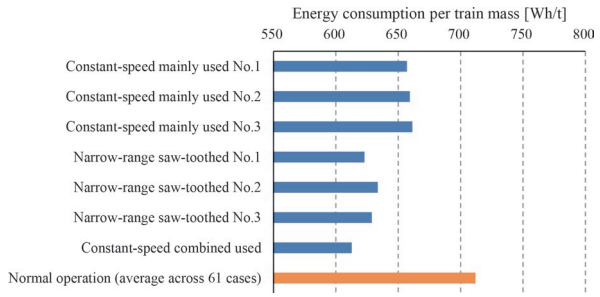

Fig. 10 Comparison of energy consumption in energy-saving operation test

Fig. 11 Distribution of energy consumption during normal operation

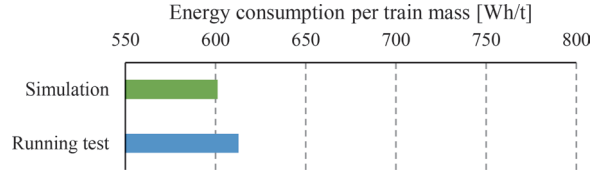

Fig. 12 Comparison of energy consumption in running tests and energy simulation

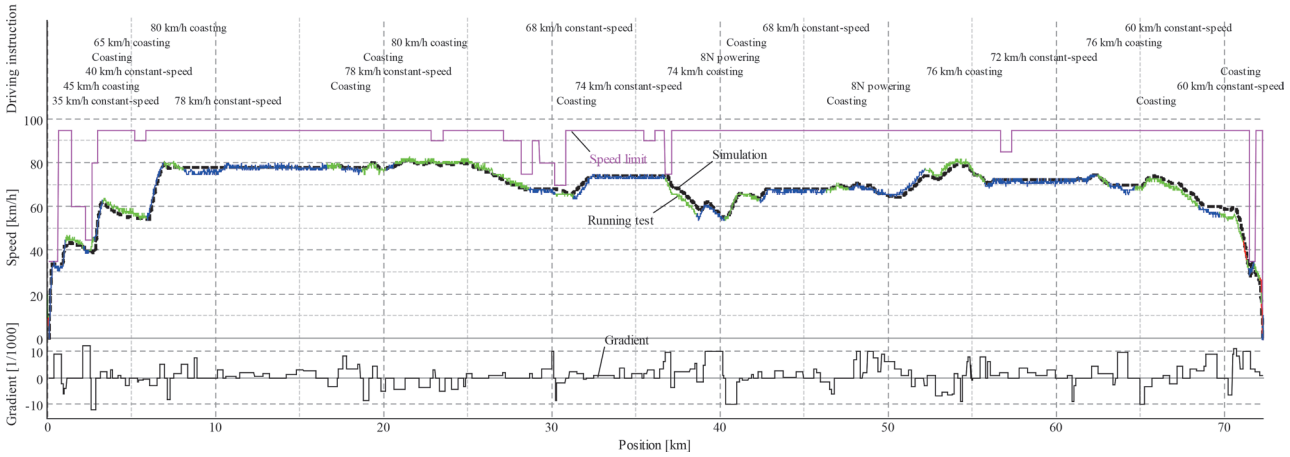

Fig. 13 Comparison of running test results and energy simulation speed shifts (combined constant-speed operation) [3]

simulation by reproducing the running test results.

6.2 Comparison of energy-saving driving methods

In energy-saving driving tests, since there are variations in running conditions such as daily differences in mass to be towed and wind effects, changes in the process of trial and error in energy-saving driving methods, and scatterings in the timing of driving instructions, it is difficult to compare energy-saving driving methods under the same conditions. Therefore, we compared energy-saving driving methods using energy simulations. For the simulation of saw-toothed operation and small-step saw-toothed operation, we specified the point where the notch change operation was performed by using manual driving function so that the average speed would be about the speed according to the operating time between stations with specified passing times. The maximum notch of 14 N was set for the powering in saw-toothed operation, and a high-motor efficiency notch of 8 N was set for the powering in small-step saw-toothed operation. In saw-toothed operation, the speed range was set to be the average speed ± 15 [km/h]; and in small-step saw-toothed operation, the speed range was set to be the average speed ± 2 [km/h]. For the simulation of constant-speed operation, we constructed a constant-speed operation calculation function and specified the average speed according to the operating time between stations with specified passing times. The constant-speed operation calculation function creates a constant-speed operation curve and calculates power consumption based on the motor output balancing with the train resistance. It should be noted that the running times were set to be as close as possible in the simulations, though some deviations may have occurred. Additionally, due to speed limits and passage time adjustments, driving in some sections deviated from the above-mentioned general rules. However, for the method of proceeding to the terminal station, which was difficult to compare in the energy-saving driving tests, adjustments were made so that the approach speed would be the same regardless of the driving method.

Figure 14 shows a comparison of energy consumption, and Fig. 15 shows a comparison of speed and driving. As shown in Fig.14 and Fig.15, it is found that the small-step saw-toothed operation consumed the least energy, followed by the combined constant-speed operation. From the energy-saving driving test results and the maneuverability, it seems that the combined constant-speed operation method was good in terms of energy saving and maneuverability.

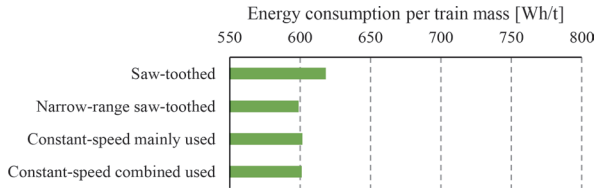

Fig. 14 Comparison of energy consumption for each energy-saving operation method

7. Conclusion

In this report, we focused on cruising, which is a main component of freight train operation, and we studied energy-saving driving methods based on running resistance characteristics and motor efficiency characteristics. Although energy-saving effects seem to fluctuate depending on the running speed and the mass to be towed, it was confirmed through energy-saving driving tests that small-step saw-toothed operation and combined constant-speed operation, which combined constant-speed operation and coasting, were best for saving energy consumption. Additionally, we used energy simulations whose validity was confirmed by energy-saving driving tests to compare the energy consumption of each method after matching other conditions. These simulations confirmed that small-step saw-toothed operation and combined constant-speed operation were best for saving energy consumption. These results clarified that driving methods which maintain a generally constant speed were best for saving energy, and suggested that constant-speed operation was better in terms of maneuverability as well. Based on this, we propose an energy-saving driving method for cruising freight trains that appropriately combines constant-speed operation and coasting according to operating conditions such as gradient and speed.

In future, we plan to develop a driver advisory system that proposes driving methods according to operating conditions such as gradient and speed, to realize energy-saving driving.

Acknowledgment

We would like to express our gratitude to the Japan Freight Railway Co. Ltd. for its cooperation in implementing the running tests in this study.

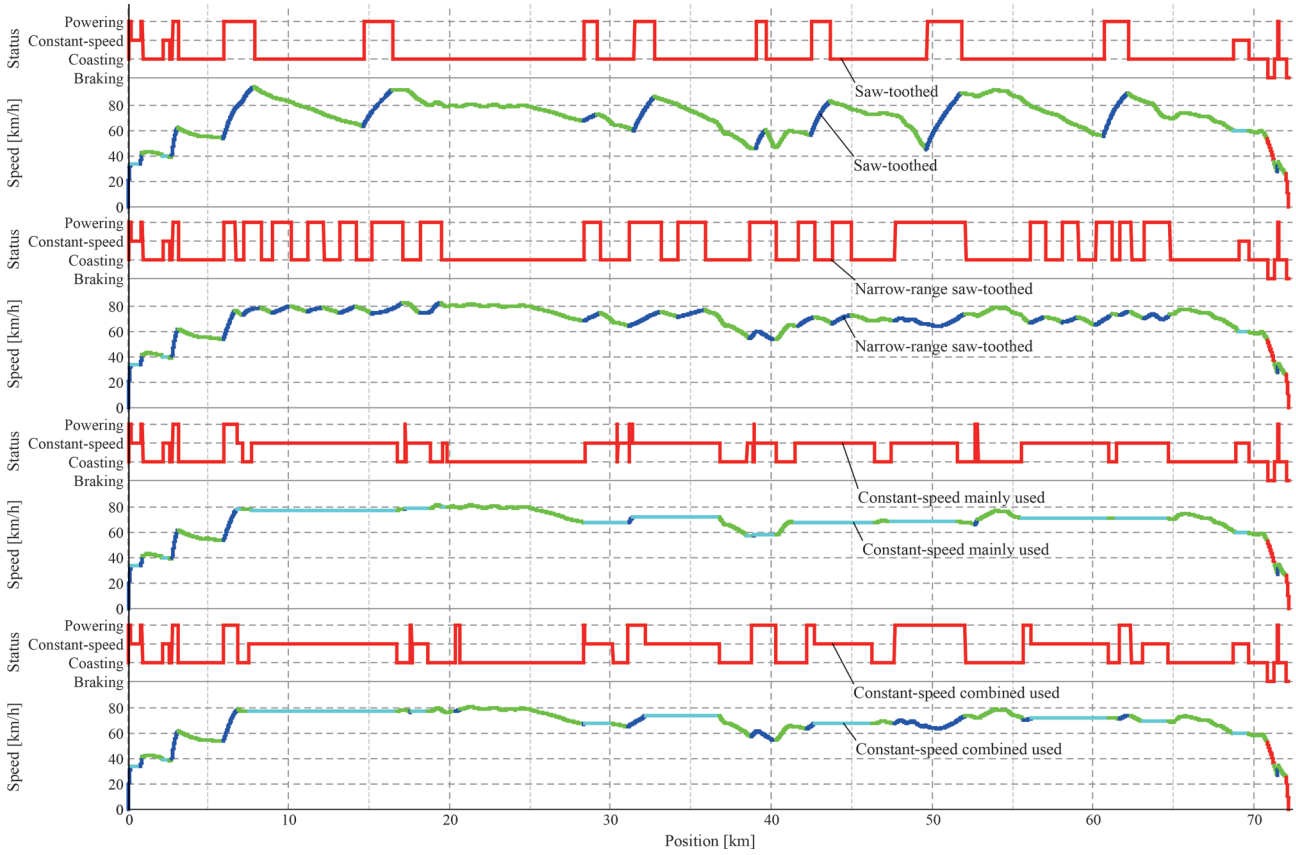

Fig. 15 Comparison of speed shifts for each energy-saving operation method [3]

References

[1] Furukawa, A., Shigeeda, H., Muramoto, K., "Research and Development at RTRI toward the Achievement of Net-Zero by 2050," *Ascent*, No. 11, pp. 3-8, 2022.

[2] Scheepmaker, G. M., Goverde, R. M. P., Kroon, L. G., "Review of energy-efficient train control and timetabling," *European Journal of Operational Research*, Vol. 257, pp. 355-376, 2017.

[3] Ogawa, T., "Energy Saving Driving Method for Freight Railway Considering Running Resistance and Motor Efficiency," *IEEJ Transactions on Industry Applications*, I.E.E. Japan, Vol. 142, No. 1, pp. 50-57, 2022 (in Japanese).

Author

Tomoyuki OGAWA, Ph.D.
Senior Researcher, Hydrogen and Sustainable Energy Laboratory, Vehicle Technology Division
Research Areas: Energy Simulation, Analysis of Train Information

Method for Evaluating Performance of Wheel Slide Protection Algorithm Using a Hybrid Simulator

Daisuke HIJIKATA **Yuta KIZAKI** **Shin-ichi NAKAZAWA**
Braking Systems Laboratory, Vehicle Technology Division

In performance evaluation of Wheel Slide Protection (WSP) systems, adjustment of the control algorithm by an on-track test is the most important process. However, since it is not easy to stably reproduce low adhesion conditions between wheels and rails in on-track tests, the control algorithm must be adjusted under different adhesion conditions for each run. Therefore, to solve this issue, we have developed a hybrid simulator that combines a real-time computer and pneumatic brake device. The developed simulator can specify arbitrary adhesion conditions, vehicle models, and control algorithms. This paper describes a method for evaluating the performance of the control algorithm for WSP using the hybrid simulator.

Key words**:** *brake, Wheel Slide Protection, adhesion, simulator, performance evaluation*

1. Introduction

Wheels of rail vehicles, which accelerate and decelerate using the force acting on contact surface between steel wheels and rails, have low rolling resistance and excellent energy efficiency. On the other hand, they tend to slip. This characteristic of wheels may lead to slippage in braking when the rail is wet, which may extend the stopping distance, or lead to wheel flats due to wheel locking. In particular, the extension of stopping distances is a major safety risk. Wheel flats are also a source of undesired noise and vibration, so that vehicles found to have wheel flats require unplanned wheel rolling (work to restore the tread profile), which consequently has a significant impact on maintenance plans. To prevent these problems, many recent rail vehicles are installed with a Wheel Slide Protection (hereafter referred to as WSP) in the braking system.

A WSP device for pneumatic brakes detects wheel sliding during braking and exhausts brake cylinder (hereinafter referred to as "BC") pressure to quickly return the wheel circumferential speed to the vehicle speed for re-adhesion, and then returns the BC pressure to the predetermined value. However, since exhausting the BC pressure leads to releasing the brake, it is important to both ensure braking performance and prevent wheel flats. For this reason, WSP algorithms with various characteristics have been proposed [1, 2].

In general, the performance of WSP is verified by intentionally causing wheel sliding in on-track tests. Specifically, low adhesion conditions are first created by spraying water over the wheel/rail contact surface from the running car. Then the stopping distance and the occurrence of wheel flats are measured to determine whether the WSP functioned effectively.

Pneumatic brakes are an extremely important application that are also used for emergency braking, and verification of their performance through on-track testing is essential to ensure safety. However, many factors affect slipperiness (e.g., amount, position, and temperature of water spray, wheel and rail surface conditions), making it very difficult to repeat tests under exactly the same conditions. In addition, on-track testing requires an enormous amount of time and effort, and in practice, it is necessary to determine performance differences due to WSP algorithms within a limited number of tests.

Therefore, the authors are developing a hybrid simulator for WSP that combines the advantages of actual machines and computers [3, 4]. This simulator is a bench test environment in which the responsiveness of the pneumatic brake is reproduced on the actual machine and the other parts are simulated by a computer. Low-adhesion conditions can be set arbitrarily by testers, and a large number of tests can be easily conducted. Comparison and verification of WSP algorithms in advance of on-track testing, lead to reduction of the number of on-track tests.

This paper describes the mechanism of the developed simulator and the performance evaluation method of the WSP algorithm utilizing its functions.

2. Hybrid simulator for WSP

2.1 Overall configuration

The overall diagram of the hybrid simulator for WSP (hereinafter referred to as the 'hybrid simulator') is shown in Fig. 1 and the block diagram in Fig. 2. The hybrid simulator consists of an actual machine and a computer.

The real machine part reproduces the compressed air flow of the actual vehicles and consists of the same pneumatic brake equipment as the actual vehicle, from the air reservoir to the constant volume container simulating a BC. The responsiveness can be varied by changing the length of the air piping connecting the equipment. Pneumatic brake equipment is provided for four independent axles (per one vehicle).

The computer part simulates elements other than the actual machine and consists of a real-time computer, an operating PC, and BC pressure sensors. Inside the real-time computer, the experimenter can arbitrarily set the numerical model of vehicle, WSP algorithm, and wheel/rail adhesion conditions (hereinafter referred to as 'adhesion conditions'). The braking force, which is calculated based on the measured BC pressure and the brake rigging specifications, are applied to the vehicle model. In the vehicle model, the deceleration motion is calculated based on the assumed vehicle specifications. The calculation of the deceleration motion uses the pre-defined adhesion conditions and the WSP algorithm. For example, when an axle under deceleration in the computer meets the slide detection condition set in the WSP algorithm, an operation command is immediately output to the WSP dump valve in the actual machine to exhaust the compressed air in the BC. The change in BC pressure is always reflected in the next calculation step and the deceleration motion is recalculated. This calculation loop is repeated until the vehicle stops (Fig. 3).

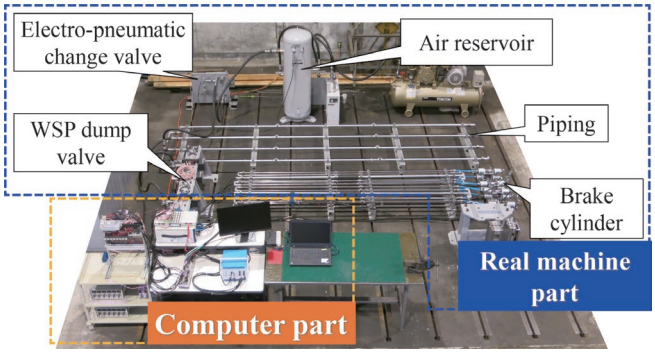

Fig. 1 Overall view of hybrid simulator

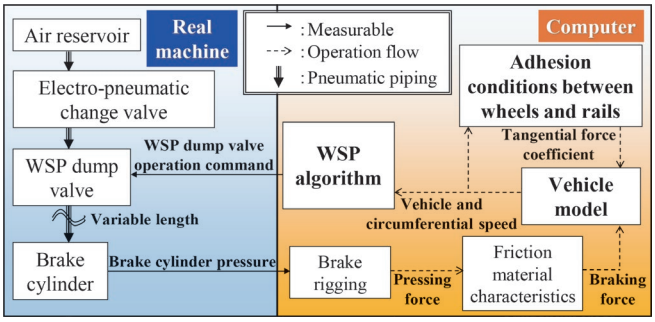

Fig. 2 Block diagram of hybrid simulator

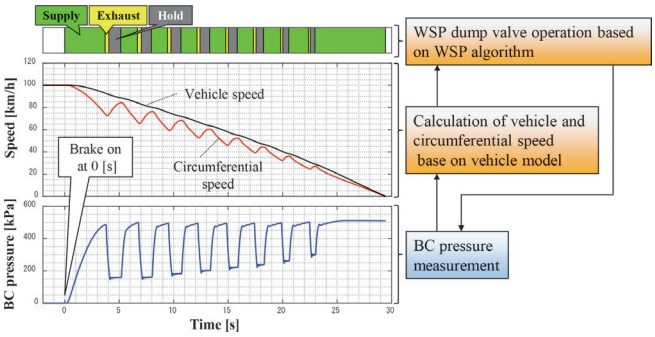

Fig. 3 Interaction of real machine with a computer

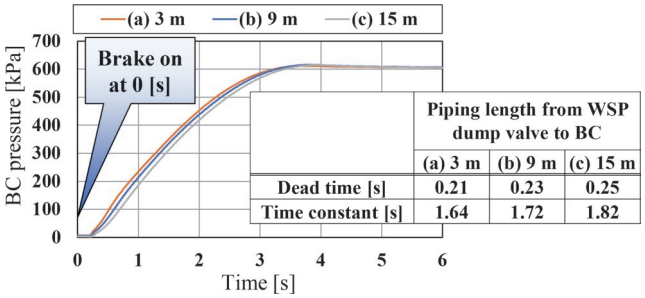

Fig. 4 Relationship between piping length and BC pressure

2.2 Responsiveness of pneumatic brake equipment

The response characteristics of BC pressure when detecting brake commands and when exhausting, holding, and supplying air are frequently switched during WSP and vary greatly depending on the length and volume of the piping. Since it is difficult to model this on a computer, an actual pneumatic brake equipment was used so that the structure was designed to allow the response to be adjusted by changing the piping length. The relationship between the piping length from the WSP dump valve to the BC and the BC pressure response characteristics is shown in Fig. 4. As shown in Fig. 4, the time constant and the time-delay increase with extending piping length. This indicates that the response characteristics can be adjusted by the piping length.

2.3 Vehicle model

The vehicle model in this paper specifies a motion in which the vehicle speed and wheel circumferential speed are slowed down by a braking force applied to the running vehicle and a tangential force generated between the wheels/rails. Only forward and backward motion of the vehicle on a straight and level track is considered and motion of vertical and sleeper direction are not considered. The braking force is calculated from the measured value by the BC pressure sensor, the specifications of the brake rigging, and the friction material characteristics. The tangential force coefficient between the wheel and rail is calculated from the adhesion conditions described later.

A schematic diagram of the vehicle model (one car) is shown in Fig. 5, and the definitions of symbols are given in Table 1. Equations (1) to (4) define the mathematical formulas involved in deceleration motion, where the subscript i represents the axle position. Equation (1) represents the translational motion of the vehicle and (2) represents the rotational motion of each wheel set. Equation (3) shows that the tangential force is the product of the tangential force coefficient and the axle load, and (4) shows the slip rate.

Each of the four axles has independent rotational degrees of freedom, and the vehicle is decelerated by the resultant force of tangential forces on four axles. If a coupler force is applied to the end of the vehicle, the deceleration motion can be represented taking into account the force received from the adjacent vehicle.

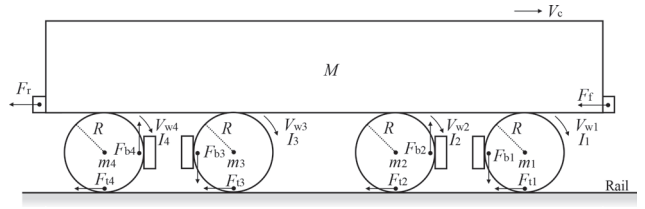

Fig. 5 Schematic diagram of vehicle model

Table 1 Symbol definitions

Symbol	Definition	Symbol	Definition
V_c	Vehicle velocity	g	Gravitational acceleration
V_{wi}	Circumferential velocity	μ_i	Tangential force coefficient
M	Car body mass	F_{ti}	Tangential force
m_i	Wheelset mass	F_{bi}	Braking force
I_i	Momemt of inertia of wheelset	η_i	Slip rate
R	Wheel radius	F_f, F_r	Coupler force

※Subscript " i " represents the wheelset position

$$(M + m_1 + m_2 + m_3 + m_4)\frac{dV_c}{dt} = -(F_{t1} + F_{t2} + F_{t3} + F_{t4}) - (F_f + F_r) \quad (1)$$

$$\frac{I_i}{R}\frac{dV_{wi}}{dt} = F_{ti}R - F_{bi}R \tag{2}$$

$$F_{ti} = \mu_i\left(\frac{M}{4} + m_i\right)g \tag{3}$$

$$\eta_i = \frac{V_c - V_{wi}}{V_c} \cdot 100 \tag{4}$$

2.4 WSP algorithm

WSP algorithm selects one of the three operations of exhausting, holding, and supplying BC pressure, depending on the deceleration of the wheel. These actions are implemented by a combination of command to AV (apply valve) and RV (release valve) in the WSP dump valve. WSP algorithms with various characteristics have been proposed [1, 2]. Methods for detecting wheel deceleration include slip rate detection, speed difference detection and deceleration detection, and their combinations are also used. As an example, Fig. 6 shows the operation of slip rate WSP and detection conditions.

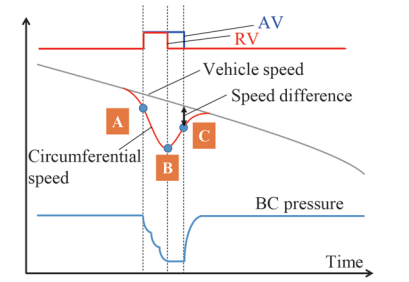

Detection point	WSP dump valve command	AV	RV	Example of condition
A	Exhaust	ON	ON	Slip rate > 15%
B	Hold	ON	OFF	Circumferential deceleration < 2 km/h/s
C	Supply	OFF	OFF	Speed difference < 3 km/h

Fig. 6 Schematic diagram of WSP algorithm

2.5 Adhesion condition

The adhesion condition in this paper is defined as a method for giving tangential force coefficients derived from several relational equations. As shown in Fig. 7, it is generally known that tangential force coefficient is almost proportional to the slip rate in the micro-slip area but unstable in the macroscopic slip area. While it is difficult to actually reproduce unstable and unrepeatable phenomena, computers have advantage of being able to reproduce them precisely with known quantities based on empirical or theoretical rules.

This section describes the tangential force coefficients derived from the three relational equations of slip rate, speed and running position, and how they are set up.

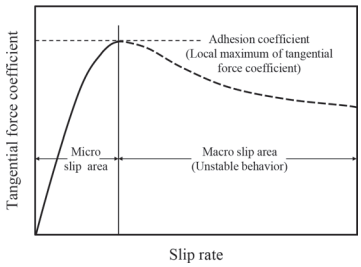

Fig. 7 Relationship between slip rate and tangential force coefficient

2.5.1 Relationship between slip rate and tangential force coefficient

The relationship between the slip rate and tangential force coefficient defines the most basic properties of the adhesion conditions, such as whether the rail surface is dry or wet. Specifically, it corresponds to specifying the adhesion coefficient (the local maximum value of the tangential force coefficient in Fig. 7), the slip rate at which the coefficient is taken, and the behavior in the macro-slip area. In this paper, we used the relationship expressed in (5) with reference to Reference [5], since it is easy to handle and can express various characteristics.

$$\mu_\eta = C\sin\left(B\tan^{-1}\left(A\frac{\eta}{100}\right)\right) \tag{5}$$

where η is the slip rate and A, B, and C are arbitrary constants. The basic properties are that the larger A, the narrower the micro-slip area (the slip rate with the maximum value becomes smaller), and the larger B, the larger the attenuation in the macro-slip area. C is the value of the adhesion coefficient. Combinations of constants A, B, and C and examples of waveforms are shown in Fig. 8.

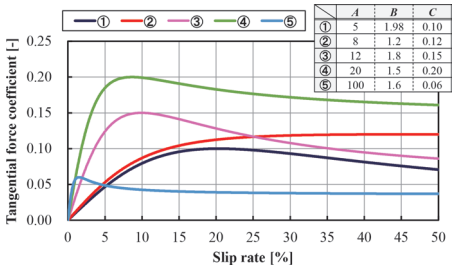

	A	B	C
①	5	1.98	0.10
②	8	1.2	0.12
③	12	1.8	0.15
④	20	1.5	0.20
⑤	100	1.6	0.06

Fig. 8 Waveform examples of tangential force coefficient

2.5.2 Relationship between speed and adhesion coefficient

The relationship between speed and adhesion coefficient represents the property that the adhesion coefficient decreases with increasing vehicle speed. In this study, (6) was used for the Shinkansen and (7) for a 1067 mm gauge line, which have been experimentally obtained in previous studies [6]. Note that v is the vehicle speed (km/h).

$$\mu_v = \frac{13.6}{(v + 85)} \tag{6}$$

$$\mu_v = \frac{32.74}{(v + 187)} \tag{7}$$

2.5.3 Relationship between running position and adhesion coefficient

In an actual vehicle environment, there are characteristics unique to the running position, such as water and fallen leaves, rail joints, rail surface roughness. Therefore, the adhesion coefficient changes at each running position. To consider this change of the

adhesion coefficient, the simulation provides conditions that are closer to the actual vehicle environment. For example, the periodic fluctuation with respect to the running position is expressed by (8).

$$\mu_x = D \sin\left(\frac{2\pi f x}{X}\right) + E \tag{8}$$

where x is the running position, D is the amplitude of the fluctuation, E is the reference value (the value when there is no fluctuation), and f is the number of cycles per distance X. Although it is desirable to give the assumed fluctuation based on the on-track test, but it is very difficult to extract fluctuation of adhesion coefficients depending on running position independently based on the on-track test results. Therefore, the experimenter arbitrarily decided the relationship between the running position and the adhesion coefficient depending on the assumed running environment. Here, as a simple example, we apply periodic fluctuations with respect to the running position. It is noted that there is also an example [7] of a study of a method that gives fluctuations with randomly changing amplitude and period within a certain range.

2.5.4 Final tangential force coefficient

A conceptual diagram of the comprehensive tangential force coefficient that integrates the three relationships in 2.5.1 through 2.5.3 is shown in Fig. 9. The specific tangential force coefficient is expressed in (9).

$$\mu = \mu_\eta \frac{\mu_v}{\mu_v(0)} \frac{\mu_x}{E} \tag{9}$$

μ_v and μ_x are normalized by dividing by the value at vehicle speed $v = 0$ and the reference value E, respectively, and then taking the product. The possible values of μ are expressed as points in a three-dimensional space with the slip rate and the running position as axes, as shown in the lower part of Fig. 9. The tangential force coefficient obtained by a given braking action can draw the locus of a point moving cubically across the surface of the figure. It is useful to visually understand how the sliding evolved and converged and how the tangential force coefficient was utilized for the set adhesion conditions.

Figure 10 shows an example of results of the hybrid simulator test based on the tangential force coefficient setting method described above. Note that from the top in the figure are the WSP dump valve motion command, speed, and BC pressure. It is found that the complex WSP behavior is reproduced by linking the actual measured values with the computer's internal model. Focusing on speed, it can be seen that the higher the vehicle speed is in the high-speed range, the more likely it is to slide, reflecting the property of the vehicle to slide.

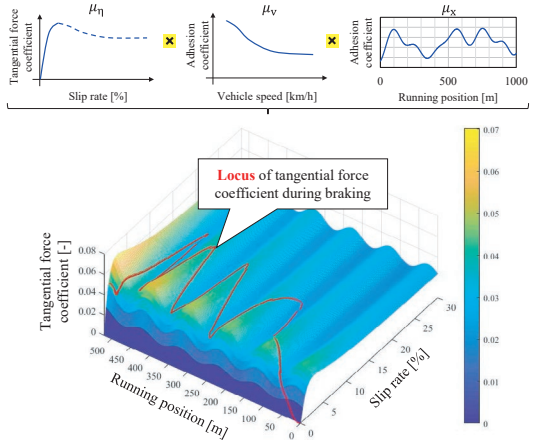

Fig. 9 Conceptual diagram of the determinate tangential force coefficient

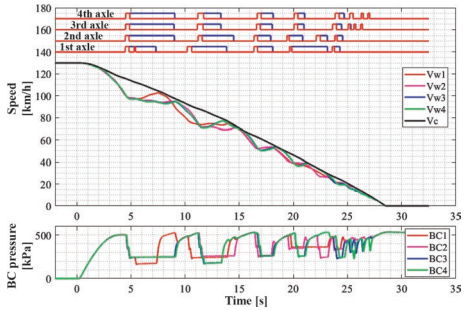

Fig. 10 An example of hybrid simulator test result

3. A method for evaluating performance of WSP algorithms

As described so far, the hybrid simulator reproduces the response characteristics of pneumatic brake equipment in the real machine part, while the vehicle model, WSP algorithm, and adhesion conditions can be specified arbitrarily in the computer part. In addition, the burden of testing is very small compared with on-track testing, so that a large number of tests can be easily conducted. This paper describes a method for evaluating performance of WSP algorithms by utilizing this advantage and statistically analyzing the results of a large number of simulator tests.

3.1 Test conditions

The piping length of the pneumatic brake equipment was 15 m shown in Fig. 4. The vehicle model was a one-car model with no coupler force, and the vehicle specifications were shown in Table 2. The constants in (5) were set to $A = 100$, $B = 1.6$, and $C = 0.25$ for the relationship between the slip rate and tangential force coefficient, while (7) for conventional lines was used for the relationship between speed and adhesion coefficient. The initial braking speed was set at 130 km/h.

The relationship between the running position and the adhesion coefficient was assumed to be that the constants in (8) were set to $D = 0.2$, $E = 1$, and $X = 100$, and the adhesion coefficient periodically varied with the running position. This means a sine wave with a reference value of 1, an amplitude of 0.2 and f cycles per 100 m. Here, by giving the value of f from 0 to 10 in increments of 0.1, 101 patterns of adhesion conditions with different cycles are generated.

Table 2 Vehicle specifications

Definition	Value	Unit
Car body mass	20000	kg
Wheelset mass	1200	kg
Moment of inertia of wheelset	165	kgm^2
Wheel radius	0.43	m
Fixed BC pressure	520	kPa
Conversion factor from BC pressure to braking force	36	N/kPa

The waveforms for $f = 0$, 0.1, 0.5, 1, 5, and 10 are shown respectively in Fig. 11.

Two WSP algorithms were applied for comparison, "SR10" with a slip rate of 10% and "SR15" with a slip rate of 15% at detection point A in the slip rate WSP described in 2.4.

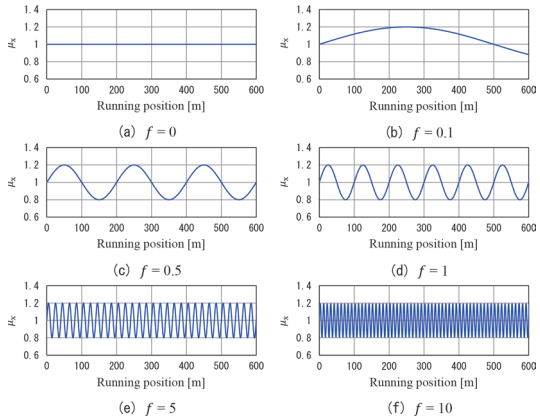

Fig. 11 Relationship between *f* and μ_x

3.2 Test results

Simulator tests were carried out by applying two WSP algorithms separately to each of the 101 patterns of adhesion conditions, resulting in a total of 202 stopping distances. The relationship between f and stopping distance for each WSP algorithm is shown in Fig. 12. With a constant fluctuation, both SR10 and SR15 showed a similar trend of an increase in stopping distance from $f = 0$ (no fluctuation in adhesion coefficient with running position) to around $f = 1.5$, followed by a gradual decrease. When compared under the same conditions, SR10 tended to have shorter stopping distances throughout. Note that when $f = 0.1$, both SR10 and SR15 show significantly shorter stopping distances. This is because, as shown in Fig. 11, μ_x exceeded the reference value of 1 up to 500 m, and sliding did not occur due to the given high adhesion coefficient.

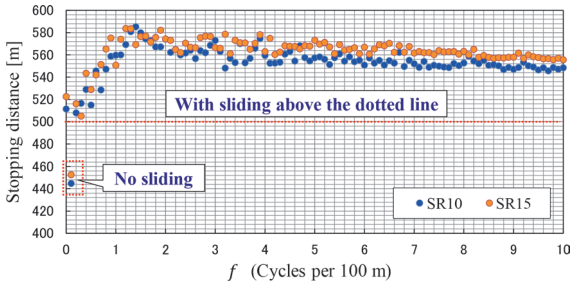

Fig. 12 Relationship between *f* and stopping distance

3.3 Evaluation by statistics

A histogram of the results for 100 stopping distances for each WSP algorithm is shown in Fig. 13, and the statistics are shown in Table 3. Note that $f = 0.1$, where no sliding occurred, is excluded.

There was no significant difference between the maximum and minimum stopping distances for each of the two algorithms. In addition, the trend of gradual decrease in frequency from the mode to the maximum and the trend of marked decrease in frequency from the mode to the minimum were also similar for both algorithms. On the other hand, the mean, and the mode of the stopping distance of SR10 is about 10 m shorter than that of SR15, so that it can be said that SR10 stops in a relatively short distance in the results of the tests. This is probably because SR10, detecting sliding at a slip rate of 10%, can utilize a higher tangential force coefficient for a longer time than SR15 as shown in Fig. 14, where the constants in (5) are $A = 100$, $B = 1.6$, and $C = 0.25$.

Thus, statistical analysis of a large number of simulator test results provides the range, frequency, and distribution of possible braking distances, and makes it easier to understand the nature of the WSP algorithm than in the past. For example, it can be easily obtained that the percentage of stopping distances of 575 m or more is 3% for SR10 and 12% for SR15. Hence, it can be possible to quantitatively indicate the possibility of meeting certain criteria. It is also possible to take into account not only the short stopping distance but also the small dispersion, i.e., whether the stability is also compatible. The above is a new performance evaluation method for WSP algorithms that takes advantage of the hybrid simulator which allows arbitrary adhesion conditions to be specified and a large number of tests to be easily performed.

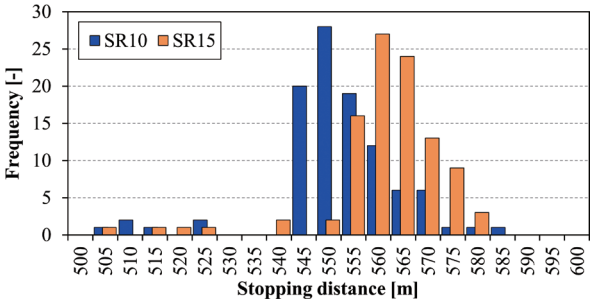

Fig. 13 Histogram of stopping distances

Table 3 Histogram statistics

	WSP Algorithm	
	SR10	SR15
Max [m]	585.2	583.7
Mean [m]	554.7	563.4
Min [m]	507.9	505.0
Mode [m]	550～555	560～565
Variance	159.6	146.9
Percentage over 575 [m]	3%	12%

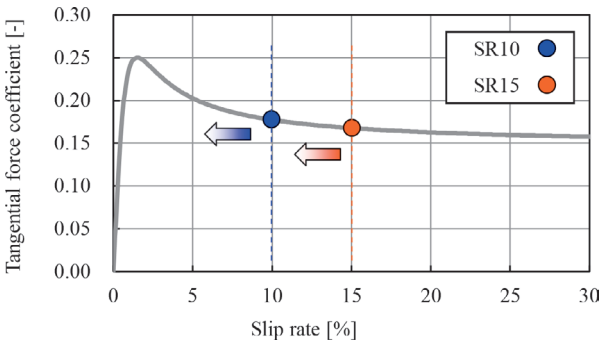

Fig. 14 Relationship between sliding detection slip ratio and tangential force coefficient

4. Summary

The mechanism of the original hybrid simulator for WSP, which combines actual pneumatic brake equipment and a real-time computer, was introduced. The developed simulator allows any number of low adhesion conditions to be specified and a large number of tests to be easily carried out. Using this feature, we presented a new evaluation method that shows the distribution trend of stopping distances for the test target WSP algorithm. It could be used as a tool for developing new WSP algorithms and as a method to reduce the number of on-track tests by confirming the performance of the WSP algorithm prior to on-track testing.

In this paper, adhesion conditions were treated as periodically fluctuating depending on the running position, but the actual vehicle environment is not limited to this and should involve more complex fluctuations. It is also important to conduct basic research to learn more the physical phenomena between the wheel and the rail, to understand the actual conditions in the actual vehicle environment, and to develop an evaluation method that reflects these conditions. In addition, we will develop the simulator by improving the functionality of the real machine part and the modeling accuracy of the computer part and will utilize this method in research and development to improve the safety of braking systems.

References

[1] Kumagai, N., Hasegawa, I., Uchida, S., Watanabe, K., "The Slip Rate Wheel Slide Control System Using Synchronized Speed Pulse Computation for Shinkansen Brake," *Transactions of the JSME*, Vol. 70, No. 689, pp. 135-141, 2004 (in Japanese).

[2] Nakazawa, S., "Development of a New Wheel Slide Protection System Using a New Detection Algorithm," *Quarterly Report of RTRI*, Vol. 52, No. 3, pp. 136-140, 2011.

[3] Hijikata, D., Kizaki, Y., Nakazawa, S., "A Hybrid Simulator for Wheel Slide Protection Combining Pneumatic Brake Hardware," *J-RAIL*, 2021 (in Japanese).

[4] Hijikata, D., "Evaluating Wheel Slide Protection Performance Responding to Train Braking," *Ascent*, No. 10, pp. 19-23, 2022.

[5] Maron, C., Klein, K., Schubert, S., "Dynamic Braking with an Electric Parking Brake System," presented at *EuroBrake 2019*, Dresden, Germany, May 21-23, 2019, EB2019-IBC-007.

[6] Ohyama, T., "Behavior of Adhesion Force at Higher Speeds from the Viewpoint of Contact Condition between Wheel and Rail - Correspondence of Experimental Results under Dry Friction to Two-Dimensional Contact Theory -," *Railway Technical Research Report*, No. 1261, p. 7, 1984 (in Japanese).

[7] Hijikata, D., Spiess, P., Bueche, B., Kroeger, F., "Performance Evaluation of Wheel Slide Protection by Using Simulation and Statistical Analysis," presented at *EuroBrake 2018*, The Hague, Netherlands, May 22-24, 2018, EB2018-VDT-032.

Authors

Daisuke HIJIKATA
Assistant Senior Researcher, Braking Systems Laboratory, Vehicle Technology Division
Research Areas: Wheel Slide Protection Control, Performance Evaluation of Brake System

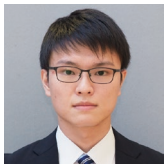

Yuta KIZAKI
Researcher, Braking Systems Laboratory, Vehicle Technology Division
Research Areas: Wheel Slide Protection Control, Performance Evaluation of Brake System

Shin-ichi NAKAZAWA
Senior Chief Researcher, Head of Braking Systems Laboratory, Vehicle Technology Division
Research Areas: Brake System, Wheel Slide Protection Control

Proposal of Backing Ring for Reducing Fretting Wear of Axle Journal Bearings

Yoshiaki OKAMURA **Daisuke SUZUKI**
Lubricating Materials Laboratory, Materials Technology Division

Shinya FUKAGAI
Frictional Materials Laboratory, Materials Technology Division

Ken TAKAHASHI
Lubricating Materials Laboratory, Materials Technology Division

Takafumi NAGATOMO
Lubricating Materials Laboratory, Materials Technology Division (Former)

It is necessary to reduce fretting wear of railway axle journal bearings caused by very slight relative slips between the contact surfaces of the inner ring and the backing ring. This paper proposes a backing ring with grooves in the circumferential direction on its oil seal sliding surface to obtain even contact pressure distributions in the radial direction between them. Results of a rotation test on a full-scale railway axle bearing using the proposed backing ring showed that this proposal is effective in suppressing fretting wear.

Key words**:** *axle bearing, fretting, wear, pressure distribution, contact pressure, grooving*

1. Introduction

Axle journal bearings for railway vehicles support both radial loads resulting from the vehicle weight and axial loads generated while railway vehicles are running. When an axle bearing rotates under radial loads, the axle journal bends due to rotary bending. Fretting occurs because of the minute relative sliding motion in the contact area between inboard inner rings and backing rings for positioning axle bearings in the axial direction. When metallic wear particles from fretting penetrate into axle bearings, wear and lubricant deterioration occur. Additionally, misalignment of the axial mounting position of axle bearings can arise. The penetration of fretting wear particles can be mitigated by inserting an O-ring [1] or a rubber-attached spacer [2] between inner rings and backing rings. However, neither of these methods has succeeded in preventing the occurrence of fretting itself.

To gain insight into how fretting between the inner ring and backing ring of an axle bearing develops, the authors carried out a test reproducing fretting using a full-scale axle bearing to confirm the state of wear on the inner ring and the backing ring, measured the contact surface pressure distribution between them, and investigated the effect of the contact surface pressure on the fretting accordingly [3]. Results showed that (1) fretting wear of the inner ring and the backing ring is more noticeable on the outer side of their contact surfaces in the radial direction, where the contact pressure is higher, because the deformation of the backing ring press-fitted onto the axle affects the contact state with the inner ring, resulting in an uneven contact pressure distribution between them and that (2) the fretting wear can be affected by the contact pressure that fluctuates as the axle rotates in addition to the relative sliding motion on their contact surfaces caused by rotary bending due to axle deflection. These results suggest that reducing the contact pressure on the outer radial side and making the contact pressure distribution uniform in the radial direction can reduce fretting wear.

In this report, firstly, the shape of backing rings was investigated to make the contact pressure distribution as uniform as possible by a finite element method (FEM) analysis. Then, the contact pressure distribution between the inner ring and backing ring was measured using a prototype backing ring based on the results of the FEM analysis, and a rotation test was conducted to investigate the effect of the prototype backing ring shape on reducing fretting wear [4].

2. Uniformity of pressure distribution

2.1 Target bearing

The uniformity of pressure distribution in the radial direction was investigated for double-row tapered roller bearings, which are widely used as axle bearings for railway vehicles. A schematic diagram of an axle bearing is shown in Fig. 1. The axle bearing consists of an outer ring with two raceways, two sets of an inner ring, cage and roller assemblies, two oil seals, a backing ring, and a seal wear ring. The inner rings and the backing ring are secured to the axle by an interference fit.

2.2 Consideration of backing ring shape by finite element method analysis

When an axle bearing is press-fitted into a journal of an axle, the inner diameter of the backing ring radially expands as it ascends the tapered part of the journal. As a result, the contact surface pressure between the inner ring and backing ring increases radially on the outside [3]. However, even if the inner diameter of the backing ring expands radially, there should be no problem if the deformation of the backing ring does not affect the contact with the inner ring. Thus, to suppress the deformation of the backing ring on the contact pressure and achieve uniform pressure distribution in the radial direction, we investigated the possibility of reducing the rigidity of the existing backing ring by making circumferential grooves onto its oil seal sliding surface. Since the groove depth, the groove distance

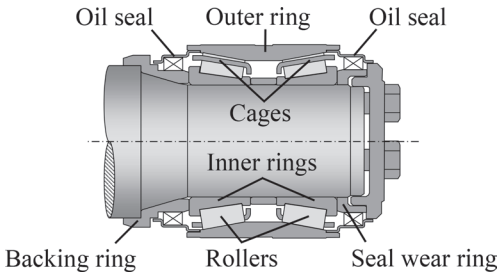

Fig. 1 Schematic diagram of a railway axle journal tapered roller bearing

from the contact surface, and the number of grooves affect the pressure distribution, the shape that achieves the most uniform pressure distribution was analyzed using the finite element method (FEM).

Figure 2 shows an example of the finite element model conducted. The analytical model consists of simplified blocks that simulate the shape of the inner ring, a backing ring, and an axle, each of which is composed of elastic hexahedral mesh (some of which are pentahedral mesh). The analytical model was constructed for 1/16 of the circumferential direction because each of these elements is axisymmetric around the z-axis. Symmetry constraint was applied to its cross-section. Additionally, the left side of the axle model was fully constrained. Young's modulus and Poisson's ratio were set to 210 GPa and 0.3, respectively, and friction among the contact surfaces was not considered. The load condition was a uniformly distributed load of 200 kN applied to the inner ring side face opposite the face in contact with the backing ring. The finite element code used in the analysis was NX Nastran V8.5.

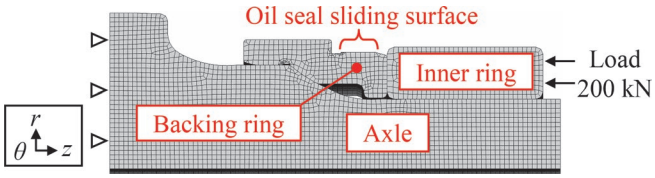

Fig. 2 Finite element model

First, one groove with a depth of 3 mm, 6 mm, or 9 mm was made on the oil seal sliding surface at 6 mm apart from the backing ring side face in contact with the inner ring to investigate the effect of the groove depth. Each groove width was fixed at 2 mm, assuming that the grooves would be made using a lathe. Figure 3 shows the contact pressure distribution between the inner ring and backing ring obtained by the FEM analysis, including the one without grooves. As the groove depth increases, the position of the maximum contact pressure moves toward the inner diameter side, and the area subjected to the contact pressure increases. Additionally, the grooving reduces the maximum contact pressure, with the greatest effect at a groove depth of 6 mm.

Secondly, we prepared a single groove that was provided at 6, 12, or 18 mm in the axial direction apart from the backing ring side face in contact with the inner ring to determine a suitable groove position. Each groove depth was fixed at 6 mm providing the lowest maximum contact pressure. Figure 4 shows the pressure distribution at the contact area between the inner ring and backing ring obtained from the FEM analysis, including the one without a groove. When the groove position is 6 mm apart from the contact surface, the peak position of the contact pressure moves toward the inner diameter side and the contact pressure-receiving area increases. On the other hand, when the groove position is 12 or 18 mm apart from the contact surface, the peak position of the contact pressure remains the same, but the contact pressure-receiving area increases.

Finally, to investigate the effect of the number of grooves, we prepared three cases of the grooves: one groove (at 6 mm in the axial direction apart from the backing ring side face), two grooves (at 6 and 12 mm), and three grooves (at 6, 12, and 18 mm), provided on the oil seal sliding surface. The groove depth was fixed at 6 mm, providing the lowest maximum contact pressure. Figure 5 shows the pressure distribution at the contact area between the inner ring and backing ring obtained from the FEM analysis, including the one without the grooves. As the number of grooves increases, the maximum contact pressure decreases, and the contact pressure-receiving area increases.

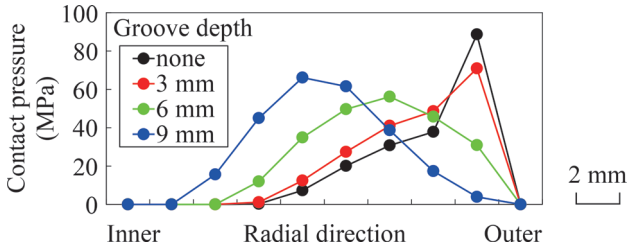

Fig. 3 Contact pressure distributions obtained by FEM analysis for groove depth

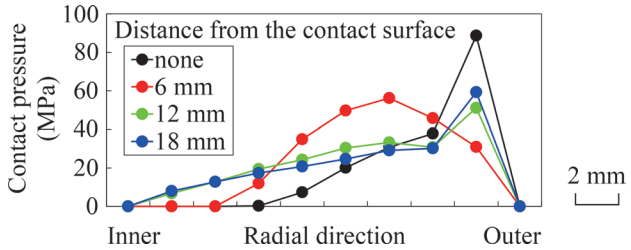

Fig. 4 Contact pressure distributions obtained by FEM analysis for distance from the contact surface

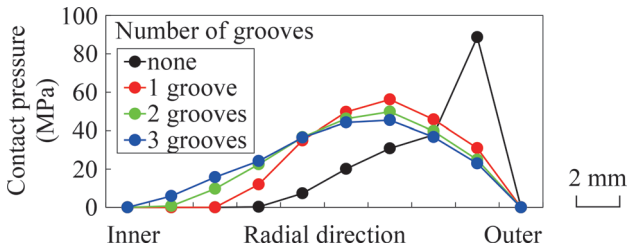

Fig. 5 Contact pressure distributions obtained by FEM analysis for number of grooves

The above results show that the condition with those three grooves provides the most uniform pressure distribution. Figure 6 shows the stress distribution in the axial direction under this condition.

2.3 Prototype of the backing ring

Figure 7 shows the appearance of a prototype backing ring. The prototype backing ring has three grooves with a 6 mm depth at three positions (6, 12, and 18 mm in the axial direction apart from the

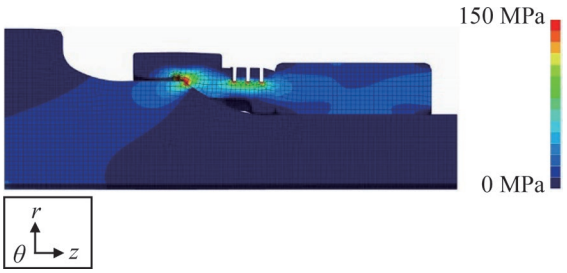

Fig. 6 Calculated stress in the axial direction using FEM analysis

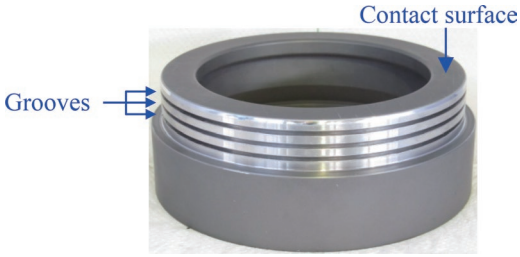

Fig. 7 Prototype backing ring

backing ring side face contacting with the inner ring) on the oil seal sliding surface.

2.4 Contact pressure distribution measurement

2.4.1 Measurement method and conditions

The contact pressure distribution between the inner ring and backing ring of the axle bearing was measured using the prototype backing ring shown in Fig. 7. The contact pressure distribution was measured using a thin-film pressure mapping system. For the pressure sensor specifications, refer to the previous paper [3].

The contact pressure distribution was measured by applying only radial load without rotating the shaft through an axle box equipped with an anti-vibration rubber while inserting a sensor between the inner ring and the prototype backing ring onto the shaft of an axle bearing performance test rig owned by the Railway Technical Research Institute. The radial load conditions were 0, 30, 50, and 70 kN. When the axle bearing was press-fitted hydraulically onto the shaft, the press-fit force was approximately 230 kN. Figures 8 and 9 show a set-up photograph of the pressure sensor and a schematic diagram of the measurement system with the axle box and anti-vibration rubber, respectively. The area where the bearing is subjected to the radial load is called the load side, and the load side in this measurement is the upper side in the vertical direction.

2.4.2 Measurement results

Figure 10 shows the measured contact pressure distribution of the prototype backing ring at a radial load of 0 kN. Because there is no sensing element at the position of the tab on the sensor sheet, no pressure is available at that position. The red-marked area is described in §3.4. The contact pressure between the inner ring and backing ring occurs over the whole circumference, but it is not uniformly distributed in the circumferential direction. If their contact surfaces were in even contact, a uniform contact pressure distribution in the circumferential direction could be obtained. In reality, however, the uneven distribution shown in Fig. 10 may have result-

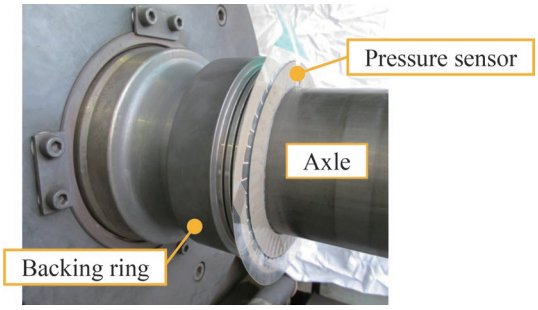

Fig. 8 Pressure sensor inserted between an inner ring and a backing ring through an axle

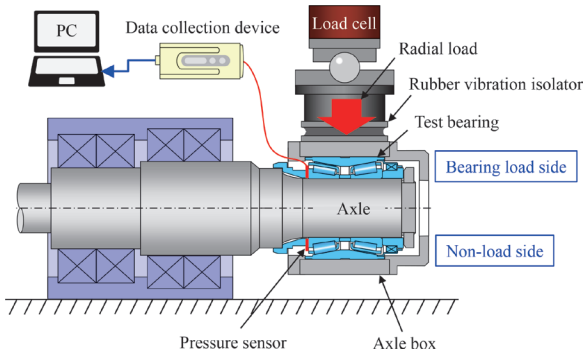

Fig. 9 Schematic diagram of the measurement system

ed due to the effects of the machining accuracy of each contact surface and the mounting condition during press fitting. For comparison, the pressure distribution of an existing backing ring without grooves on the oil seal sliding surface is shown in Fig. 11. Figure 10

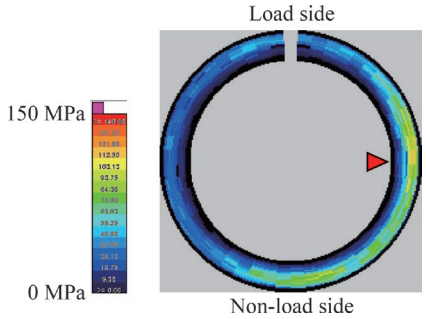

Fig. 10 Contact pressure distribution of the prototype backing ring for a radial load of 0 kN

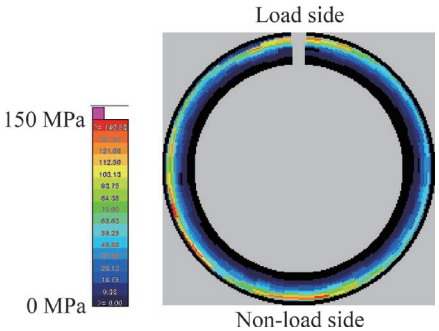

Fig. 11 Contact pressure distribution of an existing backing ring for a radial load of 0 kN

shows that the grooves on the oil seal sliding surface reduce the maximum contact pressure and increase the contact pressure near the middle of the radial direction. Thus, it can be said that the grooves have the effect of making more even pressure distribution in the radial direction.

To investigate the change in the contact pressure due to the deflection of the axle when a radial load is applied to the bearing, the amount of the change in the contact pressure was obtained by subtracting the contact pressure under no radial load shown in Fig. 10 from the contact pressure under applied radial load. This eliminates the influence of the contact condition between the inner ring and backing ring caused by press fitting the bearing onto the axle. Figure 12 shows the change in the contact pressure when radial loads were applied to the bearing. As the radial load increases, the contact pressure on the load side decreases; the contact pressure on the non-load side increases. The results show that the grooves on the oil seal sliding surface allowed the contact pressure to vary over a wide radial range and that more over the grooves reduced the maximum amplitude of the contact pressure.

The above results show that the amplitude of the contact pressure between them was reduced by providing circumferential grooves on the oil seal sliding surface of the backing ring to make more even radial pressure distribution on the contact surfaces.

2.4.3 Comparison with the analysis results

As described in §2.2, the FEM analysis showed that the radial pressure distribution between the contact surfaces approaches uniformity when grooves are made on the oil seal sliding surfaces of the backing ring. For the prototype backing ring made on the basis of the analysis results, the contact pressure distribution was measured. Here, we compare the analytical values obtained by FEM with the experimental values obtained by a thin-film pressure mapping system. The load condition for the above FEM analysis was calculated as an equally distributed load of 200 kN. However, the press-fit force was approximately 230 kN when the axle bearing was press-fitted hydraulically onto the shaft of the test rig. Thus, this value was used in the FEM analysis and recalculated.

Figure 13 shows the FEM analytical and experimental values of the pressure distribution in the case of a grooved backing ring. The experimental value is the pressure distribution in the radial direction obtained by averaging the contact pressure at each sensing element of the contact pressure distribution obtained by the no-load condition shown in Fig. 10 on the same circumference. The pressure distribution shows almost the same pattern between the FEM analytical and experimental values. Additionally, both the maximum values are nearly equal and are located slightly on the outer diameter side from the middle of the radial direction. The FEM analysis can be used to evaluate the pressure distribution owing to the change in the shape of the backing ring.

3. Bearing rotation test

3.1 Test bearing

To confirm the effect of the prototype backing ring shown in Fig. 7 on preventing fretting wear, we conducted a rotation test using a full-scale axle bearing. The bearing used for the rotation test was the same as that examined in Chapter 2. The inner ring was manufactured from carburized steel equivalent to JIS SNCM 420 steel and had a surface hardness of 58–62 HRC (equivalent to 653–746 HV). On the other hand, the backing ring was manufactured from normalized medium-carbon steel JIS S45C and had a surface hardness of 167–229 HBW (equivalent to 173–243 HV).

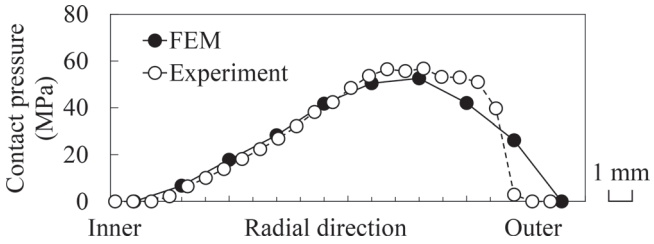

Fig. 13 Comparison of the result of the contact pressure by the FEM analysis with that by the experiment

3.2 Test condition

The rotation test was carried out using the test rig for axle bearing performance until the cumulative distance reached 600,000 km, which is the mileage at which axle bearings undergo inspections. The test method and condition were the same as those in the previous paper [3]. The surface temperature of the outer ring during the rotation test was about 51 K higher than the ambient temperature at the maximum and within the range of the predetermined regulation value (ambient temperature +70 K or less) specified in JRIS J 0455 [5].

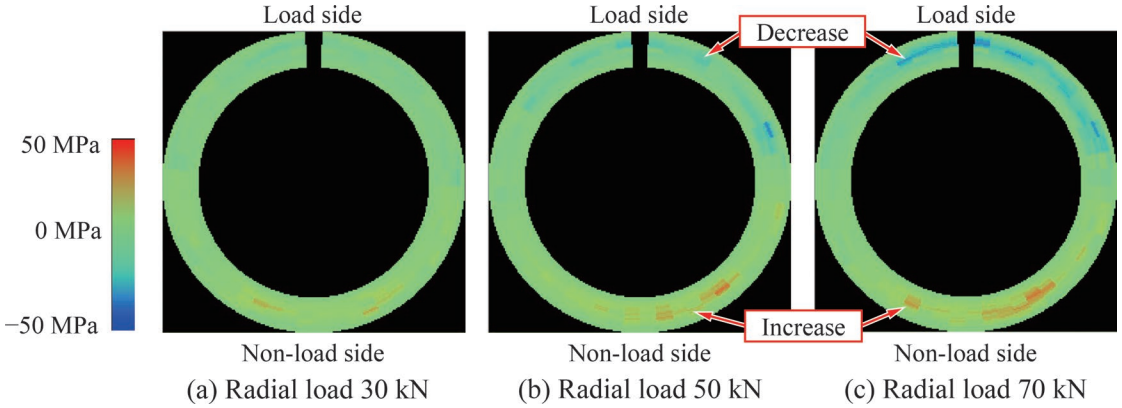

Fig. 12 Changes of the contact pressure distribution for each radial load in case of using the prototype backing ring

3.3 Test results

Figures 14 and 15 show the appearance and wear depth distribution of the prototype backing ring side face and the inboard inner ring back face after the rotation test, respectively. The wear depth distribution was measured in the circumferential direction using a two-dimensional laser displacement sensor. During the rotation test, the inner ring and the backing ring were in contact with each other at the coordinate phase of the circumferential direction without any relative rotation.

Wear is observed on both contact surfaces and the inner ring is covered with reddish-brown colored grease. Fretting wear particles are generally known to be reddish-brown iron (III) oxide (α-Fe_2O_3) [6]. When fretting occurs on the contact surfaces of the inner ring and the backing ring and fretting wear particles are mixed into the grease, the grease turns reddish brown. Accordingly, the wear on the backing ring side face and the inner ring back face was caused by fretting wear.

The wear depth distribution shows that the fretting wear of the inner ring back face occurs over the entire contact surface with a maximum wear depth of approximately 0.08 mm. On the other hand, the fretting wear of the backing ring side face occurs from the middle to the outer diameter in the radial direction with a maximum wear depth of approximately 0.08 mm.

Profile curve measurements were taken for the area having severe fretting wear (red marks) in Figs. 14 and 15. Figures 16 and 17 show microscope images and their profile curves of the prototype backing ring side face and the inner ring back face after the rotation

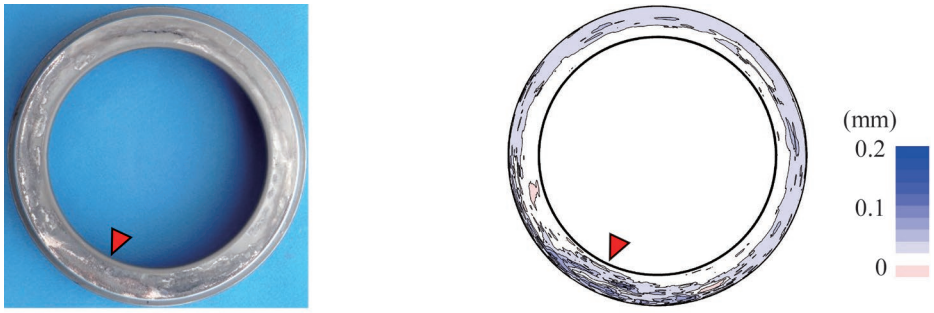

(a) Appearance (b) Wear depth distribution

Fig. 14 Prototype backing ring side face after the rotation test

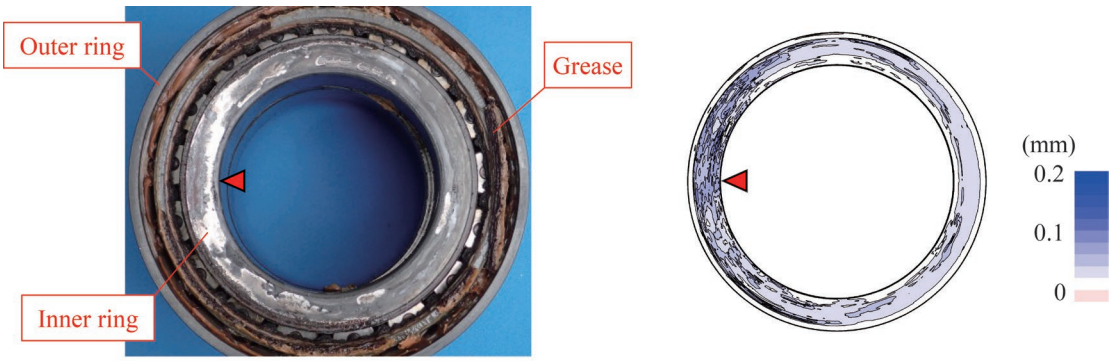

(a) Appearance (b) Wear depth distribution

Fig. 15 Inboard inner ring back face after the rotation test

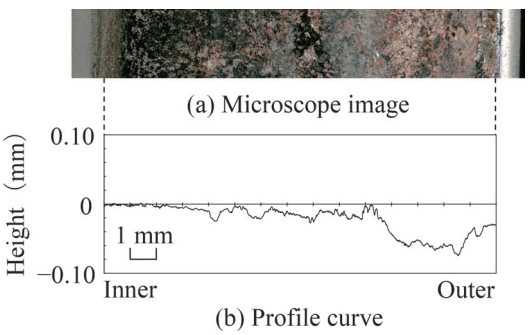

Fig. 16 Microscope image and corresponding profile curve of prototype backing ring side face after rotation test (enlarged image of section indicated with red mark in Fig. 14)

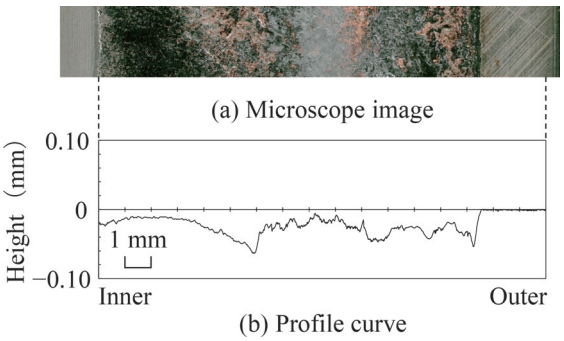

Fig. 17 Microscope image and corresponding profile curve of inboard inner ring back face after rotation test (enlarged image of section indicated with red mark in Fig. 15)

test, respectively. The fretting wear on the backing ring side face shown in Fig. 16 is noticeable in the vicinity of its outer circumference, and the maximum wear depth is approximately 0.07 mm. Additionally, the wear tends to be more marked on the outer side in the radial direction at all circumferential areas, which is almost consistent with the wear depth distribution shown in Fig. 14(b). On the other hand, the fretting wear on the inner ring back face shown in Fig. 17 is almost uniform in the radial direction with a maximum depth wear of approximately 0.06 mm.

3.4 Relation between fretting wear and contact pressure

As shown in §3.3, the fretting wear on the inner ring back face and the prototype backing ring side face was not uniform in the circumferential direction. This may be related to the fact that the contact pressure was not uniform in the circumferential direction when the axle bearing was press-fitted onto the axle, as shown in Fig. 10. Accordingly, we checked the positional relationship between the wear depth distribution and the contact pressure distribution and found that they coincided. Furthermore, the most significant wear area on the profile curve of the backing ring side face (red arrow in Fig. 14) coincided with the high contact pressure area on the radial direction of the pressure distribution (red arrow in Fig. 10), as shown in Fig. 18. Thus, the degree of the fretting wear on the inner ring and the backing ring in the axle bearing is affected by the magnitude of the contact pressure between them that becomes uneven when the axle bearing has been press-fitted onto the axle.

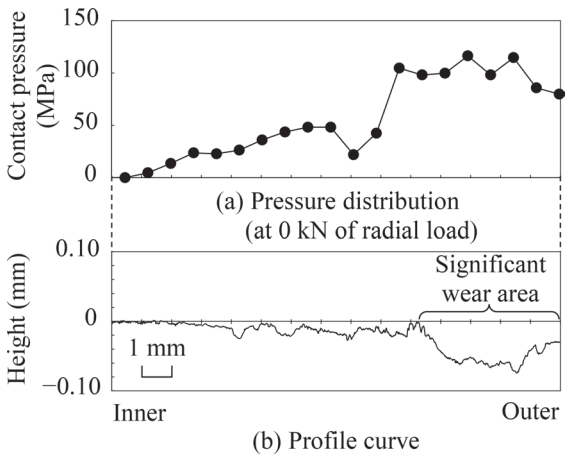

Fig. 18 Measured pressure distribution for a radial load of 0 kN and profile curve of the prototype backing ring after the rotation test

4. Effect of reducing fretting wear by equalizing pressure distribution

In our previous paper [3], we confirmed that the fretting wear area of the backing ring side face coincides with the place where the amplitude of the contact pressure is high. When the pressure distribution in the radial direction between the inner ring and backing ring is made even, the fretting wear on the contact surfaces can be reduced. As described in Chapter 2, when the pressure distribution in the radial direction between them was made uniform by adding circumferential grooves to the oil seal sliding surface of the backing ring, the maximum contact pressure and the maximum amplitude of the contact pressure were reduced accordingly. Thus, the wear depth distribution was measured on the existing backing ring side face without grooves after the rotation test, as shown in the previous paper [3], and compared with the results obtained in this paper.

Figure 19a and 19b show the wear depth distributions of the backing ring side face without grooves on the oil seal sliding surface and with grooves (same as Fig. 14b), respectively. Note that there is an unmeasured area in Fig. 19a, which was cut off for the material evaluation and the wear condition of which was reported in the previous paper [3]. Although the fretting wear of the backing ring is generated all over the contact surface regardless of the grooves, a comparison of the two shows that the wear on the grooved backing ring side face is less.

Additionally, to investigate the amount of the fretting wear particles in the grease with and without grooves on the backing ring, the grease adhered to the inside of the cage bars and the roller large end faces was collected from the inboard inner ring of the tested bearing after the rotation test. Their iron content was determined using a scanning X-ray fluorescence spectrometer. Table 1 gives the results. The grooves on the backing ring reduced the iron content of the grease collected from the inside of the cage bars and the large end faces of the rollers.

Table 1 Iron content of the grease collected after the bearing rotation test

	Inside of cage bars	Roller large end faces
With grooves	0.14 mass%	0.16 mass%
Without grooves	0.21 mass%	2.88 mass%

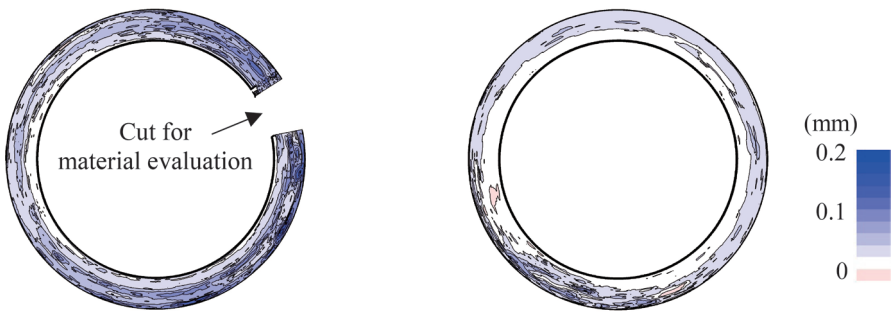

Fig. 19 Comparison between the amplitude of the contact pressure in the radial direction for the presence of grooves and for the absence of grooves

The above results indicate that the grooves on the oil seal sliding surface of the backing ring reduce the fretting wear between the inner ring and backing ring by making the pressure distribution in the radial direction closer to even.

5. Conclusions

To prevent fretting wear that occurs between the inner rings and backing rings of axle bearings, we proposed cutting circumferential grooves on the oil seal sliding surface of the backing ring to bring the radial pressure distribution between them closer to even. To confirm the effect of the grooved backing ring, we analyzed and measured the pressure distribution and conducted a rotation test using an actual bearing. The main results obtained are shown below.

1. We investigated the shape of the backing ring to make the contact pressure distribution between the inner ring and backing ring as even as possible using FEM analyses. When a circumferential groove is made on the oil seal sliding surface of the backing ring, the maximum contact pressure between the inner ring and backing ring is reduced, and the pressure distribution in the radial direction becomes more even.
2. A prototype backing ring was fabricated under the conditions that produced the most even pressure distribution among those studied in the FEM analysis. The contact pressure distribution between the inner ring and backing ring was measured using it, and the measured distribution agreed with the result of the FEM analysis.
3. The area of significant fretting wear in the backing ring with grooves on the oil seal sliding surface coincides with the area where the amplitude of the contact pressure is high, as in the case of existing backing rings without grooves.
4. The bearing rotation test result showed that the fretting wear on the contact surface of the prototype backing ring with grooves was less than that of the existing backing ring without grooves. Besides, the iron content of the grease in the bearing with the grooved backing ring was smaller than that with the existing backing ring.

From the above, we confirm that circumferential grooves on the oil seal sliding surface of backing rings generate more even contact pressure distributions in the radial direction between inner rings and backing rings and have the effect of reducing fretting wear that occurs on inner rings and backing rings of axle bearings.

References

[1] Takano, K. and Asai, H., "Axle bearing equipment," Japan Patent JP3529691B2, 2004 (in Japanese).
[2] Oka, R., "High speed and long life technology for railway axle journal bearings," *Journal of Japanese Society of Tribologists*, Vol. 58, No. 7, pp. 479-484, 2013 (in Japanese).
[3] Okamura, Y., Fukagai, S. et al., "Effect of the contact pressure on the fretting of railway axle journal bearings," *Transactions of the JSME*, Vol. 82, No. 834, DOI: 10.1299/transjsme.15-00523, 2016 (in Japanese).
[4] Okamura, Y., Suzuki, D. et al., "Reduction of fretting wear in contact surfaces of inner ring and backing ring of railway axle journal bearings," *Transactions of the JSME*, Vol. 84, No. 859, DOI: 10.1299/transjsme.17-00324, 2018 (in Japanese).
[5] *Rolling stock—Performance tests for axle journal rolling bearings*, JRIS J 0455, 2009 (in Japanese).
[6] Waterhouse, R. B., *Fretting Corrosion,* Pergamon Press Ltd., Headington Hill Hall, Oxford, England, pp. 83-88, 1972.

Authors

Yoshiaki OKAMURA, Ph.D.
Senior Chief Researcher, Head of Lubricating Materials Laboratory, Materials Technology Division
Research Areas: Tribology, Roller Bearing, Metallic Material

Daisuke SUZUKI
Assistant Senior Researcher, Lubricating Materials Laboratory, Materials Technology Division
Research Areas: Tribology, Roller Bearing, Mechanical Engineering

Shinya FUKAGAI, Ph.D.
Senior Researcher, Frictional Materials Laboratory, Materials Technology Division
Research Areas: Friction Management between the Wheel and Rail, Tribology

Ken TAKAHASHI, Ph.D.
Senior Researcher, Lubricating Materials Laboratory, Materials Technology Division
Research Areas: Tribology, Roller Bearing, Mechanical Engineering

Takafumi NAGATOMO, Ph.D.
Senior Chief Researcher, Head of Lubricating Materials Laboratory, Materials Technology Division (Former)
Research Areas: Tribology, Roller Bearing, Metallic Material

Autonomous Damage Detection System for Damaged Axle Bearings of Railway Car Bogies

Shogo MAMADA **Tatsuya OHTA**
Vibration-Isolating Materials Laboratory, Materials Technology Division

Yoshiaki OKAMURA
Lubricating Materials Laboratory, Materials Technology Division

Axle bearings of railway car bogies are important parts that support the running of the cars. It is desirable to detect damage to axle bearings at an early state. Therefore, an autonomous damage detection system (ADDS) was developed that does not require a power supply nor wiring and notifies axle bearing damage to the vehicle. The ADDS utilized an anti-vibration rubber with a built-in piezoelectric element and a wireless transmitter; which was installed on the axle box. The damage detection performance of the ADDS was evaluated using a test machine. In the case of a damaged bearing, the power generated by the piezoelectric element built-in the rubber could drive the transmitter, and the damage could be notified.

***Key words*:** *axle bearing, autonomous damage detection system, anti-vibration rubber, piezoelectric element, transmitter*

1. Introduction

Axle bearings in railway bogies are critical for the smooth rotation of axles while supporting car bodies. Damage to these axle bearings may cause running difficulty. Therefore, damage to axle bearings must be detected as soon as possible [1, 2].

Currently, temperature is used to monitor axle bearings. On some conventional lines, irreversible temperature seals are used, which change color at certain temperatures [1]. On Shinkansen trains, shaft temperature detection sensors are attached to axle boxes that house axle bearings and will disconnect internal cables at high temperatures [2]. However, when the temperature of axle boxes rises to a level that is detected by these sensors, it is assumed that the damage is advanced.

The authors have been studying a method for detecting abnormal vibrations caused by damaged axle bearings using piezoelectric elements incorporated in the axle spring rubbers installed on the axle boxes, as shown in Fig. 1. Piezoelectric elements generate electrical signals in response to applied vibration. The results of this study showed that by analyzing the electrical signals generated from the piezoelectric elements, bearing damage could be detected before the temperature of the axle boxes rose [3]. On the other hand, in this method, it is necessary to wire a cable from the piezoelectric element built into the axle spring vibration isolator to the car and analyze the electrical signals obtained, and implementing this on a real vehicle is complicated. One solution is to use wireless devices which can send a notification in case of detected damage. However it is difficult to secure power supplies to drive the transmitters of wireless devices on axle boxes.

Therefore, as a technology to secure the power to drive the transmitter, we examined the use of energy harvesting, which stores and utilizes the minute electric power generated by piezoelectric elements [4]. It was assumed that if this technology could be utilized to drive a transmitter using electric power generated from the piezoelectric element built into the axle spring vibration isolator due to abnormal vibration caused by axle bearing damage, the system would be an autonomous damage detection system (ADDS) that could autonomously detect and notify the user of damage. This paper presents a summary of the fabricated ADDS and the results of evaluating its basic and damage detection performance.

2. Summary of ADDS

The ADDS consists of a damage detection rubber (DDR) which is an axle spring vibration isolator for the system and a receiver for the wireless device.

2.1 DDR

A schematic diagram of the DDR is shown in Fig. 2. As shown in Fig. 2, the DDR has three components: a power generation component, a capacitor component, and a transmission component. Each component can contain the components of each component by providing grooves in the rubber.

2.1.1 Power generation component

The power generation components contain a power generation module that uses lead zirconate titanate (PZT) as a piezoelectric element. There are two power generation components, each of which contains one power generation module. The power generation module is made of two stacked disks of PZT with a diameter of 50 mm and a thickness of 2 mm. When stacking them, conductive rubber of 50 mm in diameter and 0.5 mm in thickness was interposed between

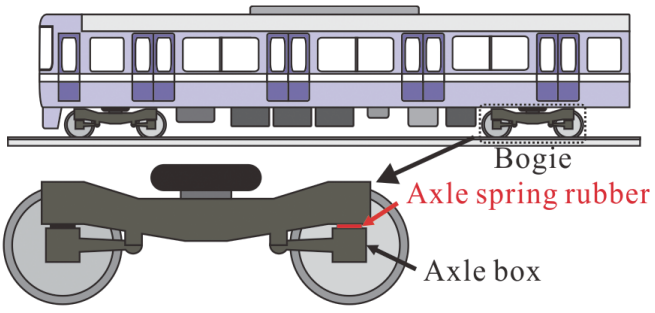

Fig. 1 Installation location of axle spring rubber

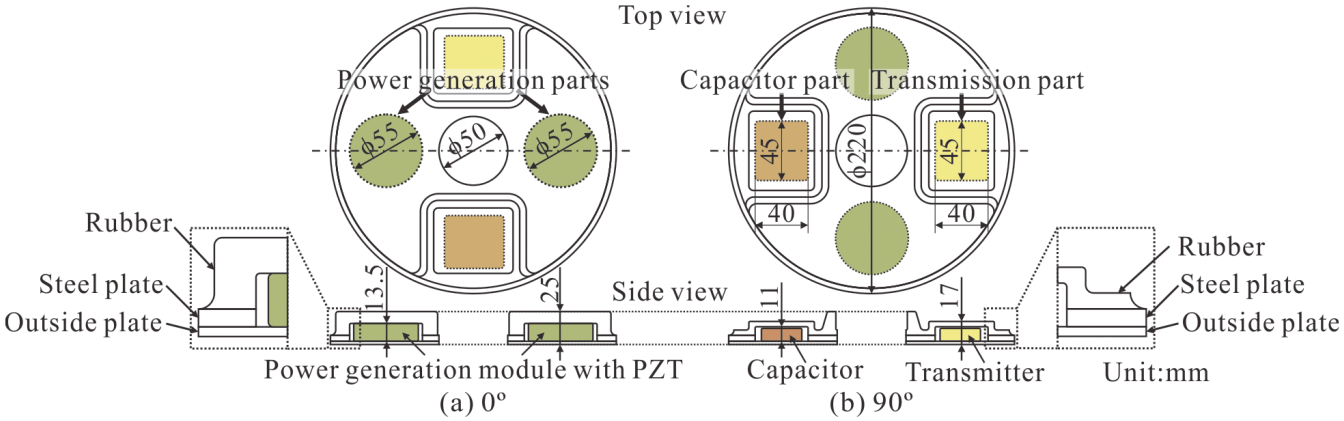

Fig. 2 Schematic diagram of the DDR

the PZT and the electrodes. This is because past findings have shown that the power generation performance of the power generation module improves when conductive rubber is interposed [5]. The thickness of the power generation components s is thicker than that of the capacitor and transmission comoponent to ensure that the load is applied to the stored power generation module.

2.1.2 Storage component

The power storage component contains a rectifier circuit using a diode to rectify the power generated by the power generation module, a capacitor to store the rectified power, and a switching regulator circuit to supply power from the capacitor to the transmitter when capacitor voltage reaches 5 V. The rectifier circuit has two systems to rectify the power generated by the two generation modules individually, and the power generated by the individual generation modules can be added together and stored in the capacitor. The capacitance of the capacitor was set to 220 μF in consideration of the minimum power required to drive the transmitter.

2.1.3 Transmission component

The transmitter of the radio equipment was housed in the transmitting component. Considering the size and power consumption, a specified low-power radio station with a frequency in a 315 MHz band and a transmission output of 0.3 mW was selected for the transmitter. The thickness of the storage and transmitter component s was made thinner than that of the generator component in order to prevent damage to the stored components due to direct loading on these components.

2.2 Receiver for wireless devices

The receiver of the wireless devices was selected to be paired with the transmitter. When the receiver receives a radio signal from the transmitter, the LED turns on for about 1 second and then automatically turns off, and the receiver enters a standby state until the next radio signal is received.

3. Basic Performance of ADDS

3.1 Static spring constant of DDR

The DDR is intended to be used in place of the current axle-spring rubber. Therefore, the static spring constant, which indicates the anti-vibration performance as axle-spring bearing rubber, should be the same as that of the current axle-spring rubber.

Therefore, a static loading test was conducted with the two power generation modules in the fabricated DDR, and the spring constants were measured. As a result, it was found that the spring constant of the DDR was within the range of ±10% of the spring constant of the current axle-spring rubber. Even when the maximum load expected to be applied when the rubber is installed on a bogie, no load is directly applied to the storage and transmission components.

3.2 Power generation performance of DDR

To evaluate the power generation performance of the DDR, the rubber was installed in a dynamic vibration machine and subjected to a vibration test in which a sinusoidal load was applied in the direction of its thickness. Figure 3 shows the appearance of the vibration test.

The conditions of the vibration test were as follows: the average load was 50 kN, the amplitude load was 1 kN, 5 kN, and 10 kN, and the vibration frequency was 0.1 Hz, 1 Hz, and 10 Hz, assuming the load applied when the rubber was installed on a bogie. During the vibration test, the capacitor voltage was measured to evaluate the power generation performance of the DDR.

Figure 4 shows examples of the relationship between excitation time and capacitor voltage in the vibration test. Figure 4(a) shows

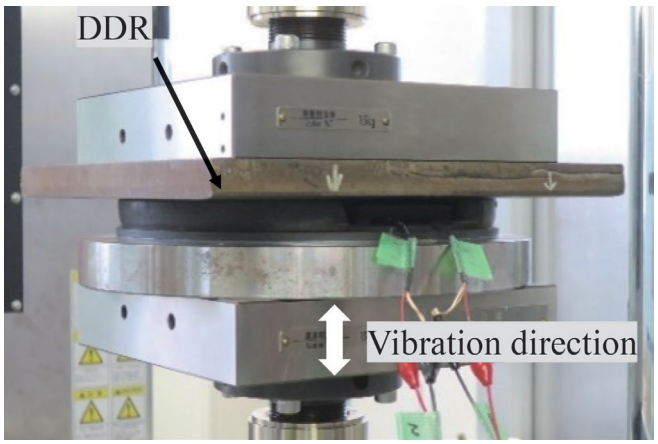

Fig. 3 Appearance of the vibration test

the results for excitation frequencies of 0.1 Hz, 1 Hz, and 10 Hz at an amplitude load of 1 kN, and Fig. 4(b) shows the results for amplitude loads of 1 kN, 5 kN, and 10 kN at a vibration frequency of 1 Hz.

Figure 4(a) shows that for the same amplitude load, the capacitor voltage at the same excitation time peaked at 10 Hz, followed by 1 Hz and 0.1 Hz. Figure 4(b) shows that for the same excitation frequency, the capacitor voltage peaked at 10 kN, followed by 5 kN and 1 kN. These results indicate that the power generation performance of DDR improves with increasing excitation frequency and amplitude load. As shown in Fig. 4(b), the capacitor voltage dropped sharply to about 3.5 V after reaching 5 V at amplitude loads of 5 kN and 10 kN. This is because the switching regulator in the storage component operated when the capacitor voltage reached 5 V, and power was supplied to the transmitter. At this time, it was confirmed that radio waves were transmitted to the receiver. After the amount of electric power decreased to about 3.5 V, it increased again until it reached 5 V, and

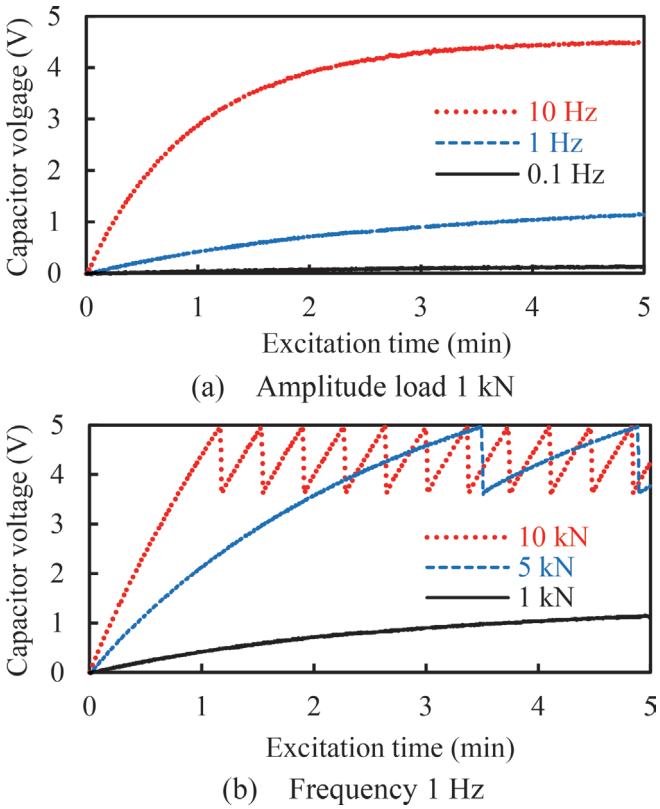

Fig. 4 Relationship between excitation time and capacitor voltage

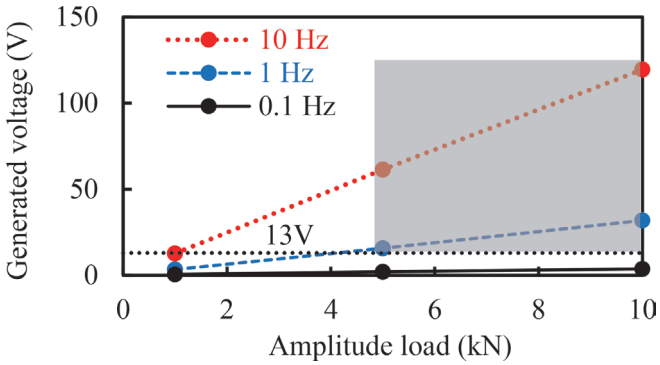

Fig. 5 Generated voltage in vibration tests

electric power was supplied to the transmitter again and radio waves were transmitted.

Next, the conditions for driving the transmitter were examined. When using a piezoelectric element to store electricity in a capacitor, the higher the input voltage, the more the stored electricity [6]. Therefore, the voltage generated by the generation module was measured during a vibration test, and the difference between the maximum and minimum values was determined as the generated voltage. The relationship between amplitude load and generated voltage is shown in Fig. 5. The generated voltage in Fig. 5 indicates the value of the smaller of the two generation modules. The shading in Fig. 5 indicates the conditions under which the transmitter was driven, and the radio was transmitting.

Figure 5 shows that the generated voltage increases in proportion to the amplitude load and with increasing excitation frequency. This trend is similar to that of the capacitor voltage. The reason why the generated voltage of the generation module increased with increasing amplitude load and vibration frequency is due to the characteristics of PZT, since the generated voltage of PZT itself has shown a similar trend in past studies [6]. In this vibration test, it was found that when the generated voltage from either of the generation modules reached approximately 13 V or higher, the capacitor voltage got 5 V or higher, and the transmitter was able to transmit a radio wave.

4. Damage Detection Performance of ADDS

The damage detection performance of the ADDS was evaluated through evaluation tests conducted by installing an artificially damaged bearing in an axle bearing endurance test machine owned by the RTRI. Figure 6 shows the test conditions.

4.1 Damaged bearings

The damaged bearing used in the test had an indentation artificially pressed on the surface of the outer ring, and then flaking damage was made starting from the indentation. Flaking of outer rings is one of the types of damage that can occur in bearings, and if flaking develops, the flakes can get mixed in with the grease and cause lubrication problems, leading to seizure.

The bearing was mounted on the test machine after the indentation was made. A load of approximately 50 kN in the vertical direction was exerted on the DDR while the main shaft rotated at a speed equivalent to 300 km/h and a horizontal load of 14.7 kN was applied repeatedly for 5 seconds at 5-second intervals to generate and develop flaking in the damaged bearing from the indentation. Figure 7 shows the occurrence and propagation of flaking. As shown in Fig. 7, clear flaking occurred after cumulative rotation equivalent to running of 100,000 km and developed as the running distance increased. It was difficult to detect flaking solely through temperature of the shaft box even after cumulative rotations equivalent to a run of 200,000 km.

4.2 Damage detection performance evaluation method

The damage detection performance of the AADS was evaluated by measuring the capacitor voltage in the DDR and generated voltage by the power generation module. Measurements were taken before (0 km) and then every 50,000 km running after the indentation was made artificially. During the measurements, the main shaft rotated at a speed equivalent to 30 km/h~300 km/h with a load of

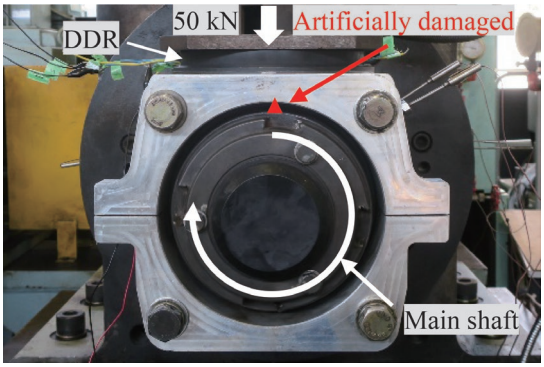

Fig. 6 Condition of the evaluation test of damage detection performance

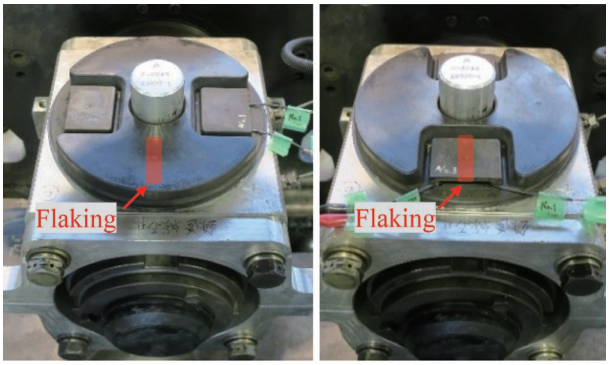

(a) Pattern A (b) Pattern B

Fig. 8 Arrangement of DDR for damage detection in the test

approximately 50 kN applied in the vertical direction. The location of the flaking in the evaluation was set at the center of the loading zone where the load was applied most, as shown in Fig. 6. As shown in Fig. 8, two arrangements of DDR for damage detection were used: the arrangement in which the power generation component is directly above the flaking (Pattern A), and the arrangement in which the storage and transmission components are directly above the flaking (Pattern B).

4.3 Damage Detection Performance with ADDS

The maximum terminal-to-terminal voltage at 5 minutes after measurement is shown in Fig. 9. Figure 9 (a) and (b) show the results for arrangement A and B, respectively. When the capacitor voltage did not reach 5 V in 5 minutes, capacitor voltage hardly increased thereafter, and the transmitter was not driven.

As shown in Fig. 9, the capacitor voltage increased with increasing running distance for both patten A and B. This can be considered as follows: flaking develops as the travel distance increases, the axle box vibration increases with the development of flaking, resulting in an increase in the load applied to the power generation module in the DDR for damage detection. The vibration acceleration of the axle box, measured separately in this test, increased with increasing running distance. On the other hand, when the maximum value of the capacitor voltage under the same test conditions was compared between pattern A and B, pattern A was larger, indicating a higher power generation performance. Note that in pattern A, there is a possibility of detection of the flaking when the bearing rotates at the equivalent speed of 70 km/h or more after the cumulative rotation has reached the equivalent travel of 50,000 km~100,000 km after the flaking occurred.

4.4 Wireless transmitter driving conditions

As shown in Fig. 9, the maximum values of the capacitor voltage were different between pattern A and B. To understand this factor, as in the shaking test, the conditions required for the capacitor voltage to reach 5 V and for the transmitter to be driven were examined using the measured results of the capacitor voltage and the generated voltage of the power generation module.

As examples of the results of capacitor voltage and generated voltage immediately after the start of measurement in patterns A and B, the results for a rotational speed of 110 km/h after rotation equivalent to 100,000 km of driving are shown in Fig. 10. In Fig. 10, (a) is the capacitor voltage and (b) is the generated voltage.

As shown in Fig. 10, both the capacitor voltage and the generated voltage are larger in pattern A than in pattern B. Therefore, to evaluate the difference in power generation performance between pattern A and pattern B, the amount of electric energy was calculated from the results of the capacitor voltage at 1 second after the start of measurement using the following equation.

$$W = \frac{1}{2} C V_{1S}^2 \quad (1)$$

where W is the electric energy (J), C is the capacitance (C/V), and V_{1s} is the capacitor voltage (V) 1 second after the start of measurement.

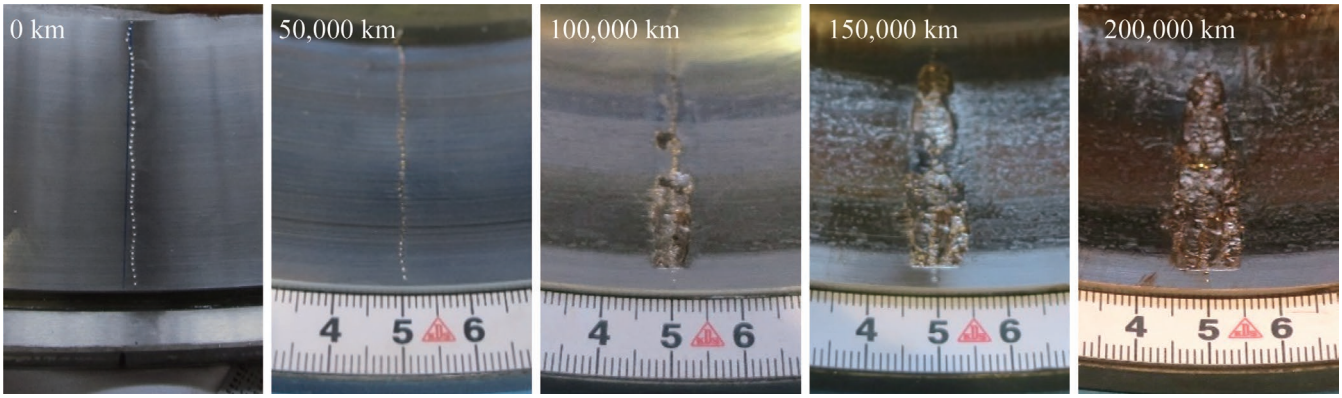

Fig. 7 Occurrence and progress of flaking of damaged bearings used in damage detection performance evaluation tests

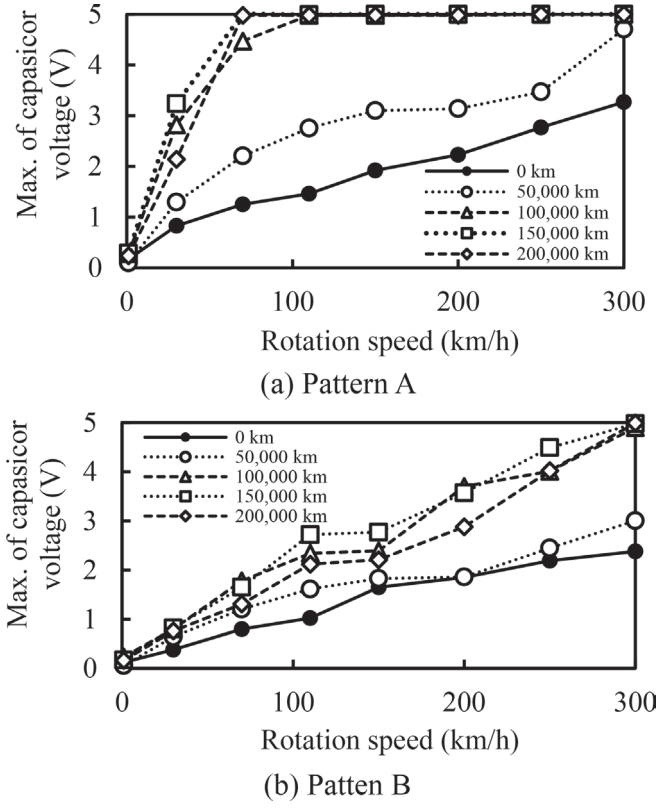

Fig. 9 Max. of capacitor voltage

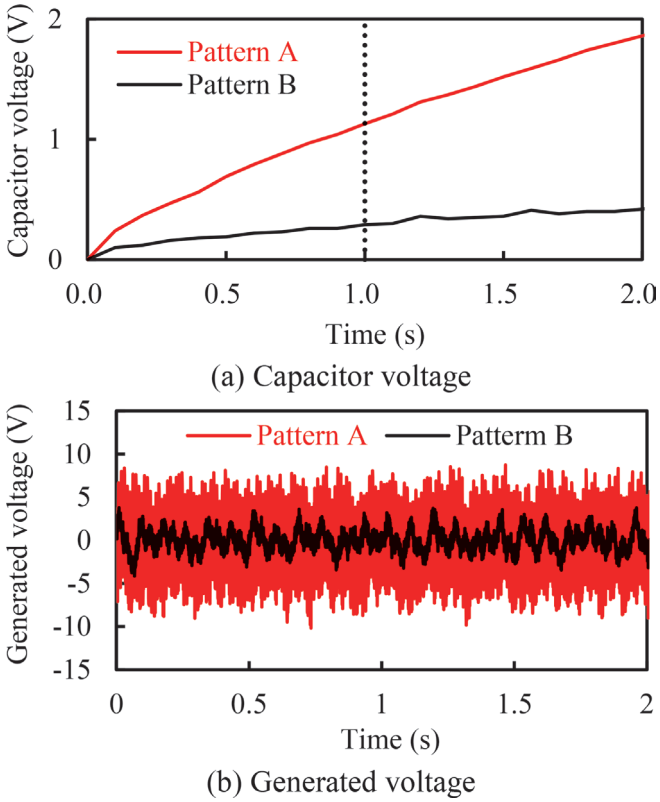

Fig. 10 Example of measurement results of capacitor voltage and generated voltage (after 100,000 km, rotation speed 110 km/h)

The amount of electric energy W calculated from the results in Fig. 10(a) was 0.11 mJ for pattern A and 0.01 mJ for pattern B. From these results, it was assumed that the higher the amount of electric energy, the higher the capacitor voltage. Therefore, the relationship between the amount of electric energy and the capacitor voltage for all test conditions was determined. The results are shown in Fig. 11.

Figure 11 shows that the maximum capacitor voltages of both patterns A and B tend to increase as the electric energy increases. On the other hand, comparing the capacitor voltages of patterns A and B at the same electric energy level, the capacitor voltage of pattern B is generally lower. In addition, the condition for the electric energy to reach the capacitor voltage of 5 V may be less than 0.05 mJ in the case of pattern A, but may not reach even at 0.05 mJ or more in the case of pattern B. These results indicate that the magnitude of the electric energy differs depending on the arrangement and that factors other than the electric energy may affect the condition for the terminal-to-terminal voltage to reach 5 V.

Therefore, the influence of the generated voltage from power generation modules was examined in the same way as in the case of the vibration test. As an example, in the case of the results shown in Fig. 10(b), the generated voltage is about 18.9 V for pattern A and about 7.9 V for pattern B. The relationship between the generated voltage and the maximum value of the capacitor voltage is shown in Fig.12. However, as in the case of the vibration test, the figure shows the generated voltage of the smaller of the two power generation modules.

Figure 12 shows that the capacitor voltage increases as the generated voltage increases for both patterns A and B. The capacitor voltage reaches 5 V when the generated voltage is approximately 14 V or higher. This value is almost equivalent to the result of approximately 13V obtained in the vibration test.

The above results show that the magnitude of the generated voltage from the power generation module has a significant effect on driving the transmitter. One of factors that makes the generated voltage of pattern A higher than that of pattern B and makes it easier to drive the transmitter is that in the case of pattern A, the power generation components of the DDR are located at the center of the load zone, which is directly above the flaking, and the power generation module is easily subjected to the load.

5. Proposal of damage detection method during actual driving

When DDRs are installed on an actual bogie, radio signals may be transmitted even during normal running because the DDRs are subjected to various vibrations that occur during running. On the other hand, if damage occurs to the axle bearings, the frequency of radio transmission is likely to increase. Therefore, as shown in Fig. 13, it is thought that damage can be detected by sensing the difference in radio transmission intervals between normal running and running when damage occurs.

Furthermore, when ADDSs are installed in actual vehicles, receivers are assumed to be installed in vehicle bodies, so it is necessary to select their installation location based on reception sensitivity and other factors.

6. Conclusion

As an ADDS, a DDR with a built-in piezoelectric element and a transmitter for a wireless device was built, and its basic performance and damage detection performance were evaluated.

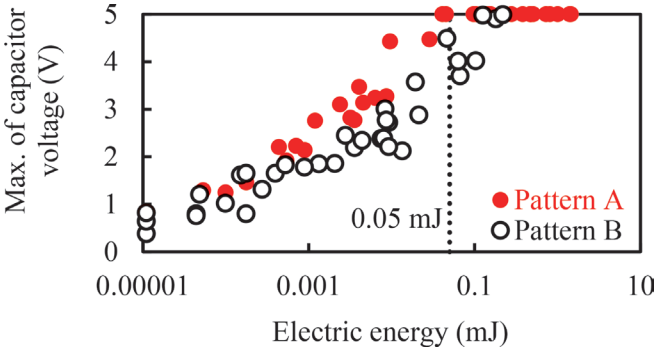

Fig. 11 Relationship between max. of capacitor voltage and electric energy

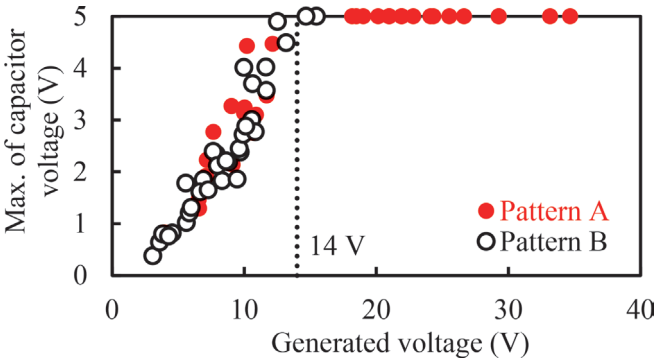

Fig. 12 Relationship between max. of capacitor voltage and generated voltage

As a result, it was found that, as basic performance, the higher the amplitude and frequency of the load applied to the DDR, the higher the piezoelectric efficiency. As for damage detection performance, it was found that when damage occurs in the bearing, the piezoelectric element in the DDR can generate enough electricity to drive the transmitter of the wireless device and signal the occurrence of damage, if the bearing rotates at an equivalent vehicle speed of 70 km/h or more after having experienced a cumulative run of 50,000 km to 100,000 km from the damage. Furthermore, it was found that to drive the transmitter, a voltage of 13 V~14 V or higher must be generated from a power generation module using a piezoelectric element housed in the DDR.

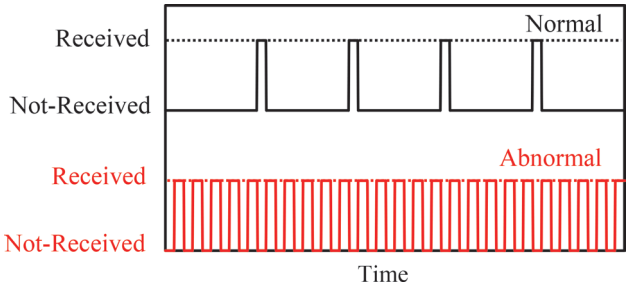

Fig. 13 Image of damage detection in actual driving

References

[1] Chiba, S., Ishi, K., "Application and improvement of reliability of the TC type of the temperature detector system," *JR EAST Technical Review*, No. 29, p. 31, 2009 (in Japanese).

[2] Uemura, Y., Nakata, K., Oba, T., Hirano, M., "Development of the temperature detector of the axle box of bogie of the shinkansen," *JREA*, Vol. 56, No. 5, pp. 377714-377717, 2013 (in Japanese).

[3] Nogimura, R., Mamada, S., Okamura, Y., Yamanaka, S., Suzuki, Y., "Development on detection technique of bearing damages by sensor rubber isolator," *J-Rail2017 Proceeding*, *S2-7-5*, 2017 (in Japanese).

[4] Yoshida, Y., Kobayashi, Y., Uchida, T., "Development of the monitoring system that operates with the power generated from the bridge vibration," *Journal of Japan Society of Civil Engineers, SER. AI Structural Engineering & Earthquake Engineering*, Vol. 70, No. 2, pp. 282-294, 2014 (in Japanese).

[5] Mamada, S., Takenaka, H., Ohta, T., Takahashi, K., Suzuki, D., "Damage detection of bearing in gear case by using piezoelectric element incorporated in hanging rubber for gear case of rolling stock (Evaluation of defection performance by bench test)," *Transactions of the JSME*, Vol. 86, No. 890, 2020 (in Japanese).

[6] Fujimoto, S., Imai, T., Ichiki, M., "Study on method of vibration power generation using piezoelectric element (3rd report, examination of optimal layer number of laminated piezoelectric elements)," *journal of Japan Society for Design Engineering*, Vol. 52, No. 9, pp. 567-582, 2017 (in Japanese).

Authors

Shogo MAMADA, Ph.D. in Eng.
Senior Chief Researcher, Head of Vibration-Isolating Materials Laboratory, Materials Technology Division
Research Areas: Isolating Rubber, Functional Rubber, Composite Materials

Tatsuya OHTA
Assistant Senior Researcher, Vibration-Isolating Materials Laboratory, Materials Technology Division
Research Areas: Isolating Rubber, Composite Materials, Environment Materials

Yoshiaki OKAMURA, Ph.D. in Eng.
Senior Researcher, Lubricating Materials Laboratory, Materials Technology Division
Research Areas: Tribology, Roller Bearing, Metallic Material

Influence of a Decarburized Layer on the Formation of Microcracks in Railway Rails: On-site Investigation

Yoshikazu KANEMATSU **Naotaka UEHIGASHI**
Frictional Materials Laboratory, Materials Technology Division

Motohide MATSUI
Materials Technology Division

This study aims to understand the effect of decarburization on microcrack formation on rails by an on-site (laying) test. Test pieces with and without decarburization were compared under the same test conditions. The results show that decarburization affects the formation of microcracks and plastic flow. Furthermore, we investigated the decarburization effect on microcrack formation using test pieces taken from actual tracks. A comparison of test pieces with and without a decarburized layer showed that the crack density of rails on the unground was 2.7-5.7 times higher than that of rails ground at a cumulative tonnage of 23 MGT.

***Key words*:** *rail, decarburization, on-site (laying) test, microcrack*

Reprinted from Wear, Vol 504, Yoshikazu Kanematsu, Naotaka Uehigashi, Motohide Matsui, Shoji Noguchi, Influence of a decarburized layer on the formation of microcracks in railway rails: On-site investigation and twin-disc study, (2022), with permission from Elsevier

1. Introduction

One problem that occurs when using rails is squats, which are a type of rolling contact fatigue (RCF). It is believed that squats are caused by the formation of microcracks on a rail surface due to repeated wheel contact, and that some of these cracks can grow in size [1-5]. If squat cracks continue to grow, a rail may break. Therefore, railway operators need to inspect rails and identify squat formation, which accounts for part of the cost of railway maintenance. In addition, railheads are often ground to prevent squats [6-9].

During rail manufacturing processes, rail material is heated in the atmosphere. At high temperatures, oxygen in the air reacts with carbon on the surfaces of steel, and carbon is eliminated as a gas: this process is called decarburization. Decarburization decreases the carbon concentration beneath the surface of steel. The portion of the surface where decarburization occurs forms a decarburized layer. It is well known that this decarburized layer reduces mechanical properties and hardness. The thickness of a decarburized layer depends on many factors, including the atmosphere in the heating furnace [10, 11].

A study on the effect of a decarburized layer on RCF was previously conducted using a two-cylinder test [12-14]. These laboratory studies revealed the following: wear is promoted by decarburized layers, but the effect on RCF is small because decarburized layers are shallow compared to the depth of the maximum applied shear stress or the RCF crack propagation mechanism. However, the two-cylinder test conditions adopted a slip ratio of ～1%-4.5%, and head checks were targeted. Therefore, the aforementioned test was not appropriate to be applied to squats in straight rail sections.

Thus, in this study, we investigated microcracks and decarburization layers in rail steels through laying tests. In laying tests, specimens, or actual rails with decarburization layers were compared to those without decarburization layers.

2. Survey of rail decarburized layer formation

Survey targets were 50-kg·N rails and 60-kg rails manufactured in Japan as specified in JIS E1101 [15]. The number of rails was 30 and the rails had no heat history. The depth of the decarburized layer was measured at the depth of the closed ferrite network specified in ISO3887 [16]. The evaluation of decarburized layer depth complied with the method defined in ISO 5003; the observed cross section was in the longitudinal direction of the rail and the observation position in the width direction of the rail was at the center of the width of the rail head. After the observed cross section was mirror polished and corroded with 5% Nital, metallographic photographs were taken.

A decarburized layer with thickness of about 0.14 to 0.45 mm was formed on the 30 new rails. The average depth of the decarburized layer of the surveyed rails was 0.29 mm, and the standard deviation was 0.14 mm. Figure 1 shows a photograph of the metal structure of the average investigated decarburized layer depth.

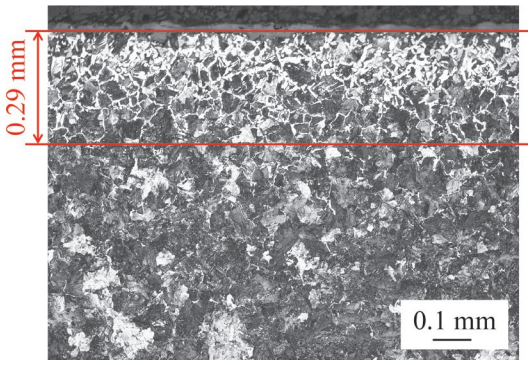

Fig. 1 Example photograph showing typical metallographic structures of new unused rails

3. Investigation of decarburized layer and microcracks by laying tests

3.1 Investigation method

For rails with different decarburized depths, partial rail replacement was performed every constant passing tonnage and microcrack formation was investigated. Metallographic observation was performed on a surplus portion of rails generated during rail replacement with new rails. The sections where the decarburized depth of each rail at the replacement point had been examined in advance were selected as investigation locations. For applicable rails, partial rail replacement was performed every 10 to 50 MGT in cumulative passing tonnage.

The relationship between the decarburized depth and passing tonnage and microcrack formation was investigated. For part of the investigated section, the rail top surface was ground with a one-grindstone-type rail grinder so that it had no decarburized layer. Figure 2 outlines the replacement and grinding of the rails. The track conditions of the selected investigation locations were a straight section, a double-track section, and a station-to-station section. Rail replacement and rail grinding were performed for these line sections in the stages described below.

Stage I: A 'New Rail 1' was laid in place of an 'Existing Rail.' During the rail replacement, a new rail surplus portion was generated, and part of the Existing Rail (A in Fig. 2) was provided to us. Metallographic observation was conducted to investigate the decarburized depth and crack formation status.

Stage II: Two weeks after the New Rail 1 was laid, the decarburized layer on the rail top surface was removed using a one-grindstone-type rail grinder on a selected portion of the New Rail 1.

Stage III: Twelve months after the 'New Rail 1' was laid, rail replacement was performed for a part of the 'Existing Rail Section' (B in Fig. 2), the 'New Rail 1' (C in Fig. 2) and the 'Rail Grinding Section' (D in Fig. 2). Microcrack formation status was investigated.
The newly replaced section was defined as the 'New Rail 2.' Metallographic observation of the surplus portion generated at the replacement was performed and the decarburized depth was investigated.

Stage IV: Six months after the New Rail 2 was laid, rail replacement was performed for the 'Existing Rail Section' (E in Fig. 2), the 'New Rail 2' (F in Fig. 2), and the 'Rail Grinding Section' (G in Fig. 2). Microcrack formation status was investigated.

3.2 Removal of decarburization layer via grinding

In this investigation, the rail top surface was ground using a one-grindstone rail grinder to create a section with no decarburized layer. Regarding the decarburized depth trend of the New Rail, the average decarburized depth of new rails was 0.29 mm. Figure 3 shows the appearance of the ground rail top surface and Fig. 4 shows the grinding amounts calculated from the rail profile measurements made for unground and ground rail profiles. No temper color due to overheating during grinding was observed in the grinding trace and the grinding finish was good. The grinding amount of the rail top surface, which ranged ±20 mm from the center of the rail width, was generally about 0.40 to 0.80 mm.

3.3 Decarburization layer depth of each rail

After a rail is laid, its wear progresses due to repeated contact with wheels. Therefore, surplus portions generated at the replacement were used to examine decarburized layers formed during the rail manufacturing stages. To examine the decarburized layer of the Existing Rail, the decarburized depth was investigated via metallographic observation of a railhead portion not in contact with wheels because it was assumed that wear had already progressed. Figure 5 shows photographs of the metallographic structures of the rails. A decarburized layer had formed in each of the rails with a depth of ~0.21 to 0.42 mm. In addition, the rail grinding amount in the previous subsection was generally about 0.40 to 0.80 mm; therefore, the decarburized layer on the section where one-grindstone-type rail grinding was performed (New Rail 1) was considered to have been removed. Figure 6 shows the distribution of carbon concentration of a New Rail 1 test piece by an EPMA. The quantitative evaluation of carbon concentration obtained via an EPMA was similar to the result obtained by measuring the depth of the decarburized layer. Table 1 summarizes the decarburized depths of the rails, also including the passing tonnage at rail replacement during the investigation.

3.4 Measurement of microcracks via metallographic observation

For each rail with different decarburized depths and passing tonnages, a metallographic observation was performed on the cross section in the rail-width direction to investigate microcrack formation status. The running bandwidth is different for each rail; therefore, metallographic observation was performed near the center of the section where the running bandwidth was common among the rails. Metallographic observation was performed at a length of about 150-mm length in the longitudinal direction of the rail.

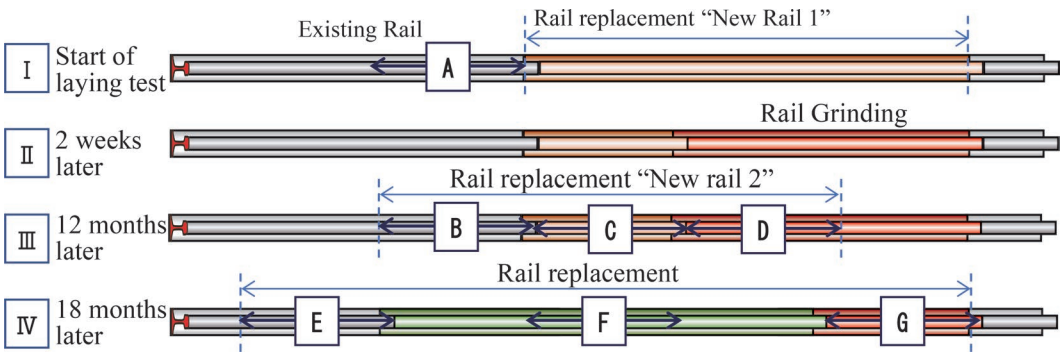

Fig. 2 Outline of replacement and grinding of rails

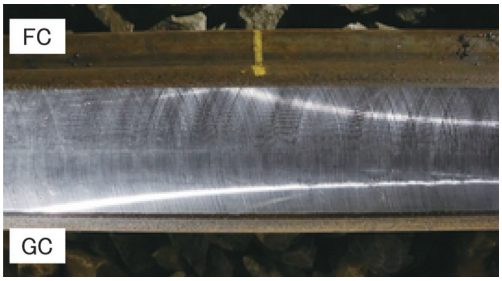

Fig. 3 Ground rail top-surface appearance

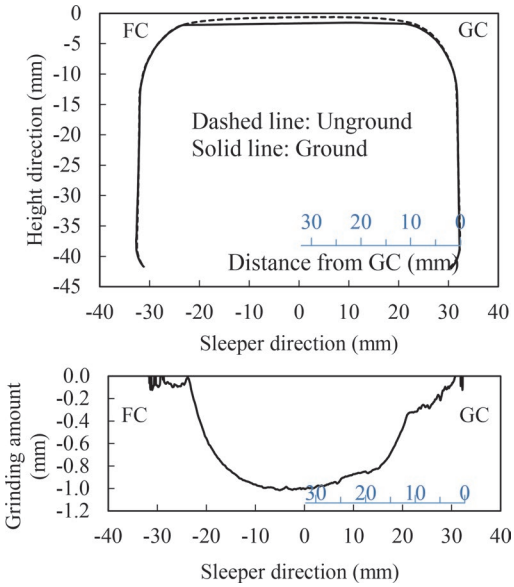

Fig. 4 Unground and ground rail profiles (upper: rail profile; lower: grinding amount)

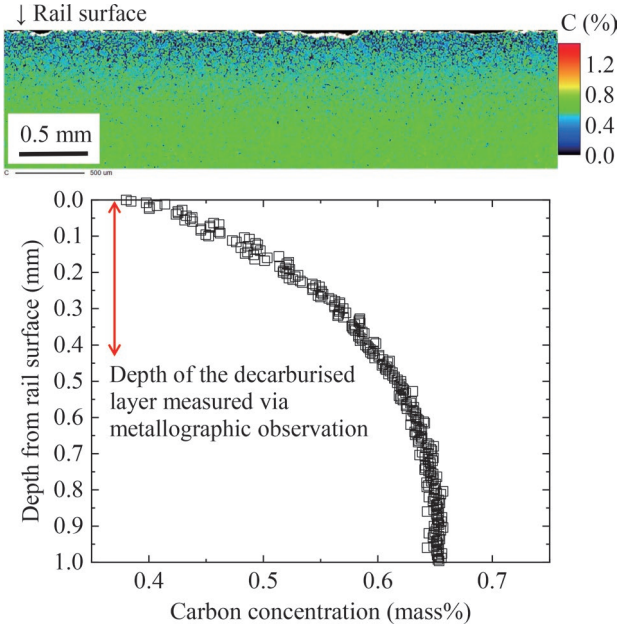

Fig. 6 Carbon concentration distribution for the New Rail 1 test piece obtained by EPMA

Table 1 Decarburized depths of rails and passing tonnages at replacement

Symbol	Designation	Grinding history	Decarburized depth (mm)	Passing tonnage (MGT)
A	Existing Rail	No	0.31	18
B	Existing Rail	No	0.31	41
C	New Rail 1	No	0.42	23
D	Ground Rail	Yes	0	23
E	Existing Rail	No	0.31	52
F	New Rail 2	No	0.28	11
G	Ground Rail	Yes	0	34

Figure 7 shows photographs of typical microcracks observed in each rail (left) and photographs of locations where these cracks formed after corrosion by 5% Nital (right). Tables 2 summarizes the microcrack formation results observed for each rail. Shading in the table indicates that the rails are from the same production lot. The order of the table is based on the number of passing tonnages and the history of rail grinding. Regarding the scope of measurement, this investigation excluded cracks with a length of 10 μm or less, which become wear debris or are difficult to identify, and those with no inward extension of the rail. Figure 8 shows boxplots and whisker plots describing the cracks on the rails. The whisker lengths indicate the maximum and minimum lengths of the measured cracks. The line in the middle of the boxplot represents the average and the width between the top and bottom lines represents the standard deviation. Figure 9 shows the relationship between crack density and passing tonnage.

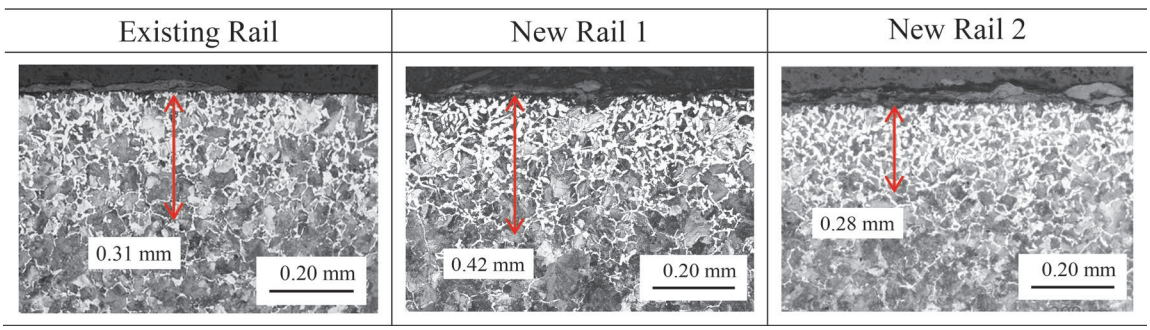

Fig. 5 Decarburized depths of each rail type

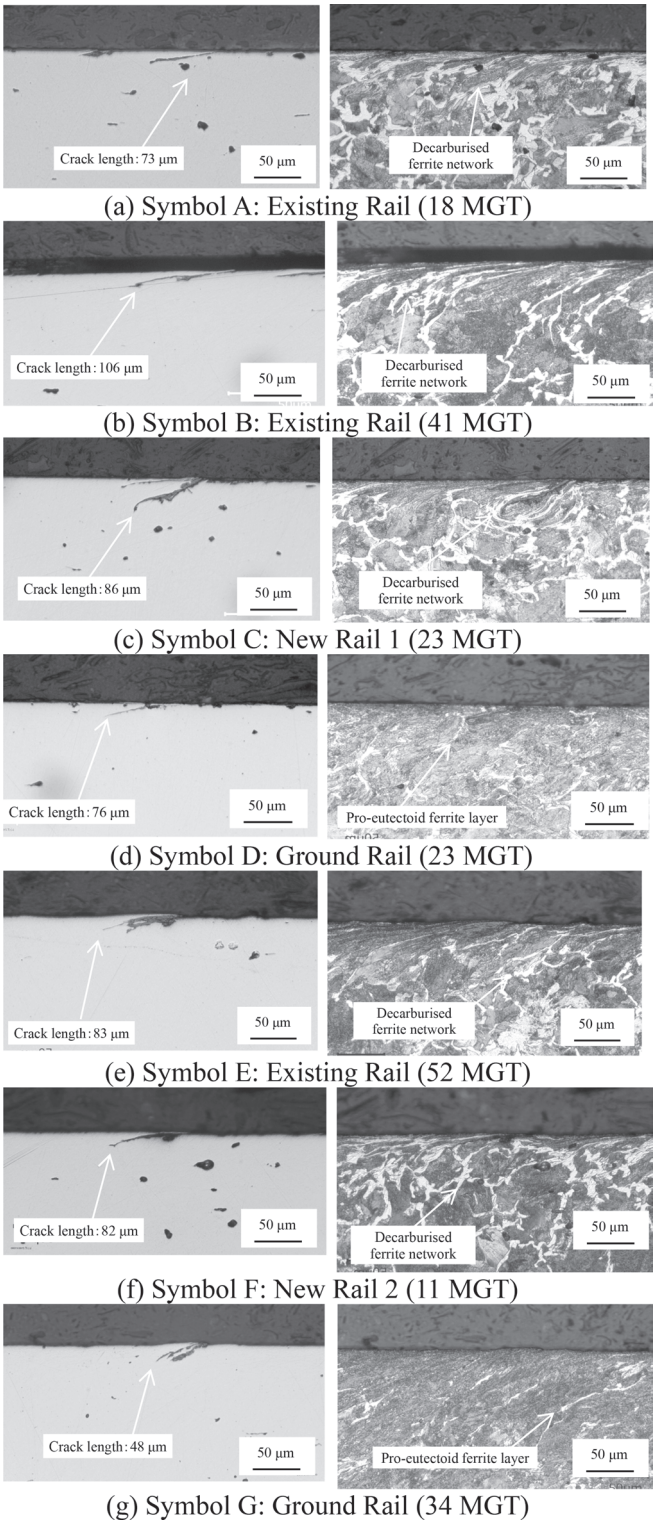

Fig. 7 Example of metallographic observations of each rails

4. Discussion

4.1 Crack density and decarburization layer

All unground rails had a remaining decarburized layer and, near their microcracks, had a plastic flow layer and decarburized layer generated by contact with wheels. Further, a decarburized layer was confirmed in rail E, which had the largest passing tonnage among all the rails. This is because the depth of the decarburized layer was larger than the amount of wear at the observation position. This plastic flow layer was considered to be formed by a partial slipping in a contact patch against wheels.

Rails D and G were sufficiently ground and decarburized layers were removed. A ferrite layer, which is pro-eutectoid ferrite formed in the equilibrium state of the steel of the rail composition, was partially observed via metallographic observation for rails D and G. Rail C (New Rail 1) and D (Ground Rail) having the same decarburized depths formed during manufacture, were located, respectively where grinding was performed or not after rail laying. Since their passing tonnages were identical (23 MGT), the difference in the existence of the decarburized layer has meaning for evaluation.

The crack density of the rail having a decarburized layer was ～5.7 times higher. Focusing on the measured maximum crack length, the crack length of the rail having a decarburized layer was approximately 1.5 times longer than that of the rail whose decarburized layer was removed. Previous studies [17] have reported the influence of RCF crack initiation by pro-eutectoid ferrite using a testing machine. The results of this field tests agreed with those reports. However, no remarkable difference was found in crack depth. Considering that the observed crack depth was almost the same as the depth of the plastic flow layer, it is probable that the passing tonnage was not large enough to affect the crack depth until these cracks significantly grew.

4.2 Crack formation due to increased passing tonnage

Rails A, B and E were all the same Existing Rail, except that their passing tonnages were different (18, 41 and 52 MGT, respectively). This allowed us to evaluate the changes in crack formation due to increased passing tonnage. The crack density tended to increase as the passing tonnage increased.

It was previously reported that squat increases with rail age, that is, passing tonnage [18]. Observations for a passage tonnage of up to 50 MGT have revealed that the number of microcracks caused by the decarburized layer also increased. These microcracks may grow into squats as passing tonnage increases. However, it must also be considered that squats disappear due to wear and competition after the formation of microcracks.

4.3 Effect of grinding

Rail G was ground after rail laying and reached a passing tonnage of 34 MGT. The crack densities at its investigation location were ～0.30 cracks/mm; these cracks were less severe than those observed at Rail F (unground rail with a passing tonnage of 11 MGT) in terms of crack density (0.77 cracks/mm). From this result, the first rail grinding after laying can be considered to have reduced the number of cracks by removing decarburized layers. However, even when rail grinding was performed, microcracks were observed on the rails. Previous studies have indicated that pro-eutectoid ferrite in hypoeutectoid steels may cause squats [19]. Since the rail studied here is also hypoeutectoid steel, this could be the cause of the observed microcracks.

4.4 Progression of microcracks to squats and effects of grinding

Crack propagation is related to factors such as wheel load change, track irregularity [20], residual stress [21] in rails and the

Table 2 Microcrack formation results of each rail

Symbol	Grinding	Decarburized depth (mm)	Passing tonnage (MGT)	Number of cracks	Crack density (cracks/mm)	Crack length (μm)		Crack depth (μm)		Remaining decarburized depth (mm)
						Average value	Maximum	Average value	Maximum	
F	No	0.28	11	115	0.77	33.4	46	9.0	21	0.11
A	No	0.31	18	96	0.64	29.5	37	8.0	21	0.20
B	No	0.31	41	95	0.63	44.6	93	9.9	20	0.13
E	No	0.31	52	161	1.07	40.2	86	10.4	29	0.07
D	Yes	0	23	21	0.14	35.9	52	7.3	14	0.00
C	No	0.42	23	120	0.80	35.4	80	10.1	41	0.18
G	Yes	0	34	45	0.30	47.5	28	8.7	36	0.00

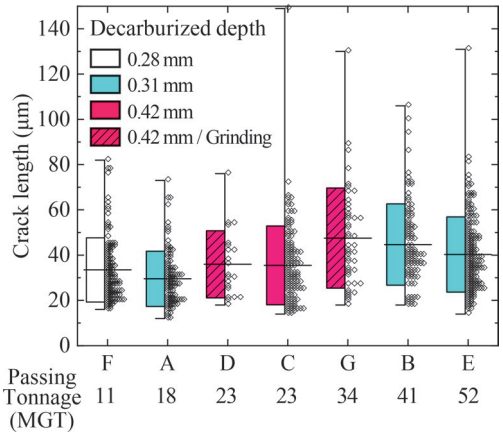

Fig. 8 Microcrack formation status of each rail

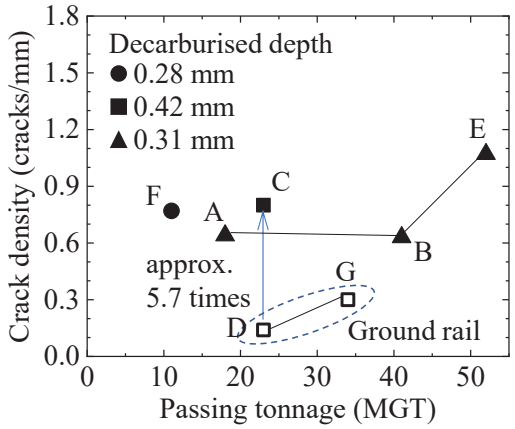

Fig. 9 Relationship between crack density and passing tonnage

effect of liquid inside the crack [22]. In the range analyzed in this study (150 mm rail length), more cracks were present in rails with decarburized layers than in those without decarburized layers. The potential for these cracks to propagate into squats is related to the aforementioned factors. Therefore, it was not possible to confirm whether the microcracks investigated in this study grow directly into squats, but it is thought that the relationship between microcracks and decarburized layers, which could be the initial of squats, could be understood.

Since all the observed crack depths were <0.1 mm, the cracks will be removed by grinding 0.1 mm at a cumulative passing tonnage of 50 MGT, which is a general rail grinding index in Japan [9]. However, squats occur at ≤50 MGT [23]; and there is a high tendency for squats to occur when rail grinding is performed at a passing tonnage of ≥50 MGT after the rail laying [24]. However, we are unsure whether these are caused by rolling fatigue or white etching layers. According to the analysis results of rails with 50 MGT or less in this investigation, the crack density and the maximum crack length tended to increase due to the decarburized layers. Therefore, we need to consider the operation of a rail grinding machine and the grinding cost, but rail grinding at a passing tonnage of less than 50 MGT may reduce cracks that cause squats.

5. Conclusion

To identify the effects of decarburized layers of rail surfaces on crack initiation, the effect of the decarburized layer was confirmed via the laying test on the same line section.

(1) In the laying test, a comparison between unground rails (with a decarburized layer) and ground rails (no decarburized layer) at a cumulative passing tonnage of 23 MGT showed that the crack density of rails with a decarburized layer was ～5.7 times higher, and the maximum crack length of the rails was ～1.7 times larger than that of rails whose decarburized layer was removed.

(2) For rails that experienced grinding shortly after rail laying and then reached a passing tonnage of 34 MGT (with no decarburized layer), the crack densities at investigation locations were approximately 0.30 cracks/mm. Micro crack formation was less severe than in the case of the rail having crack densities (0.77 cracks/mm) which experienced a tonnage of 11 MGT without grinding (with decarburized layers). The removal of decarburized layers by grinding effectively suppressed microcrack propagation.

(3) In the range analyzed in this study (150 mm rail length), more cracks were present in rails with decarburized layers than in those without decarburized layers. Therefore, it is not possible to confirm whether the microcracks investigated in this study grow directly into squat, but it is thought that the relationship between microcracks and decarburized layers, which could be the initial of squats, could be understood.

References

[1] Steenbergen, M. and Dollevoet, R., "On the mechanism of squat formation on train rails-part I: origination," *International Journal of Fatigue*, 47, 2013.

[2] Li, Z., Zhao, X., Esveld, C., Dollevoet, R. and Molodova, M., "An investigation into the causes of squats - Correlation analysis and numerical modeling," *Wear*, 265, 2008.

[3] Li, Z., Lewis, R. and Olofsson, U., "Squats on railway rails," *Wheel-rail interface handbook,* Woodhead Publishing, Cambridge, pp. 409-436, 2009.
[4] Grassie, S. L., "Squats and squat-type defects in rails: the understanding to date," *Proc Inst Mech Eng F: J Rail Rapid Transit*, pp. 235-242, 2011.
[5] Simon, S., "Tribological characterization of rail squat defect," *Wear*, 297, 2013.
[6] Grassie, S. L., "Rolling contact fatigue on the British railway system: treatment," *Wear*, 258, 2005.
[7] Kozeki, M. and Kataoka, K., "Research and development for improvement of reliability of rails," *JR EAST Technical Review*, No. 9, 2007.
[8] Kondo, K., "Cause, increase, diagnosis, countermeasures and elimination of Shinkansen shelling," *Wear*, 199, 1-2, 1996.
[9] Ishida, M., Abe, N. and Moto, T., "The Effect of Preventive Grinding on Rail Surface Shellings," *Quarterly Report of RTRI*, 39, 3, pp. 136-141, 1998.
[10] Parrish, G., "Carburizing. Microstructures and Properties," *ASM International*, 1999.
[11] Vander Voort, G. F., "Understanding and measuring decarburization," *Advanced Material and Processes*, 173, 2, pp. 22-27, 2015.
[12] Carroll, R. I. and Beynon, J. H., "Decarburization and rolling contact fatigue of a rail steel," *Wear*, 260, 2006.
[13] Zhao, X. J., Guo, J., Wang, H. Y., Wen, Z. F., Liu, Q. Y., Zhao, G. T. and Wang, W. J., "Effects of decarburization on the wear resistance and damage mechanisms of rail steels subject to contact fatigue," *Wear*, 364-365, 2016.
[14] Zhao, X. J., Wang, H. Y., Guo, J., Liu, Q. Y., Zhao, G. T. and Wang, W. J., "The effect of decarburized layer on rolling contact fatigue of rail materials under dry-wet conditions," *Engineering Failure Analysis*, 91, p. 58-71, 2018.
[15] Japanese industrial Standard (JIS) E 1101 "Flat bottom railway rails and special rails for switches and crossings of non-treated steel," 2001.
[16] ISO 3887 "Steels - Determination of the depth of decarburization," 2017.
[17] Deng, X., Qian, Z., Li, Z. and Dollevoet, R., "Investigation of the formation of corrugation-induced rail squats based on extensive field monitoring," *International Journal of Fatigue*, 112, 2018.
[18] Muhamedsalih, Y., Hawksbee, S., Tucker, G., Stow, J. and Burstow, M., "Squats on the Great Britain rail network: Possible root causes and research recommendations," *International Journal of Fatigue*, 149, 2021
[19] Stock, R., Kubin, W., Daves, W. and Six, K., "Advanced maintenance strategies for improved squat mitigation," *Wear*, 436, 2019.
[20] Andersson, R., Torstensson, P. T., Kabo, E., Larsson F. and Ekberg, A., "Integrated analysis of dynamic vehicle-track interaction and plasticity induced damage in the presence of squat defects," *Wear*, 366-367, 2016.
[21] Trollé, B., Baietto, M. C., Gravouil, A., Mai, S. H. and Nguyen-Tajanb, T. M. L., "XFEM Crack Propagation Under Rolling Contact Fatigue," *Procedia Engineering*, Vol. 66, 2013.
[22] Bogdański, S., "Quasi-static and dynamic liquid solid interaction in 3D squat-type cracks," *Wear*, 314, 1-2, 2014.
[23] Yamane, H., Imanishi S. and Tatsumi, S., "About the tendency of shelling and the preventive effect of rail rectification," *Japan Society of Civil Engineers 2017 Annual Meeting Proceedings*, 2017 (in Japanese).
[24] Gotoh, K., "Study on the effect of suppressing shelling by initial rail rectification," *Japan Society of Civil Engineers 2017 Annual Meeting Proceedings*, 2017 (in Japanese).

Authors

Yoshikazu KANEMATSU, Ph.D.
Senior Researcher, Frictional Materials Laboratory, Materials Technology Division
Research Areas: Rolling Contact Fatigue and Wear, Track Materials

Naotaka UEHIGASHI
Assistant Senior Researcher, Frictional Materials Laboratory, Materials Technology Division
Research Areas: Rolling Contact Fatigue and Wear, Track Materials

Motohide MATSUI, Ph.D.
Director, Head of Materials Technology Division
Research Areas: Wheel/Rail Interaction, Rolling Contact Fatigue and Wear, Track Materials

Inspection Method of Track Facilities Using Image Analysis of Images Taken from Front of Trains

Nozomi NAGAMINE **Wataru GODA** **Riho MAEDA**
Image Analysis Laboratory, Information and Communication Technology Division

Yosuke TSUBOKAWA **So KATO**
Track Geometry and Maintenance Laboratory, Track Technology Division

Kensuke ITOI
Track Geometry and Maintenance Laboratory, Track Technology Division (Former)

Appropriate maintenance of tracks is vital for the safe operation of railways. Properly managing track facilities is necessary to prevent buckling of rails. Changes in society are creating a shortage of workers, a decrease in skilled engineers, a decrease in passenger income, and an increase in the need to develop low-cost inspection methods which do not require experience. Therefore, we have developed a method using only inexpensive camcorders, which can extract information from images to detect joint gaps, wooden sleeper deterioration and ballast shape, and estimate the kilometer point of these images to locate the installations in question. This paper describes the outline of the method and its application results.

***Key words*:** *image analysis, train front image, track facilities, inspection*

1. Introduction

Proper track maintenance is important to ensure safe operation of railways. Track information related to buckling stability in particular needs to be verified and track facilities properly managed. However, a shrinking workforce and decreasing passenger revenue are leading to a shortage of workers and skilled technicians. As a result, it is necessary to develop low-cost methods to inspect the condition of track facilities that do not require special experience.

Therefore, we have developed a method to extract information about the condition of track facilities related to vehicle running safety from images taken from the front of a train using only an inexpensive and easily obtainable handy camera. The extracted information includes the size of joint gaps, the degree of sleeper deterioration, whether a fastening device has fallen off, and the width of the ballast bed shoulder and the height of excess ballast for determining the lateral resistance of the ballast bed. Automating inspections that have been previously performed on foot or by using special vehicles can reduce costs, increase inspection frequency, and make inspections more flexible depending on the situation.

This paper describes the following developed methods: a projective transformation method that converts images taken from the front of trains taken by train-mounted handy cameras into an under-floor image for inspecting the condition of track facilities, a kilometer estimation method for each image to identify the location of facilities to be inspected, a rail spacing measurement method, a method for determining the deterioration of wooden sleepers, and a method for estimating ballast bed geometry. In addition to describing the methods, this paper also reports on the results obtained from the application of these methods.

2. Generation of underfloor images by a projective transformation

2.1 Capturing forward-facing images from a train cab

When photographing a track surface, it is desirable to install a handy camera to obtain a bird's-eye view from directly above. However, considering that the camera is installed in the driver's cab of a train, we took images diagonally downward from the cab as shown in Fig. 1. In this case, the lower part of the captured image will be large because the distance from the camera is close, and the upper part of the image will be small because the distance from the camera is far. When acquiring information about track facilities by image analysis, there should be no difference in scale depending on the coordinates in the image. Therefore, we transformed the acquired image using a method called projective transformation to generate an underfloor image as if it were a bird's-eye view of the track surface from directly above.

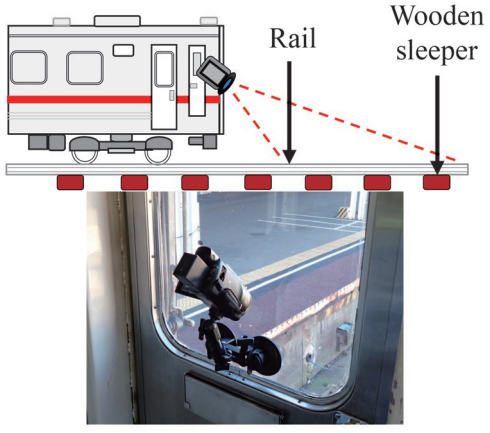

Fig. 1 Example of capturing images in front of a train

2.2 Underfloor imaging by a projective transformation

In this section, we describe projective transformation in two dimensions. Each pixel in an image can be denoted as a point in two-dimensional space, and its coordinates are represented by two values $\boldsymbol{x} = (x, y, 1) \in \mathbb{R}^3$. The coordinates before the transformation are denoted by $\boldsymbol{x}$, and the coordinates after the transformation are represented by $\boldsymbol{x}'$, and the geometric transformation in two dimen-

sions can be expressed by (1) when expressed by matrix multiplication in the homogeneous coordinate system.

$$x' = Mx \quad (1)$$

In this case, the type of geometric transformation depends on the matrix **M**. Table 1 shows that the type of geometric transformation depends on the matrices corresponding to the transformations, and Fig. 2 shows the concept of each transformation. Where $\boldsymbol{I}$ denotes the unit matrix, and $\boldsymbol{R}$ denotes the rotation matrix.

In the case of transforming a forward-facing image taken from the front of a train to an underfloor image, since the transformation is from a trapezoid to a rectangle, a projective transformation is used, which can transform any four of these two-dimensional geometric transformations to any four points. The homography matrix $\boldsymbol{H}$ can be calculated by solving a system of simultaneous equations if the four corresponding points are known. Figure 3 shows an example of an underfloor image of the front of the train using the projective transformation. Figure 3 shows that the trapezoid points *abcd* have been transformed into the rectangle *a'bcd'*.

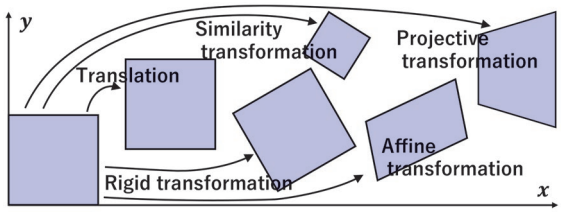

Fig. 2 Basic 2D geometric transformations

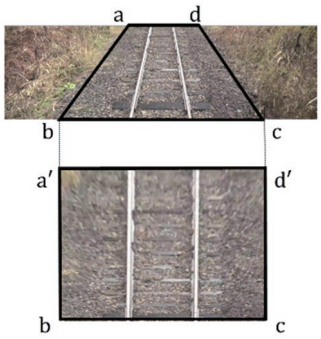

Fig. 3 Track Image by projective transformation

Table 1 Matrices corresponding to 2D geometric transformations

Transformation	Matrix	Degree of freedom
Translation	$[\boldsymbol{I}\|t]_{2\times3}$	2
Rigid transformation	$[\boldsymbol{R}\|t]_{2\times3}$	3
Similarity transformation	$[s\boldsymbol{R}\|t]_{2\times3}$	4
Affine transformation	$[\boldsymbol{A}]_{2\times3}$	6
Projective transformation	$[\boldsymbol{H}]_{3\times3}$	8

3. Kilometer estimation [1]

3.1 Purpose of kilometer estimation

Since railway facilities are maintained and managed on the basis of kilometers corresponding to the position of installations, it is necessary to calculate kilometers for each frame of the image in front of the train when inspecting by image analysis. Therefore, we calculate the kilometers from the front image of the train.

3.2 Calculation of train speed by optical flow

Although there are methods to calculate the velocity field between two images by template matching, these are sparse methods that calculate the velocity field for only some pixels. We used the optical flow method, which is a dense method that calculates the velocity field of all pixels in the image. This allows us to calculate the velocity field for every pixel in the image. We removed outliers by finding the mode of the calculated velocity field, and found the velocity vector in this frame as the moving velocity of the train [pixel/frame].

3.3 Correspondence with kilometers

The algorithm creates per-pixel distance data accumulating the speed of pixel movement in each frame. If the distance at the start of the video is zero, the pixel distance at frame is obtained by integrating the velocity from zero to t. Using the pixel unit distance data for the image frame and the reference data for the frame such as the kilometer distance of the station, the image frame-pixel unit distance is scaled up or down for each section of the reference data to create the kilometer distance data for the image frame.

Figure 4 shows the running curves calculated with the proposed method and the running curves calculated with the conventional method, template matching, for the same run. The conventional method has many obvious calculation errors around 0.9 km to 1.8 km, while the proposed method has almost no errors. This indicates that the proposed method calculates speeds with fewer errors than the conventional method.

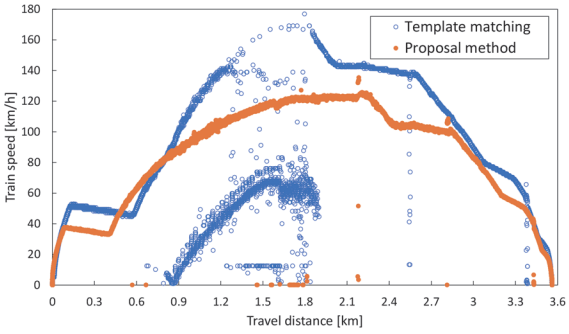

Fig. 4 Calculated run curve

4. Joint gap measurement [2]

4.1 Purpose and overview of joint gap measurement

Since rails expand and contract due to the axial force generated by the rise and fall of rail temperatures, it is necessary to control the gap between the ends of adjoining rails at the joint (joint gap) to

prevent rail buckling or breaking, which can lead directly to accidents. During joint gap inspection, a rail maintenance engineer measures the size of the gap at each joint using a gap gauge, compares the results with a reference value, and judges whether the gap is admissible (as in within a pre-determined admissible range). If the joint gaps are below the reference value, the specified gap size cannot be secured (no gap) at hot temperatures in summer, so the joint gaps need to be straightened. Until now, joint gap measurement work has been done on-site. Therefore, to replace on-site joint gap measurement work with photographing of the track surface by a train attendant, we developed a method to measure the joint gap using image analysis from the captured images.

4.2 Extraction of joint locations

To inspect joint gaps from images taken from the front of a train, it is necessary to extract joints from the image. Therefore, we extracted rail joints using deep learning. We used YOLOv4 as the network architecture, the method for the simultaneous detection and identification of objects. When the input image is applied to the YOLOv4 discriminator, the obtained outputs are: the object category, the confidence (probability) of the category class, the horizontal position, the vertical position, the width, and the height. As training data, we specified that the entire structure of the joint, including the joint board and the bolts, fits into the training region, and used a total of 3,127 images (437 images with joint tags and 2,690 jointless images). Figure 5 shows an example of the results of deep-learning joint extraction.

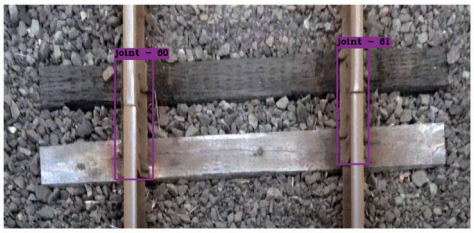

Fig. 5 Extraction result of two joints

4.3 Extraction of joint locations

Figure 6 shows the basic concept of the joint gap measurement algorithm. First, a "rail image without a gap" is pseudo-created by performing moving average processing in the longitudinal direction of the rail on the "rail image with a gap" that was taken. The joint gap (pixel) is calculated by labeling the shape obtained by the difference between the two images. Next, the vertical size of the joint plate that fastens the rail is extracted from the image. The resolution of the image is calculated using the ratio of the number of pixels obtained from this process to the actual dimension of 560 mm. Finally, using the calculated image resolution, the gap calculated by the number of pixels in the image is converted into the length of the implementation (mm), and it is found that the gap is measured from the captured track image.

Figure 7 shows the results of measuring the joint gap using this method. The joint gaps in the left rail and the right rail are 4.8 mm and 11.6 mm, respectively, and the joint gap shapes extracted by the algorithm are overlaid in red. Since the joint gap inspection requires measuring the smallest point for safety reasons, the gap measurement algorithm uses the smallest value of the shape as the measurement value after noise elimination.

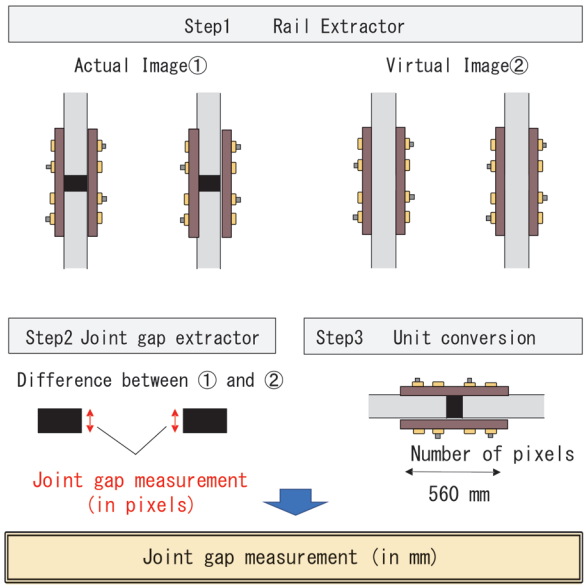

Fig. 6 Joint gap measurement algorithm

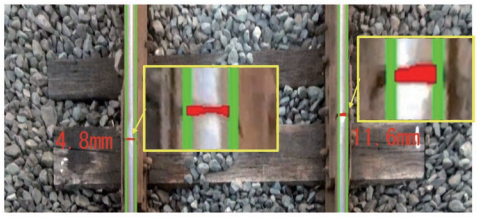

Fig. 7 Measurement results by image analysis

4.4 Accuracy of measurement of joint gaps

To verify the accuracy of the gap measurement algorithm, as shown in Fig. 8, the size of joint gaps measured by humans from images (horizontal axis) was compared with the size of joint gaps based on the algorithm (vertical axis). This figure has a strong correlation with a coefficient of determination of 0.95, so we can say that the algorithm estimated the values well. The maximum error was 2 pixels. Note that the image should be acquired at a resolution corresponding to the required accuracy for actual use in inspections.

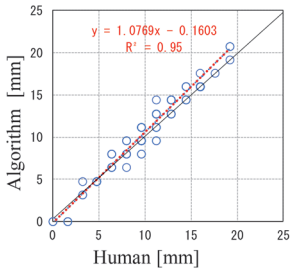

Fig. 8 Measurement results by image analysis

5. Determination of deterioration of wooden sleepers [3]

5.1 Purpose of determining deterioration of wooden sleepers

Deterioration of sleepers affect the reduction of rail fastening force and, if continuous, is a factor in vehicle derailment. Hence, the deterioration of wooden sleepers is a crucial element in assessing

the condition of track facilities in terms of vehicle running safety. Currently, sleepers are inspected individually by workers on foot. As an alternative to this work, we have developed an algorithm to determine the deterioration of each wooden sleeper based on images taken from the front of a train.

5.2 Criteria for judging deterioration of wooden sleepers

We extract sleepers and evaluate the degree of deterioration using a deterioration evaluation model trained by deep learning on underfloor images. Based on the deterioration judgment standard for wooden sleepers shown in Fig. 9, the model outputs a total of seven classes of evaluation: "A" and "B" for defective sleepers, "C" for minor damaged ones, "D" for good ones, "Uncategorized" for undiagnosed sleepers when the sleeper surface is hidden or buried or hidden by ballast, grass, etc., and "PC" for PC sleepers.

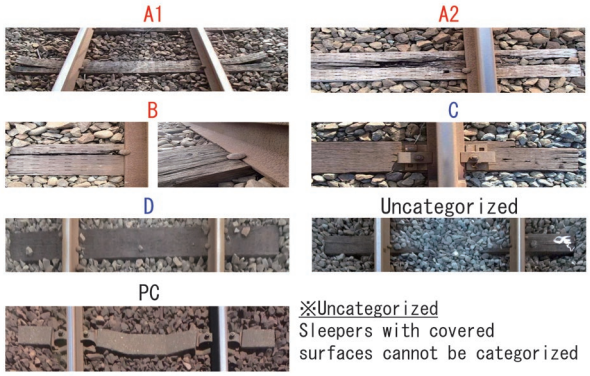

Fig. 9 Standards for judging the degree of deterioration of wooden sleepers

5.3 Extension of training data

As well known, Deep Learning has the property of discriminating categories with high accuracy by learning a large amount of image data. To extend training data, we assumed the influence of color tones due to weather and sun movement as environmental changes that may occur during actual shooting, creating four patterns with a ±60% strength in the brightness and light/dark ratio. In addition to these four patterns, assuming white noise and blurring may occur during shooting, we expanded the data by adding 1,000 pieces of noise and smoothing using random numbers to create two patterns. By combining these six image processing patterns, we increased the number of data in A2 and B by a factor of about 5 and the number of data in C by a factor of about 1.5. This process expanded the number of frames by a factor of 2, which was originally about 100,000, to build the model. We tagged about 370,000 sleepers for about 200,000 images.

5.4 Management of evaluation results

Since the same sleeper and rail joint are reflected in multiple frames, when plotted on the kilometer axis, the plots are clustered according to the number of shots of the same sleeper. Since the clustered plots are identical sleepers and rail joints, the clustered plots can be counted as a single facility. Therefore, we used the shortest distance method (single linkage method), which uses the shortest distance between plots among the cluster analysis methods, to classify the plots into classes. In this case, the number of classes is the number of sleeper and rail joints installed. Here, the threshold of the shortest distance between plots to be classified as different classes was set as follows. For sleepers, the threshold was set at 20 cm based on the vertical size, and for rail joints, the threshold was set at 1 to 2 m because the rail length is 10 m or longer in most cases. For the ranks of sleeper defects, we adopted the rank with the worst condition for intra-class identification so that the system would decide on the safe side.

5.5 Accuracy verification of degradation determination method

We evaluated the accuracy of the algorithm for judging the deterioration of wooden sleepers. We compared the results of the algorithm's evaluation with the results of the visual evaluation of the underfloor images by a maintenance engineer on 16,033 detected sleepers. Note that the results of visual evaluation by a maintenance engineer were used as the correct values for the evaluation. Figure 10 shows an example of the evaluation results, and Table 2 shows the percentage of correct answers for each degree of deterioration of the wooden sleepers. The percentage of correct answers for the degree of deterioration of the wooden sleeper is 88.6% for C, more than 90% for D and B to A, 72.1% for "not evaluated," and 98.5% for "PC." Although the accuracy of evaluation for C is inferior to that of the other deterioration levels, the average percentage of correct answers for D to A2 is more than 90%, indicating that the accuracy of evaluation of deterioration levels in this model is high. The sleeper detection accuracy was 16,033 (detection rate 99.5%) out of 16,111 total sleepers, indicating that the algorithm can detect sleepers with high probability.

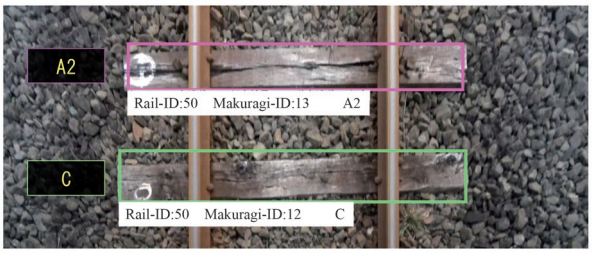

Fig. 10 Detecting wooden sleepers and determining the degree of deterioration

Table 2 A matrix corresponding to a 2D geometric transformation

	D	C	B	A2	no	PC
Human	10,476	3,387	1,292	404	208	266
System	9,662	3,001	1,178	380	150	262
Accuracy (%)	92.2	88.6	91.2	94.1	72.1	98.5

6. Rail fastener dropout detection [4]

6.1 Detection method for rail fastener dropout

On concrete sleeper and slab track, it is important to control the condition of rail fasteners, which are intensively inspected by foot patrols. To completely replace foot patrols with cameras, it is necessary to detect all the current inspection items, such as the overhang of track pads, etc. However, this study focused on rail fasteners, and developed a method to automatically detect rail fasteners based on images taken from the front of a train using deep learning detection

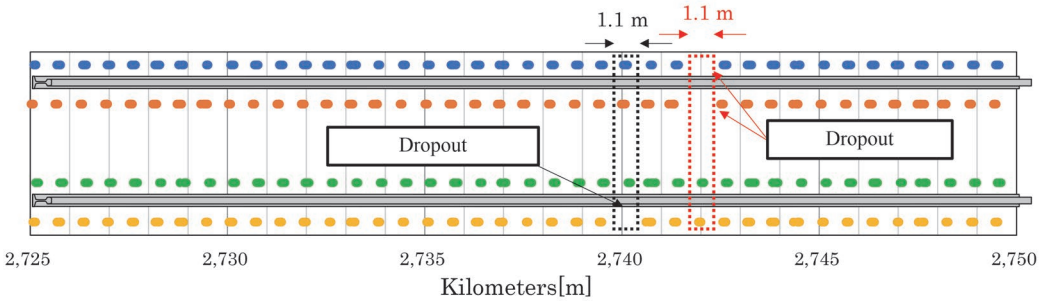

Fig. 11 Distribution of rail fasteners

and clustering as described in Chapter 5. The algorithm detects the locations where the calculated spacing of rail fastening devices is greater than the design value as the locations of rail fastening device dropouts.

6.2 Verification results of dropout detection

To verify the detection accuracy of the rail fastener, we processed and calculated the detection rate for about 2.8 km of images (about 16,000 images) taken. The results showed that the detection rate was more than 99.6%, indicating that the system detected with high accuracy. The main reasons for non-detection were due to shadows of overhead wires and vegetation, which were clearly not detectable even visually. As an example of the estimated locations of rail fastening device dropouts, the distribution of rail fastening devices is shown in Fig. 11. The plots of rail fastening devices are generally aligned at intervals of 0.6 m and can be accurately captured. In addition, the algorithm detected two cases where the spacing between rail fasteners was 1.0 m or more. The detected locations are shown in Fig. 12. Although the detection results are output with a mixture of "dropped" and "unextracted" locations of rail fastening devices, the practical impact is considered to be minimal.

7. Estimation of ballast bed geometry [5]

7.1 Purpose of ballast bed geometry estimation

One of the most important aspects of rail running safety is the lateral resistance of the ballast bed. The lateral resistance of the ballast bed is the resistance to sleeper movement in the left-right direction and plays a significant role in preventing rail buckling. Sufficient height and width of the ballast bed shoulder are required to ensure the lateral resistance of the ballast bed. The extra heights are the highest points of each of the left and right sleeper shoulders. The shoulder width is the distance from the edge of the sleeper to the point on the outside of the hemming where it is the same height as the edge of the sleeper. The smaller value is measured as the safe side during the inspection. Since the ballast bed is subject to settlement and collapse due to external factors such as a train running, it must be maintained periodically. Therefore, we have developed a method to estimate the shape of the ballast bed.

7.2 Estimation method of ballast bed geometry

To estimate the ballast bed geometry from undercarriage images transformed from forward-facing images taken from the train, we applied the principle of triangulation. Figure 12 shows a conceptual diagram of the principle. When the camera moves, objects close to the camera are captured with a larger displacement, and objects farther from the camera are captured with a smaller displacement. In other words, the relationship between the distance h from the camera and the amount of object movement l seen from the camera is proportional. Using this relationship, the shape of the ballast bed is estimated from the amount of movement. The amount of movement is calculated using the optical flow described in Chapter 3. The specific processing procedure is as follows:

(1) Perform a projective transformation on the captured forward-facing images from the front of the train to generate an underfloor image.
(2) From the information on the rail and its vanishing point in the image from the front of the train, the tilt angle of the camera and the distance from the camera to the object are derived, and these values are used to determine the height of the camera from the center of the track surface sleeper.
(3) Calculate the optical flow from the under-floor images of successive frames.
(4) Calculate the height of each point in the image from the ratio of the height of the camera to the height of the track surface obtained in the procedure above. Then estimate the cross-sectional shape of the ballast bed at that point.
(5) Form the three-dimensional shape of the ballast bed by connecting the cross-sectional shapes at each frame.

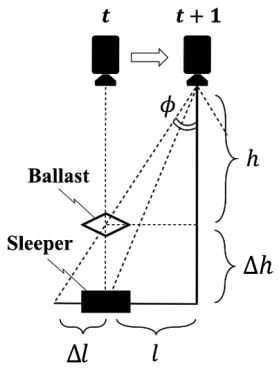

Fig. 12 Relationship between distance from camera and amount of movement

7.3 Estimation results of ballast bed geometry

Figures 13 and 14 show the results of the 3-D estimation of the ballast bed and its 3-D cross-sectional profile. The results correctly represent the extra heights of sufficient ballast at the sleeper ends. It was also confirmed that the ballast bed shoulder width and extra heights can be measured based on this cross-sectional view.

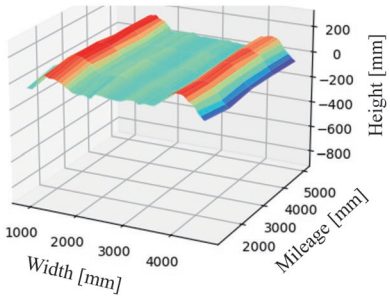

Fig. 13 Estimation result of 3-D shape of ballast

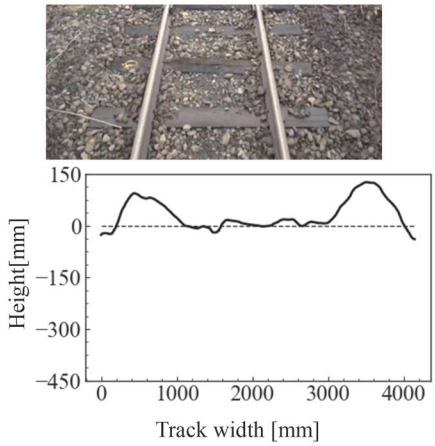

Fig. 14 Captured image and cross-sectional shape estimation results

8. Summary and future work

To reduce the cost of inspecting track facilities, we have developed the following methods: a projection transformation method to convert images taken by a handy camera from the front of a train into under-floor images for inspection, a kilometer estimation method for each image to identify the location of the inspected facilities, a method for measuring joint gaps, a method for determining deterioration of wooden sleepers, and a method for estimating ballast bed geometry. Each method has a detection and measurement performance of more than 90% and has the potential to be used in inspections. We will improve these methods for use in actual inspections. Since these image analysis technologies can be applied to systems other than track facilities, we will also investigate their application to other systems.

References

[1] Goda, W., Nagamine, N., Mukojima, H., Itoi, K., Tsubokawa, Y., and Kato, S., "Kilometrage Estimation by Optical Flow Using Forward View Image from Train Cab," *The Papers of the Technical Meeting on "Transportation and Electric Railway,"* IEE Japan, 2021 (55-57, 59), 17-22, 2021-07-13 (in Japanese).

[2] Itoi, K., Nagamine, N., Goda, W., Tsubokawa, Y., Oba, H., and Kato, S., "Application of Joint Gaps Measurement Method to Forward View Image from Train Cab," *TER = The Papers of the Technical Meeting on "Transportation and Electric Railway*," IEE Japan 2020 (69, 71-74, 76, 77), 29-32, 2020-10-02 (in Japanese).

[3] Itoi, K., Nagamine, N., Goda, W., Tsubokawa, Y., and Kato, S., "Improving Inspection Accuracy of Wooden Sleeper Deterioration Analysing Forward View Image from Train Cab," *J-RAIL 2021*, SS2-4-5, 2021 (in Japanese).

[4] Itoi, K., Nagamine, N., Goda, W., Tsubokawa, Y., and Kato, S., "Development of Dropout Detection Method for Rail Fastening System Using Forward View Image from Train Cab," *TER = The Papers of the Technical Meeting on "Transportation and Electric Railway,"* IEE Japan 2021 (20-28), 49-54, 2021-09-24 (in Japanese).

[5] Maeda, R., Nagamine, N., Itoi, K., Tsubokawa, Y., and Goda, W., "Basic Study of the Ballast Bed Shape Estimating Method Using Camcorder Video on the Train Cab," *TER = The Papers of the Technical Meeting on "Transportation and Electric Railway,"* IEE Japan 2022 (29, 31-41), 01, 03-13, 2022-02-28 (in Japanese).

Authors

Nozomi NAGAMINE, Ph.D.
Senior Chief Researcher, Head of Image Analysis Laboratory, Information and Communication Technology Division
Research Areas: Computer Vision, Image Processing, Signalling Systems

Yosuke TSUBOKAWA
Senior Chief Researcher, Head of Track Geometry and Maintenance Laboratory, Track Technology Division
Research Areas: Track Measuring

Wataru GODA
Researcher, Image Analysis Laboratory, Information and Communication Technology Division
Research Areas: Computer Vision, Image Processing

Riho MAEDA
Researcher, Image Analysis Laboratory, Information and Communication Technology Division
Research Areas: Computer Vision, Image Processing

So KATO
Researcher, Track Geometry and Maintenance Laboratory, Track Technology Division
Research Areas: Track Measuring

Kensuke ITOI
Researcher, Track Geometry and Maintenance Laboratory, Track Technology Division (Former)
Research Areas: Track Measuring

Evaluation Method for Implementation Effects of Disaster Countermeasures for Freight Railway Networks

Daiki OKUDA **Takuya WATANABE** **Shingo NAKAGAWA**
Data Analytics Laboratory, Information and Communication Technology Division

Takamasa SUZUKI
Data Analytics Laboratory, Information and Communication Technology Division (Former)

Noriko FUKASAWA
Data Analytics Laboratory, Information and Communication Technology Division

We developed a method for evaluating the effect of disaster countermeasures using two indices: volume of freight transportation on a freight railway network during disruptions caused by natural disasters and sum of costs borne by freight railway operators during restoration periods. The evaluation method aims to support train operator decision-making regarding implementation of disaster countermeasures. A case study applying the evaluation method demonstrated that the method could provide appropriate evaluation results contributing to decision-making by operators.

***Key words*:** *freight railway network, resilience, natural disaster, disaster countermeasure, decision-making, optimization calculation*

1. Introduction

Natural disasters are becoming more severe and more frequent. When they do occur, they often cause long-term disruption to railway freight transportation. Therefore, it is necessary to minimize the impact of natural disasters, even when they exceed expectations, by ensuring that freight transportation can continue as much as possible or by restoring it as early as possible. In other words, it is important to improve the resilience of railway freight transportation against disasters.

Under these circumstances, freight railway operators have designed business continuity plans (BCPs) in case of large-scale natral disasters, and as part of this, the operators have been considering various disaster countermeasures. However, resources that the operators can invest in disaster countermeasures are limited. Moreover it takes a lot of time to implement these countermeasures. Therefore, to maximize the effectiveness of investment in disaster countermeasures, it is desirable that decision-making by the operators regarding disaster countemeasures, such as judgment of the necessity of implementation or prioritization of implementation, is based on quantitative evidence.

Several studies have reported on methods for evaluating the effects implementing disaster countermeasures in Japan [1, 2], however they focused on mainly road networks. In addition, the evaluation indices in those methods were selected mainly considering benefits to users, such as reducing detour losses or opportunity losses in the event of disasters, and social benefits, such as preventing areas becoming isolated immediately after disasters, without considering the costs covered by the operators responsible for transportation.

Based on the above, to support decision-making by freight railway operators regarding implementation of disaster countermeasures, we developed a method for evaluating implementation effects of disaster countermeasures for freight railway networks [3, 4]. The evaluation method has two indices: DV and TC. DV stands for volume of freight transportation during restoration period. Restoration period means a period from the day a freight railway network is damaged by a disaster to the day when it is completely restored. TC is the sum of DC and IC. DC stands for the sum of restoration costs and additional transportation costs due to irregular transportation covered by the operators during the restoration period. IC stands for investment costs covered by the operators for implementation of disaster countermeasures.

In this paper, chapter 2 describes definitions of the study. Chapter 3 describes a method for evaluating the implementation effects of disaster countermeasures, including a method for estimating DV and TC. Chapter 4 describes a case study using the evaluation method and consideration of the results. Chapter 5 offers a conclusion and highlights future issues.

2. Definitions in this study

2.1 Freight railway networks

A freight railway network in this study consists of nodes corresponding to freight stations or signal stations and railway links connecting each node, as shown in Fig. 1. In addition, some nodes are also connected by road links which use substitute transportation by trucks. The number of railway links and road links connecting each node is limited to one each, and their lengths (km) are given in advance.

2.2 Freight demand and processing methods

Freight demand is defined as transportation orders generated for each OD on each day, and volume is obtained from values converted to the number of 12-ft containers, which is the most common unit for railway freight transportation. OD stands for Origin and Destination. To simplify calculations, freight demands for each OD on each day are regarded to be constant and their volumes are given in advance. In addition, transportation routes for freight demands in normal times are also given in advance. Moreover, although some of ODs require more than two days of transportation in normal times,

each transportation for all ODs in this study are defined as one-day transportations.

To process daily freight demands, one of the processing methods shown in Table 1 is applied to each demand. In the case of substitute transportation that combines railway and road transportation, the freights are transshipped between railway and trucks at a node in the middle of the route (hereafter referred to as "relay node").

Processing capacities of nodes and railway links are defined by constraints given in advance shown in Table 2. When nodes or railway links are damaged, processing capacities of these are temporarily lost until restoration work, described later, is completed. Since this study focuses on railway freight transportation when freight railway networks are damaged, road links are assumed not to be damaged by the disasters, and the upper quantity limit of freight transportation that can pass through is not also set.

The volume of freight that can be transported between each OD is defined by processing the capacities of origin nodes, destination nodes, relay nodes, and railway links in transportation routes. Processing capacities of nodes in the middle of transportation routes through which freights just pass (hereafter referred to as "pass node") have no effect on the volumes of freight that can be transported between each OD. In other words, if only pass nodes on a transportation route are damaged, freight transportation on that route can continue.

2.3 Restoration work

Restoration workers (persons/day) are dispatched to damaged nodes and railway links on each day. The processing capacity of damaged nodes or railway links is restored when the cumulative number of restoration workers (persons) dispatched to each damaged location has reached a certain number (persons) required to restore each damaged location. Since most railway links on the freight railway networks in Japan are managed by passenger railway operators, in this study, restoration workers that can be sent to damaged nodes and railway links are independent of each other.

It is assumed that restoration work for damaged nodes and railway links is carried out within the constraints given in advance, as shown in Table 3.

3. Method for evaluating effect of disaster countermeasures

3.1 Outline of the evaluation method

The purpose of disaster countermeasures for freight railway networks is to improve the resilience of railway freight transportation against disasters, and the ideal is that freight demand can be processed on each day without delay even in the event of large-scale disasters. In addition, considering the business continuity of freight railway operators, it is also necessary to consider the costs covered by the operators in the event of disasters. Therefore, DV and TC which is the sum of DC and IC are appropriate as indices to evaluate the effect of disaster countermeasures. Furthermore, the effect of disaster countermeasures is often evaluated by comparing two cases: the case when disaster countermeasures have been implemented, and the case without disaster countermeasures (status quo).

Based on the above, to quantitatively evaluate implementation effects of disaster countermeasures, as shown in Fig. 2, the difference in DV (index 1) and the difference in TC (index 2) between these two cases are used as evaluation indices. The methods for estimating DV and TC in each case are described later.

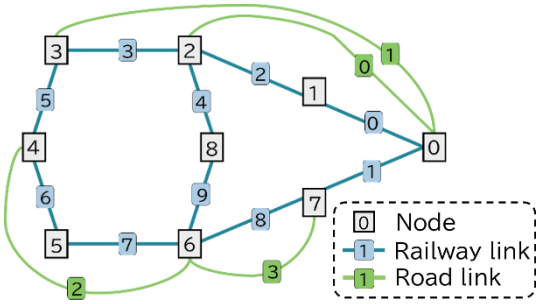

Fig. 1 Example of freight railway network

Table 1 Processing methods of freight

Regular transportation	Railway transportation on the same route as normal times (all freight demands are processed with this method in normal times)
Detour transportation	Railway transportation via different route to normal times
Substitute transportation	Transportation by truck only, or transportation by combining truck and railway
Storage	Store at an origin node for one day and add to next day freight volume
Return	Return to shippers without transportation or storage

Table 2 Constraints on processing of freight demands at nodes and railway links

node	Upper limit of freight volume per day that can be shipped/received by railway transportation (containers/day)
	Upper limit of freight volume per day that can be shipped/received by truck transportation (containers/day)
	Upper limit of freight volume per day that can be transshipped (containers/day)
	Upper limit of freight volume per day that can be stored (containers/day)
railway link	Upper limit of freight volume by direction per day that can pass through (containers/day)

Table 3 Constraints on restoration work

A certain number of restoration workers to restore each damaged node/railway link (persons)
Upper limit on number of restoration workers per day that can be dispatched to each damaged node/railway link (persons/day)
Upper limit of total number of restoration workers per day that can sent to all damaged nodes/railway links (persons/day)

The evaluation method can evaluate a wide range of disaster countermeasures, including hard measures such as strengthening equipment to improve the resistance of freight stations against disasters, and soft measures such as strengthening substitute transportation systems by truck to ensure redundancy of freight transportation.

3.2 Method for estimating DV and TC

Freight demands for each OD are processed using regular transportation in normal times. However, if nodes or railway links are damaged by a disaster, freight demands may have to be processed differently than normal times. In addition, once restored, nodes and railway links restore their processing capacities, so freight transportation conditions can be changed day to day during a restoration period. Therefore, to estimate DV and TC, it is necessary to estimate the restoration process of a freight railway network after a disaster and have a framework of processing methods for each day during the restoration period.

3.2.1 Estimating the restoration process of a freight railway network

When a node loses its processing capacity, only the freight demands which depart from or arrive at the node are affected. However, when a railway link loses its processing capacity, all freight demands transiting the railway link on route are affected, and thus the impact on freight transportation is likely to be large. Therefore, in this study, the restoration process of the freight railway network is estimated first on the basis of damaged railway links and damaged nodes second.

First, the restoration process of damaged railway links is estimated using optimization calculations aimed at minimizing the loss in freight transport volume, and assuming that all nodes maintain their processing capacities. Lost freight transport volume means, as shown in Fig. 3, the total quantity of freight transport on a freight railway network that cannot be transported by regular transportation during the restoration period. The reason why minimizing a quantity of freight transportation loss is set as the objective function is that the aim of restoration work is to restore transportation conditions back to normal times as soon as possible. Constraints of the calculation are shown in Table 3.

Secondly, the restoration process of damaged nodes is also estimated using optimization calculations aimed at minimizing lost freight transport volume, assuming that damaged railway links are restored according to the restoration process estimated in the previous step. Constraints of the calculation are also shown in Table 3.

The cost of restoring damaged nodes and railway links is calculated by multiplying cumulative numbers of restoration workers dispatched to each damaged node and damaged railway link until completion of restoration work at each location by the unit cost of restoration workers (yen/person-day). The unit cost of restoration workers for nodes and railway links are distinguished and both are given in advance.

Natural disasters can also cause extensive damage to social infrastructures other than railways, such as large-scale power outages or widespread flooding. As such, it is necessary to consider the impact of these constraints on restoration work, which may mean that the freight railway network restoration process is not ideal for minimizing loss of freight transportation volume. In response, it is possible to set different scenarios to defines the restoration process for damaged locations (hereafter referred to as a "restoration scenarios").

3.2.2 Determining processing method to apply on each day during a restoration period

Assuming that a freight railway network will be restored according to a process based on the approach described in the previous paragraph, it is possible to determine which processing method should be applied on each day during a restoration period. The processing methods are shown in Table 1, with the order of priority being regular transportation, detour transportation, substitute transportation, storage, and return. This order was defined on the basis of freight transportation records of past disasters and subsequent railway freight operator policies. Figure 4 is a flow chart showing how each processing method can be applied on each day of a restoration

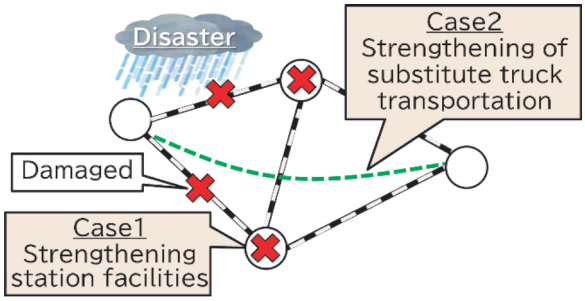

Disaster countermeasures	DV	TC	
		DC	IC
Case0 (Status Quo)	DV_0	DC_0	–
Case1	DV_1	DC_1	IC_1
Case2	DV_2	DC_2	IC_2

Calculated by estimating method

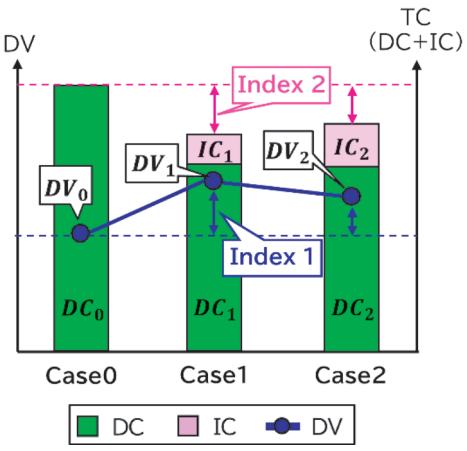

Fig. 2 Evaluation method of implementation effects of disaster countermeasures

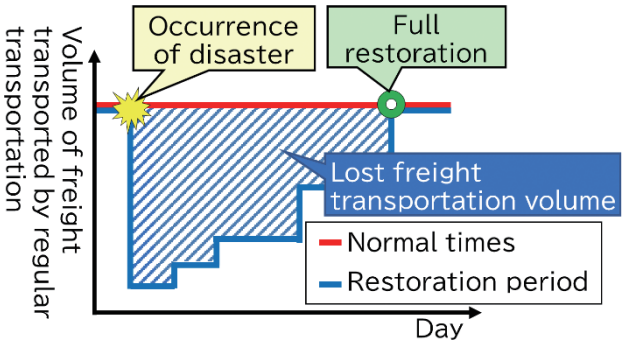

Fig. 3 Visualization of lost freight transportation volume

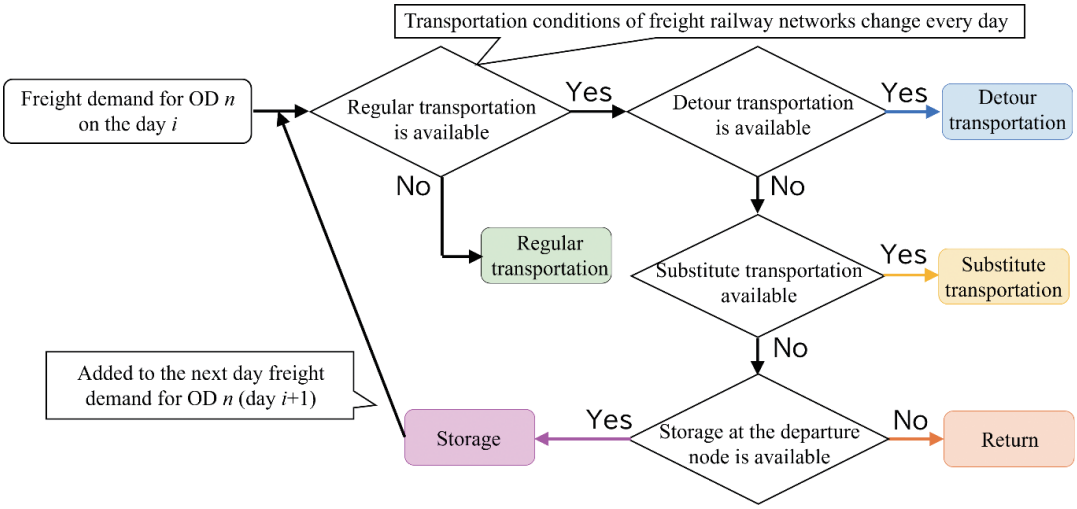

Fig. 4 Flow chart to determine application of each processing method on each day during a restoration period

period.

First, detour transportation is selected for day during a restoration period that meet two conditions found using optimization calculations: maximizing the sum of freight volume transported by detour transportation for each OD on the day that cannot be transported by regular transportation and minimizing total transportation costs for each OD on that day compared to normal times (hereinafter referred to as "detour cost"). Of the two conditions, the former has priority. The cost of regular transportation on the day is the total cost calculated by multiplying volume of freight transported by regular transportation for each OD (number of containers), length of each regular transportation route (km), and unit cost of railway transportation (yen/number of container-km). The detour cost on a day is calculated in the same way. The unit cost of railway transportation is given in advance. Since regular transportation has a priority, processing capacities of nodes and railway links that can be used in detour transportation use surplus capacities after regular transportation has been carried out, and this is one of the constraints in this calculation.

Secondly, substitute transportation is applied when two conditions are met following optimization calculations: maximizing total freight volume transported by substitute transportation for each OD on days where detour transportation is not possible and minimizing total transportation cost for each OD on the day compared to normal times (hereinafter referred to as "substitute cost"). Of the two conditions, the former has priority. Substitute transportation cost is calculated in the same way as regular transportation. However, railway sections and road sections on substitute transportation routes are distinguished, and the unit cost of railway transportation and road transportation are also distinguished. The unit cost of road transportation (yen/number of containers-km) is given in advance. In general, the unit cost of road transportation is higher than railway transportation, so this study also sets the unit costs accordingly.

The processing capacities of nodes and railway links that can be used in substitute transportation use surplus capacities after detour transportation has been carried out, and this is one of the constraints in this estimation.

Finally, storage during a restoration period is applied when freight demand for an OD on a day where substitute transport is not possible. The freight is then stored at its origin node as much as possible. The stored freight demands are added to the next day's volume for that OD on. Storage cost is the total cost calculated by multiplying freight volume stored in each origin node and the unit cost of storage (number of containers/day). The unit cost is given in advance. As shown in Table 2, each node has its own upper limits of storage volume per day, and all freight above this limit for each OD is returned to shippers. The penalty for returning to shippers is the sum of costs calculated by multiplying freight quantities returned for each OD (number of containers) and the unit cost of return (yen/number of containers). The unit cost of return is given in advance.

3.2.3 Estimation of DV and TC

DV is estimated as the sum of freight volume transported by regular transportation, detour transportation, and substitute transportation during a restoration period. TC is estimated as the sum of restoration costs, detour costs, substitute costs, storage costs, and return costs during a restoration period.

3.3 Verifying accuracy of estimation method

To verify the accuracy of the estimation method, DV for a case when the freight railway network was actually damaged by a past natural disaster was calculated and compared with the actual DV at that time. The actual data of freight transportation at that time was provided by JR Freight. Here, since there was no actual TC data at that time, accuracy of TC estimation cannot be directly verified. However, as mentioned above, restoration costs are calculated by multiplying the sum of cumulative numbers of restoration workers dispatched to damaged locations and the unit cost of restoration workers, and it does not change depending on the restoration process of the freight railway network. In short, the accuracy of TC estimation is determined by the costs of each freight processing method, and these depend on the estimation accuracy of application of each processing method, that is, the estimation accuracy of DV. Therefore, if DV can be estimated accurately, it can be considered that TC can also be estimated accurately.

The freight railway network in this simulation is shown in Fig. 5. To reduce the scale of the network, areas not directly affected by the disaster were excluded from the network. Moreover off-rail stations and small freight stations were merged into large freight stations nearby. In this case, although no nodes were damaged, multiple railway links were damaged, and it took more than 50 days to restore all of them.

Freight demands for each OD on each day during the restoration period were substituted with an average of the actual volumes of freight for each OD during the two weeks before the disaster occurred.

Since there was no data that clearly indicates the processing capacities of nodes and railway links, these were substituted with values to process enough freight demands when occur in normal times. In addition, since the number of restoration workers sent to damaged nodes and railway links was unknown, a restoration scenario was given based on the actual restoration process.

Figure 6 shows the transition of the estimated DV and the actual DV during the restoration period. Actual freight demands have periodicity on a weekly basis, thus actual DV also has the same periodicity. On the other hand, since the estimated DV is calculated on the basis of freight demands assumed to be constant on each day, it did not have the periodicity as the actual DV. Therefore, the accuracy of the estimated DV was verified by comparing it with the actual DV that smoothed the periodicity by applying a 7-day moving average (the average of a reference day and the three days before and after).

Figure 6 shows that the estimated DV accurately reproduced the actual DV processed with the 7-day moving average, except for the period of long consecutive holidays when freight demands temporarily declined. Therefore, we concluded that the estimation method has high estimation accuracy.

4. Case study to evaluate effects of disaster countermeasures

A case study to evaluate the effects of disaster countermeasures was conducted for past disasters different to the one in Section 3.3. The freight railway network in this case study is shown in Fig. 7. As in Section 3.3, areas not directly affected by the disaster were excluded, and off-rail stations and small-scale freight stations were merged into nearby large-scale freight stations to reduce the scale of the network.

In this case, although no nodes were damaged, multiple railway links were damaged, and it took about two weeks to restore all of them. The disaster countermeasure in this case study was to strengthen substitute truck transportation.

As shown in Fig.7, the sections to be strengthened were five sections connecting stations A and B to station F (Case 1 to Case 5). These are major freight stations in each area. Then, the implementation effects were evaluated for each of the five cases, Case 1 to Case 5, in which the disaster countermeasure was implemented only in one of these sections. Various conditions for estimating each DV and TC for each case were defined in the same way as in Section 3.3.

Actual data of freight transportation used in this case study was provided by JR Freight. Various unit costs such as the unit cost of regular transportation were defined based on published data about freight transportation. Moreover, in Cases 1 to 5, there was no limit to the number of trucks that could be used.

Since strengthening truck substitute transportation is a soft measure that does not require large-scale capital investments, the main components of the ICs were truck lease costs, driver costs, fuel costs, and miscellaneous costs. Here, these costs except miscellaneous costs are proportional to the lease period and defined to be included in the unit cost of road transportation, that is, included in the DC. In addition, since the implementation period of the substitute truck transportation in this case study is a short period of about two weeks and the amounts would not change significantly in each case, the miscellaneous costs were defined as sufficiently small amounts and did not affect the evaluation results.

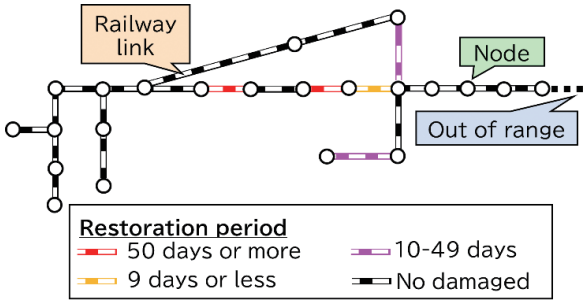

Fig. 5 Freight railway network in the case study

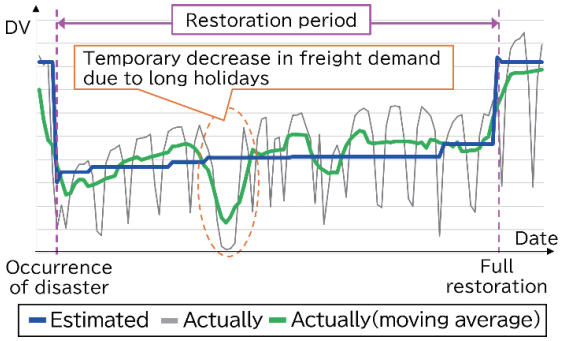

Fig. 6 Transition of the estimated DV and the actual DV

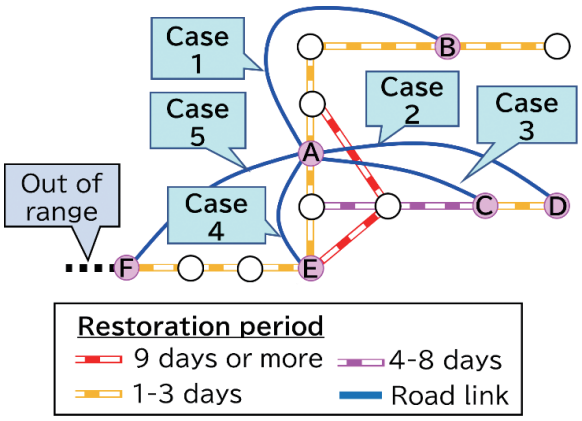

Fig. 7 Freight railway network in this case study

Figure 8 shows the estimated DV and TC in each case. Case 0 means the case that no disaster countermeasures have been implemented (status quo). The DV was improved in Case 3, Case 4, and Case 5, with greatest improvement in Case 5. Considering only the maintenance of a volume of freight transported in the event of a disaster, Case 5 was the best disaster countermeasure. However, in case 5, since the TC increased, considering the maintenance of business continuity of freight railway operators as well, it was not the best disaster countermeasure. The reason for this result is assumed that the volume of freight transportation was maximized by truck substitute transportation whose unit cost is higher than that of railways, between stations A and F where a large volume of freight was transported over a long distance.

Both the DV and TC were improved only in Case 3. Considering both the maintenance of transported freight volume and the maintenance of business continuity of freight railway operators, Case 3 was the best and only effective disaster countermeasure.

From the above results, we concluded that the evaluation meth-

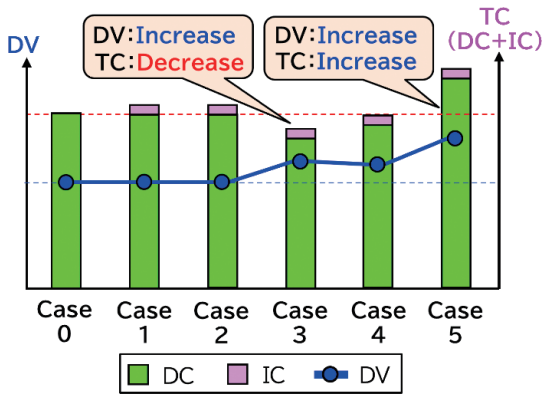

Fig. 8 Estimation result of the case study

od can provide useful information to help railway freight operators decide which disaster countermeasures are needed and in which order of priority.

5. Conclusion

This study aimed to offer support to railway freight operators making decisions about disaster countermeasures. The following results were obtained:

- A method for evaluating the impact of disaster countermeasures was developed. This method is based on indices obtained from comparing differences in DV and TC in cases where disaster countermeasures have and have not been implemented.
- A method for quantifying DV and TC was developed. This method was based on estimated results of restoration processes implemented on freight railway networks and processing methods applied on each day of a restoration period.
- The quantification method was demonstrated to have high estimation accuracy by comparing reproduced DV calculated with past disaster data with actual DV at that time.
- The results of the case study showed that the evaluation method can effectively evaluate the effects of disaster countermeasures in terms of both maintaining freight transportation volume and business continuity in the event of a disaster.

Future efforts and issues are as follows:

- To obtain more accurate and realistic evaluations of the effects of disaster countermeasures, work will be carried out to expand and refine disaster conditions and freight railway networks by improving the estimation method.
- A system that implements these methods will be developed to automate a series of calculations related to the evaluation.
- Since disaster countermeasures are expected to be effective over a medium to long term, the evaluation method will be improved so that the effects of disaster countermeasures can be evaluated for all disasters that are expected to occur within a certain period in the future.
- Expansion of the evaluation method will be studied so that effects of disaster countermeasures for passenger transportation can be evaluated.

References

[1] Muraki, Y., Takahashi, K., Ieda, H., "A Reliability Analysis of Nationwide Transportation Network against Earthquake Risk," *Infrastructure planning review*, No. 16, 1999 (in Japanese).

[2] Harada, T., Ono, T., Kurauchi, F., Takagi, A., "Benefit Evaluation of Disaster Reduction Capability of Road Network," *Proceedings of JSCE D3*, Vol. 73, No. 2, pp. 109-123, 2017 (in Japanese).

[3] Okuda, D., Nakagawa, S., Watanabe, T., Suzuki, T., Fukasawa, N., "Methods for Evaluating Implementation Effects of Disaster Countermeasures for Railway Networks (Part 1) ," presented at the *Japan Society of Civil Engineers 2022 Annual Meetings*, Kyoto, Japan, September 14-16, 2022 (in Japanese).

[4] Watanabe, T., Okuda, D., Nakagawa, S., Suzuki, T., Fukasawa, N., "Methods for Evaluating Implementation Effects of Disaster Countermeasures for Railway Networks (Part 2)," presented at the *Japan Society of Civil Engineers 2022 Annual Meetings*, Kyoto, Japan, September 14-16, 2022 (in Japanese).

Authors

Daiki OKUDA
Senior Researcher, Data Analytics Laboratory, Information and Communication Technology Division
Research Areas: Transportation Planning, Transportation Economics

Takuya WATANABE
Assistant Senior Researcher, Data Analytics Laboratory, Information and Communication Technology Division
Research Areas: Transportation Planning, Geospatial Analysis

Shingo NAKAGAWA
Senior Researcher, Data Analytics Laboratory, Information and Communication Technology Division
Research Areas: Transport Behavior Analysis, Operations Research

Takamasa SUZUKI, PH.D.
Senior Researcher, Data Analytics Laboratory, Information and Communication Technology Division (Former)
Research Areas: Transport Planning, Demand Forecasting

Noriko FUKASAWA
Senior Chief Researcher, Head of Data Analytics Laboratory, Information and Communication Technology Division
Research Areas: Transportation Behavior Analysis

Evaluation of Delay Mitigation Measures based on Delay Propagation Scores and Affected Passenger Numbers

Taketoshi KUNIMATSU **Aiko KUNISAKI** **Kosuke NAKABASAMI**
Transport Operation Systems Laboratory, Signalling and Transport Technology Division

In recent years, train delays have become one of the most serious problems affecting rail transportation in Japan. Although timetable planners try to improve punctuality by modifying current timetables, they have few means to determine how to increase train running time supplements or station dwelling time supplements. In this research, we developed a method for evaluating train delays based on their propagation range. We also proposed an evaluation method which takes into passenger perspectives. We applied these methods to timetable changes on existing railway lines and confirmed that the proposed methods can identify which trains are critical for measures to be effective and improve overall punctuality of the railways.

Key words**:** *delay propagation, punctuality, passenger flow, running time supplements, dwell time supplements*

1. Introduction

Train delays and their subsequent impact on many other trains on a daily basis are a problem many railways face today. Direct trains which run through several lines are particularly affected, since once a train is delayed on a certain line, numerous other trains on many lines may be affected for a long time. Because such widespread delays may cause inconvenience to large numbers of passengers, maintaining punctual transportation service is a priority for railway companies.

Nowadays, railway companies try to improve punctuality by analyzing the state of train operations on a daily basis and modifying current train timetables by increasing running time / dwelling time supplements. Today, delay data for every train and station on daily bases is recorded and accumulated in train control systems. Railway companies statistically analyze this data to know the state of delays. One of the conventional methods used to analyze train delay data is constructing a chromatic diagram. It is a kind of a train diagram, colored according to mean values or medians of train delays for a certain period. This diagram helps easily identify and distinguish which points (a set of train, station, and arrival or departure) are prone to delay on a daily basis. However, little is known about how timetables can be adjusted to improve punctuality. That is, it is unclear where countermeasures, such as increasing running time/ dwelling time margins, should be aimed to improve punctuality of the whole line efficiently. In addition, since only the number of train delays is calculated for each train and station, this information does not clearly show the number of passengers affected, or the degree of inconvenience caused by the delay.

In this research, we first focused on delay propagation, instead of length of delay. We developed a method for evaluating delay propagation for train delay data, by counting points where delays occurred as the result of the delay propagation from a certain point. This was called the "Delay Propagation Score (DPS)." DPS is constructed on the idea that, when a delay at a certain point propagates widely to many points, if we can eliminate the delay at that point, punctuality of the line can be increased efficiently. Then, we developed a second evaluation method called "Affected Passengers (AP)." That estimates the number of passengers arriving at their destination station behind schedule due to train delays at the target point. AP is calculated by using passenger data collected by automatic ticket gates in addition to recorded delay data. Each passenger's train journey both with and without delays is estimated. By comparing the two journeys, the number of passengers arriving at their destination station behind schedule can be specified.

We applied both the evaluation methods to three railway lines having different features, like single/double tracks, or main line/commuter line. We picked up the sets of trains and stations for which calculated DPS or AP were significantly large. After we discussed the results with a timetable planner for the target line, we found that the timetable planner also thought that countermeasures for delays should be implemented for these trains and stations to improve punctuality. In addition, at the next timetable change, the timetable was modified to increase running time /dwell time supplements at target points. After the timetable change, we confirmed that punctuality at the points were largely improved.

In section 2, we describe procedures and problems in timetabling to improve punctuality. Details of two evaluation methods are described: for DPS in section 3 and for AP in section 4. After that, we show the results in which the two methods were applied to an actual line in section 5. Finally, we summarize the conclusion in section 6.

2. Train delays and timetabling

2.1 Train delays

Train delays can be divided into two categories [1]. One is "large-scale delays," caused by operational disruptions such as passenger related accidents or signal failures. The other is "small-scale delays," caused by an extension of train dwelling time at stations due to heavy congestion. To cope with small-scale delays, countermeasures, such as increasing time supplements, tend to be taken in a case of timetable changes. In this research, we developed new evaluation methods for those small-scale delays.

In some cases, a small-scale delay may propagate to an extremely wide area and extend over a long period of time. In fact, as shown in Fig. 1, there was a case in which a local train on main line Q, departing from St. A, was delayed because there was a route conflict between a delayed arrival train on branch line P. The delay of this local train in turn propagated to a limited-express train scheduled to pass the station, and trains on the single track line R were delayed due to the direct route of the delayed limited-express train.

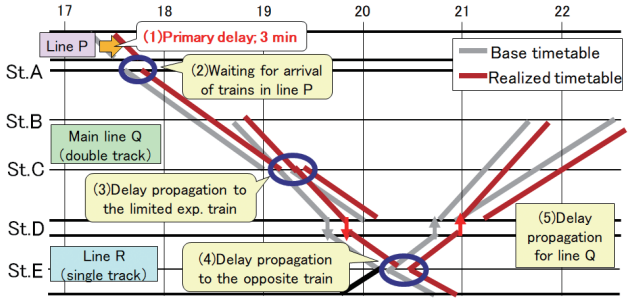

Fig. 1 Wide propagation of train delay

Then, another limited-express train for the other direction was delayed as it waited for the limited-express train. Finally, another limited-express train for the other direction propagated the train delay on main line Q again. In this case, although the length of the delay was only between 2 min. and 5 min., the secondary propagated delays continued for more than 4 hours. To cope with such wide propagation of train delays, it is important to find the point of primary delay, and understand its propagation range.

2.2 Timetabling and countermeasures for delays

Timetable planners plan countermeasures for train delays, however doing so is very time consuming, because it involves the following 5 tasks: 1) finding train delays, 2) analyzing the causes, 3) planning countermeasures, 4) estimating the effects of countermeasures, and 5) validating the timetable change. One of the most difficult tasks in this process is pinpointing and selecting effective points for applying countermeasures. This task requires great amount of timetable planning experience. Drafts of countermeasures also have to be compared quantitatively. In addition, since increasing time margins may reduce speed and frequency or service, they must be minimized. Moreover, planners must examine train operations on site multiple times and qualitatively explore the tradeoffs of each countermeasure before selecting one, which impacts their productivity.

2.3 Related work

In the case of small-scale delays, several methods have been already proposed. For example, a chromatic diagram visualizes train delay trends over a certain period [2]. A method for detecting delay propagation paths by correlation rules has also been proposed [3]. These methods can help timetable planners in their work, such as: 1) finding train delays, 2) analyzing the causes, 4) estimating effects of countermeasures, and 5) validating the timetable change. However, for 3) planning countermeasures, these methods are not enough. That is, even if we understand current train delay conditions on a target line, this insight does not help decisions about how to modify current timetables. For example, we still do not know which trains or stations in the timetable should be changed, nor why applying a countermeasure for one train may be more effective than applying it to another. In addition, since the evaluation results from these methods are summarized as trains or stations, they do not tell us how many passengers are affected by the train delays in question.

Nevertheless, there is research which evaluates the effect of train delays from a passenger perspective by means of disutility values, including transfer failures [4]. Another method estimates the total volume of passengers or sum of delays caused by operational disruptions using smart card data [5]. These methods evaluate the impact of delays from a passenger perspective. However, they only calculate the total impact of a delay over a whole day: they do not tell us how much each delay point contributes to the overall delay. As such, these methods cannot support timetable planning countermeasures. In other words, they do not offer the insight required to know which point of delay, out of many, countermeasures should be aimed to achieve greatest effectiveness.

2.4 Objectives and requirements of the research

This research develops evaluation methods which satisfy the following requirements:

- Evaluation can be done using several days of recorded train delay data;
- Immediate understanding of the delay conditions represented by the evaluation results;
- Representation of train delay propagation range;
- Estimation of countermeasure effect;
- Representation of the number of passengers affected by the delay.

3. Delay propagation score (DPS)

3.1 Objectives and basic ideas

This section introduces the “Delay Propagation Score (DPS)” which is used instead of length of delay to identify individual trains or stations where countermeasures such as increasing time supplements will effectively lead to better punctuality over an entire line. DPS is defined as the number of points over which the target delay is propagated, for example the target train’s delayed arrival at the next station, or delayed arrival of the following train at the same station. In Fig. 2, train 1M has a primary delay of 5 min at Station B as indicated by point 1. The delay propagates to trains and stations, and arrival or departure sites across 28 points. The DPS for point 1 is therefore calculated to be 28. On the other hands, another train 9M has a primary delayed of 7 min at St. B, as indicated by point 2. The delay propagates to trains, stations and arrival or departure sites across 12 points. The DPS for point 2 is thus calculated to be 12. In this case, although the delay is longer for point 2 than point 1, the DPS is higher for point 1 than point 2. This indicates that a delay at point 1 has an overall greater effect on punctuality of the line than point 2. In addition, if delays at point 1 are avoided, this will prevent delays across 28 points, which covers more points than if point 2 delays are avoided, which would only prevent delays across 12 points. Therefore, it can be said that, to improve the overall punctuality of trains on this line efficiently, it is better to take countermeasures for point 1, instead of point 2. Therefore, by calculating the DPS, we can identify the points where countermeasures should be

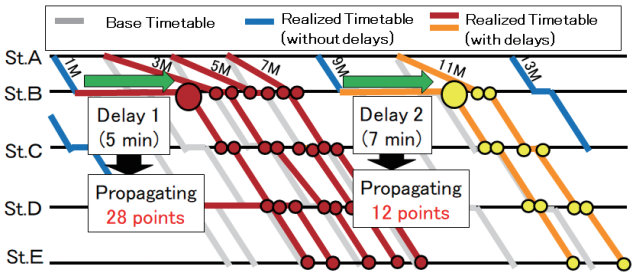

Fig. 2 Definition of delay propagation score

taken to optimize their effectiveness.

Railway timetable planners know that these problematic points which lead to wide propagation of train delays need to be targeted with countermeasures as a priority, because delays are eliminated not only at that point, but also across a large number of other points. Therefore, DPS is an evaluation method which follows timetable-planning practice.

3.2 Evaluation procedure

DPS can be calculated as follows. First, we prepare data about the base timetable and recorded delay data, in which arrival and departure delays of every train and station for everyday are recorded. Following this, records for train, station, and arrival or departure delays which exceed a certain delay threshold are extracted. At the same time, a range of propagation for each point of delay is specified by the method described in the next section. Second, by counting the number of delay points within the specified range, DPS for the day for that point is calculated. Finally, we take medians of DPS for several days for each set of train, station, and arrival or departure. We define that as the median DPS. When there is no train delay at a certain point on a certain day, we set 0 for DPS on the day for that point.

In the case of disruptions due to passenger related accidents or emergency passenger assistance, both length and propagation range of delay increase, and DPS is also significantly higher than usual. Because our main target is small-scale delays, this kind of data on the day with operational disruptions should not be included. However, this type of disruption can happen at different locations and time periods, so it is not appropriate to exclude all recorded data for disrupted days, because this limits the available data for analysis. This is why we use DPS medians instead of mean values, to exclude inappropriate data.

3.3 Specification of propagation range

The propagation range of a certain point of delay is determined as follows: First, we take a certain point of delay, and search for neighboring points of delay in the "downstream" area of the target delay. If the delay at the neighboring point is not greater than the length of delay at the target point, then the neighboring point delay is considered as a point of propagation of the original (target point) delay.

The "downstream" area means areas satisfying the following conditions: *Tmin* stands for the actual minimum headway on the target line, which is set by adding a margin which takes into account variations in running time.

(1) When the target point is train arrival:
- Departure of the target train from the target station;
- Arrival of the following train to the target station;
(only in case when the following train arrives within *Tmin*)

(2) When the target point is train departure:
- Arrival of the target train to the next station;
- Arrival of the following train to the target station using the same track as the target train;
(only when the following train arrives within *Tmin*)
- Departure of the succeeding train from the target station;
(only when the following train departs within *Tmin*)

(3) When the target point is train arrival on a single track line:
- Departure of the oncoming train from the target station;
(only when oncoming train departs within *Tmin*)

In Fig. 2, when we set *Tmin* as 3 min, and when the arrival of train 1M at St. C (point 3) is delayed for 4 min, the delay at point 1 is considered to propagate to point 3. Similarly, when the arrival of train 3M at St. B (point 4) is 2 min after the departure of train 1M, and delayed for 3 min, the delay at point 1 is considered to propagate to point 4.

Then, we specify the area of reachable points of the target point i, by crossing the neighboring point which is considered to have a propagated delay. We denote the set of points as E(i). E(i) is the propagation range of target delay i. DPS can be calculated by counting the number of points inside E(i). As described in the previous sections, we take medians of DPS in the target period.

4. Affected passengers (AP)

4.1 Objectives and basic ideas

This section describes the method for evaluating "Affected Passengers (AP)" for evaluating the magnitude of train delays from a passenger perspective. The basic idea is that AP stands for the number of passengers arriving at their destination station behind schedule due to a delay at the target point. In section 3, DPS evaluates the range of delay propagation by sets of train, station, and arrival or departure. However, DPS cannot reflect the number of passengers on the target train. As a result, both heavily congested trains during peak hours, and less occupied trains running in suburban areas may be evaluated as being the same, if they have a similar delay. In the case of AP, by using passenger data collected by automatic ticket gates, the number of passengers affected by a delay on the target train can be determined. So, AP is an evaluation from the viewpoints of passengers.

4.2 Evaluation procedure

The procedure for calculating AP is as follows [6]. In addition to the collected data described in 3.2, we also gather passenger data from automatic ticket gates. It is enough for us to prepare passenger data for a standard day.

First, using the methods described in 3.2, we determine the delay points and propagation range of the delays. Then, we estimate what the passenger journeys would be with no delay by using base timetable data and passenger data. This is called the "planned journey" below. Similarly, we estimate each passenger journey on the target day including train delays, by using base timetable data, recorded delay data, and passenger data. This is called "actual journey" below.

Next, we determine which passengers arrived at their destination station behind schedule. That is, we compare the planned journey and actual journey of each passenger. If the arrival time at the destination station in the actual journey is later than the planned journey, this is considered to be behind schedule due to the delay. For example, in Fig. 3, passenger P takes train 1M from St. A to St. B. Passenger Q travels from St. A to St. C, taking train 1M and 3M by transferring at St. B. On the target day, only train 1M is delayed for 5min., and train 3M is not delayed at all. Passenger P arrives at St. B 5 min. behind the schedule. Passenger Q, on the other hand, arrives at St. C with no delays, because they managed to catch the connection at St. B despite the delay with 1M. In this case, only passenger P is affected by the delay of train 1M. So, in this case, AP is calculated as 1.

Then, we link each affected passenger to a point of a train delay

by the method described in the next section. After that, we count the number of passengers linked inside the propagation range of the target set of train, station and arrival or departure. This is calculated as AP on the target day. Finally, we take medians of AP for all target days. Note that, if there was no delay at the target point on a day, AP is considered as 0.

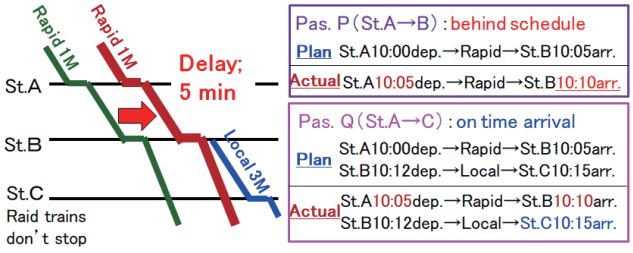

Fig. 3 Specification of passengers behind the schedule

4.3 Passenger delay linking to train delay

In this section, we describe a method for linking passengers to train delays. Linking is only conducted in cases described below because passenger delays are caused by train delays, except in cases when passengers fail to transfer at intermediate stations.

- When the arrival of a train at the passenger's final destination station in the planned journey is delayed on the target day, they are linked with the arrival of a train at that station;
(Except the arrival of trains which passengers cannot board due to delays of other trains in the transferring station);
- When the arrival of a train at a passenger's destination station on their actual journey is delayed on the target day, they are linked with the arrival of a train at that station.

5. Test application on actual lines

5.1 Outline of the target line

The target railway line was double track with limited express trains, rapid trains, and local trains running on it. To confirm the appropriateness and usefulness of the proposed methods, they were applied for analyzing recorded delay data both before and after the timetable change.

5.2 Data and conditions

We prepared base timetable data and recorded delay data for weekdays during the month both before and after the timetable change. Recorded delay data included the length of arrival or departure delays in minutes for every set of train and station. When we calculate the DPS, if a set of train, station, and arrival or departure had a delay more than 1 min it was counted as a delay point. When we calculated AP, we counted passengers arriving at their destination station more than 1 min behind the schedule. In addition, we set *Tmin* as 3 min considering the minimum headway on the target line.

5.3 Length of train delay before timetable change

At first, we visualized train delay conditions before the timetable change using the conventional method. In Fig. 4, the train diagrams are colored according to the median length of departure delay for each train and station. Train lines colored deep blue indicate trains without any delay (0 min), while deep red indicates trains with long delays, and green indicates the middle. From this, it is clear that many trains were delayed on a daily basis. However, it is difficult to determine which countermeasures should be taken.

It seems to be effective to take measures for trains with long delays, indicated by red or orange lines and black circles in Fig. 4. However, on many days, these are not primary delays. Primary delays often occur on trains and stations within the red circles. As a result of delay propagation, the delays of trains inside the black circles become longer. In this case, it is more efficient for us to take measures aimed at trains within the red circles than those within the black circles. However, the conventional method does not consider delay propagation, and the method does indicate which points should be targeted to optimize the countermeasures.

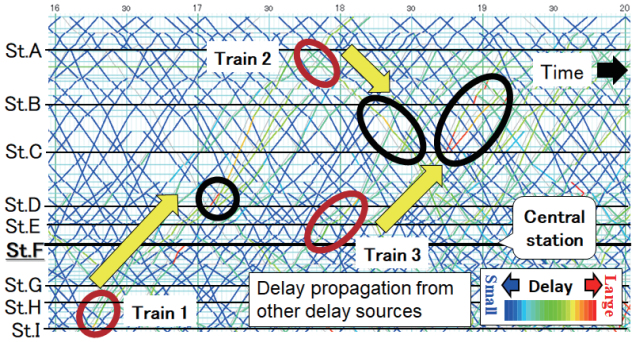

Fig. 4 Length of delay (before timetable change)

5.4 Results after applying DPS

Next, we calculated the median value of DPS for each train and station by using recorded delay data before the timetable change. Fig. 5 illustrates this by adding the DPS to the colored diagram.

Comparing Fig. 4 with Fig. 5, it is clear that DPS easily detects the problematic trains which lead to wide propagation of delay. In particular, trains and stations within the red circles in Fig. 4 are clearly highlighted by the DPS in Fig. 5. Therefore, mitigating these delays with countermeasures can prevent many other delays.

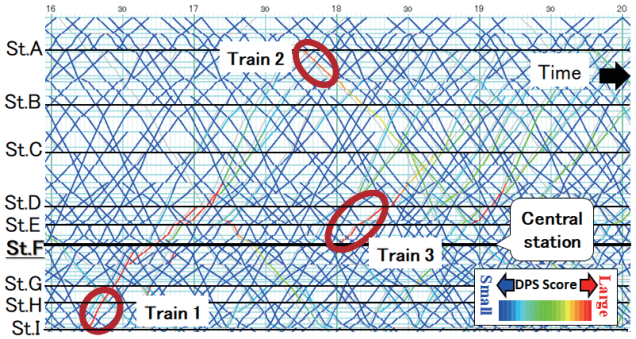

Fig. 5 DPS Score (before timetable change)

5.5 Results applying AP

We calculated the median values of AP using delay data and passenger data before the timetable change. Figure 6 illustrates this by coloring the diagrams according to the AP score.

Comparing Figs. 4, 5 and 6, it is clear that there are relatively fewer points with high AP scores than those showing long delays, or a high DPS scores. That is, lines of train 1 and 3 around St. F and train 2 around St. A are green or yellow. This means they have relatively high AP scores. For trains 1 and 3 around St. F, this is because St. F is a central station with a high volume of passengers. This means that to optimize delay mitigation, countermeasures should target train 1 or 3 around St. F, rather than sections around other stations. This would significantly reduce the number of delayed passengers.

On the other hand, train 2's delay around St. A led to several passengers have their departure delayed from St. A before arriving at St. B or St. C. In addition, train 2's delay propagated to numerous other trains running between St. F and St. I. This led to the delay of passengers boarding trains from St. F. That is why the AP scores for train 2 around St. A is relatively large.

Timetable planners for this line had already identified that trains 1 and 2 were critical before we got the results of evaluation. So, it can be said that DPS or AP scores are effective for identifying trains for which countermeasures would be most effective.

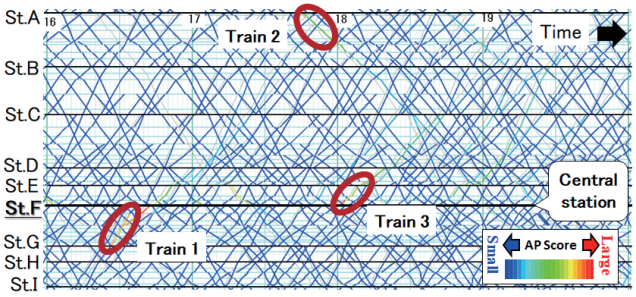

Fig. 6 AP Score (before timetable change)

5.6 Length of train delay after timetable change

Based on the evaluation results above, when considering the next timetable change, the following countermeasures were adopted:

- In the case of train 1, since primary delays tend to occur on the railway lines before St. I, the timetable on that line was adjusted to decrease delayed arrivals of train 1 at St. I.
- Train 2 departure delays from St. A however, tend to occur when trains from other railway lines arrive with a delay at St. A. In addition, train 2 delays tend to increase between St. A and St. B due to heavy congestion. Therefore, the departure track for train 2 from St. A was changed, and it was given extra dwelling time supplements for the journey between St. A and St. B.

The lengths of delays after the timetable change are shown in Fig. 7. Comparing Fig. 4 with Fig. 7 shows that train 1 and train 2 delays were almost eliminated. At the same time, secondary train delays caused by train 1 and train 2 were also prevented. This indicates that the countermeasures above seem to be effective. On the other hand, in the case of train 3, no countermeasures were taken. Figure 7 shows however, that although delays for train 3 were mitigated, some remained and these delays propagated to following trains around St. C.

After the timetable change, Covid-19 significantly changed the volume of passengers on the target line. However, because there were some differences in the delays comparing train 1 and train 2 with train 3, the countermeasures in the timetable change were considered to be effective. In this way, we confirmed the appropriateness and usefulness of DPS and AP.

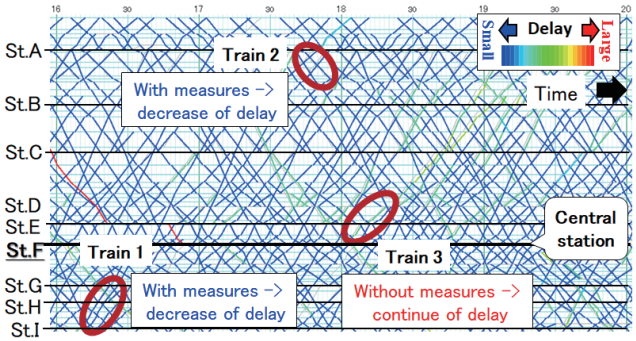

Fig. 7 Length of delay (after timetable change)

6. Conclusions

In this research, we developed two methods to evaluate train delays to optimize current timetable adjustments and improve punctuality. DPS is calculated by counting sets of train, station, and arrival or departure within a propagation range. DPS is an index which stands for the propagation range of the target delay. AP, on the other hand, estimates the number of passengers arriving late at destination due to the delay. AP is an index which evaluates train delays from a passenger perspective.

By applying DPS and AP to an actual railway line, we confirmed that both indices can determine the sets of trains and stations which timetable planners consider to be problem points. Moreover, after adjusting timetables at the identified points we confirmed it was possible to mitigate train delays across a whole line. We therefore conclude that the proposed methods are useful for modifying timetables to improve punctuality. In addition, we confirmed these methods on two other railway lines with different features.

In future, we are going to extend the proposed methods to specify the range of delay propagation, or to evaluate passenger perspectives. For example, we are going to apply the methods to train rescheduling, or to evaluate the impact of decreases in train frequency.

References

[1] Ministry of Land, Infrastructure, Transport and Tourism, "Future vision of railways in Tokyo metropolitan area," *Report of the Transport Policy Council*, No. 198, 2016 (in Japanese).

[2] Yamamura, A. et. al, "Identification of Causes of Delays in Urban Railways," *Proceedings of 13th International Conference on Railway Engineering Design and Optimization*, 2012.

[3] Kono, A. et. al, "Identification of causes and propagation of delays using association rules," *Proceedings of IEE annual meeting*, 2017 (in Japanese).

[4] Takeuchi, Y. and Tomii, N., "Robustness Indices based on Passengers' utilities," *Proceedings of 7th World Congress of Railway Research*, 2006.

[5] Tsunoda, F. et. al, "A Study for Quantification Method of Passenger's Influence by Railway Accident with Transport IC Card," *IPSJ Transactions on Database*, Vol. 6, No. 3, pp. 187-196, 2013 (in Japanese).

[6] Kunimatsu, T. et. al, "Evaluation of Train Delay from the Viewpoints of Affected Passengers," *IEEJ Trans. Industrial Applications*, Vol. 142, No. 5, 2022 (in Japanese).

Authors

Taketoshi KUNIMATSU, Ph.D.
Senior Researcher, Transport Operation Systems Laboratory, Signalling and Transport Technology Division
Research Areas: Train Operation Modeling, Passenger Flow, Simulation

Aiko KUNISAKI
Researcher, Transport Operation Systems Laboratory, Signalling and Transport Technology Division
Research Areas: Energy Friendly Driving, Scheduling, Life Estimation of Electronic Devices

Kosuke NAKABASAMI, Ph.D.
Assistant Senior Researcher, Transport Operation Systems Laboratory, Signalling and Transport Technology Division
Research Areas: Big Data Analysis, Train Timetabling, Passenger Flow, Simulation

Summaries of Papers in RTRI REPORT (in Japanese)

Adhesion Increase Method for Shinkansen Vehicles under Snowfall in Winter

Shinichi SAGA, Hua CHEN, Junji MATSUNO
(Vol.37, No.5, 1-8, 2023.5)

When railway vehicles running in snowy weather, the adhesive force between rails and wheels is lower than that in rainy weather. For this reason, we studied a method to increase the adhesion coefficient focusing on the temperature and the roughness of wheel treads. From the viewpoint of minimizing specification changes, improving the material of current adhesive blocks through full-scale dynamo bench testing, we developed new adhesive blocks. An optimal wheel tread cleaner operation pattern was found through running tests using an actual vehicle in winter. The execution of the pattern contributes to improving adhesive effect such as increasing roughness of wheel treads, and suppressing sliding in the high-speed range, in addition to reducing temperature rise and improving wear resistance.

Seismic Response Analysis of Piers with Foundation Composed of Micropiles and Soilbags

Tatsuya DOI, Yoshitaka MURONO, Feng ZHANG
(Vol.37, No.5, 9-17, 2023.5)

In this paper, the authors propose a new type of foundation, which is a combination of micropiles and soilbags. The proposed foundation is characterized by laying soilbags on the pile head and constructing structures on the soilbags. The effects by the adoption of the new foundation are expected to result in the omission of joint between piles and a footing, a reduction of diameter of piles, and a reduction of response acceleration of structures. In this study, seismic response evaluation method for the proposed structure with actual size was constructed to compare the seismic responses of the proposed foundation with those of pile foundation under the different conditions of input acceleration.

Natural Frequency Identification Method for a Substructure in Railway Bridges and Viaducts

Kazunori WADA, Kimitoshi SAKAI
(Vol.37, No.5, 19-27, 2023.5)

We have proposed a method to identify the natural frequency of a single structure from data obtained by measuring the vibration of railway bridges and viaducts. In the method, the natural frequency of a single structure can be theoretically calculated by using undamped natural frequencies and natural modes of a whole structure. The eigenvalue analysis was performed, and it was shown that the natural frequency of a single structure can be identified by the proposed method.

Effect of Decarburisation Layer Removal by Rail Grinding on Reduction of Microcrack Formation

Yoshikazu KANEMATSU, Naotaka UEHIGASHI, Motohide MATSUI, Hidenori NISHIMURA
(Vol.37, No.5, 29-36, 2023.5)

This study aims to understand the effect of decarburisation on microcrack formation on rails using a twin-disc test and an on-site (laying) test. Test pieces with and without decarburisation were compared under the same test conditions using a twin-disk test. The results show that decarburisation affects the formation of microcracks and a plastic flow. Furthermore, we investigated the decarburisation effect on the microcrack formation using test pieces taken from actual tracks. The comparison between the test pieces with and without a decarburized layer showed that the crack density of rails on the unground was 2.7-5.7 times higher than that of rails ground at a cumulative tonnage of 23 MGT.

Development and Performance Evaluation of Rail Fastening System Using Non-metallic Materials Applied to Its Main Components

Atsushi MATSUO, Tadashi DESHIMARU, Yoshihiro MASUDA, Minoru SUZUKI
(Vol.37, No.5, 37-43, 2023.5)

A function of rail fastening systems is to fasten rails to supporting structures such as sleepers. In addition to the fastening function, rail fastening systems are designed to provide a certain level of electrical insulation to prevent rail current from leaking through the supporting structures to the earth. Despite this, some cases have been reported where the electrical insulation of rail fastening systems has deteriorated in some installation environments, resulting in transport disturbances such as ground faults and short circuits. Thus, we studied the applicability of resin materials to the rail fastening components to prevent the reduction of the electrical insulation. Based on the results of this study, we produced a prototype of a rail fastening system using resin components and evaluated its performance. In order to evaluate the performance of the prototype, design reference values were proposed to reflect the influence of the installation environment on the material strength. The performance evaluation of the prototype based on the proposed value confirms that the prototype has the performance to be installed on a conventional rail track.

A Method of Internal Resistance Estimation by Measuring Ripple During Charging for Traction Battery

Kosuke OSAKI, Yoshiaki TAGUCHI, Aruto WATANABE
(Vol.37, No.6, 1-6, 2023.6)

We developed a method for calculating internal resistance using RMS values of ripple voltage and current in charging process of a traction battery. Since the ripple voltage and current contain many frequency components, we built frequency filters to measure required components. The internal resistance calculated by the developed method was found to be in good agreement with the value calculated using the main frequency components of ripple. The results showed the effectiveness of the developed method using frequency filter and RMS value meter which are small and inexpensive devices.

Application of Phased Array Ultrasonic Testing Method to Flaw Detection in Vehicle Bogie Parts

Kazunari MAKINO
(Vol.37, No.6, 7-14, 2023.6)

An imaging technology by the phased array ultrasonic testing (PAUT) was applied to bogie part inspection, targeting welded parts in bogie frames and wheel seats in axles. Regarding bogie frames, the superiority of PAUT was confirmed in detecting inclined surface flaws, and the effect of paint thickness on the echo height was clarified. When PAUT was applied to an actual bogie frame, the results of flaw detection were visualized clearly, demonstrating the effectiveness of PAUT in bogie frames. Regarding axles, when PAUT was applied to a wheel seat using shear-wave and longitudinal-wave angle beam inspection techniques, flaws on the wheel seat were detected and visualized in a wheel-fitted state.

Centrifugal Model Test and Design Method for Temporary Retaining Wall Using Soil Buttress as Displacement Suppressing

Takashi USHIDA, Takuya NAKASHIMA, Takaki MATSUMARU, Takashi NAKAYAMA, Nobutaka HIRAOKA, Kazuya ITOH

(Vol.37, No.6, 15-21, 2023.6)

It is important to suppress displacement of the temporary retaining wall when excavating in the urban area nearby existing structures. Soil buttresses have economic advantages compared to struts, such as in large-scale excavation works. On the other hand, an issue in designing such temporary retaining walls is that displacement suppressing mechanisms need to be considered by FEM and so on. In this paper, we clarified the displacement suppressing mechanism of soil buttresses by centrifuge model tests with excavation. Cutout shaped soil buttresses were proposed based on the test knowledge. Furthermore, we proposed the design method of temporary retaining wall using soil buttresses as displacement suppressing.

Effect of Opening on Walls of Small Train Sheds on Wind Pressure and Response of Shed Members

Daisuke ISHIKAWA, Katsuyuki SHIMIZU, Minoru SUZUKI, Yuhei NOGUCHI

(Vol.37, No.6, 23-29, 2023.6)

It is important to evaluate wind loads on small train sheds constructed on passenger platforms, since they have relatively light mass and both upper and lower surfaces of the roofs are exposed to the wind. In this study, we examined differences in forms, conducting wind tunnel tests and frame analyses using the results of the wind tunnel test for small train sheds, and obtained following findings. Wind loads acting on the sheds and the stress of their members produced by the wind loads are smaller as the openings formed in the back walls of the sheds are larger, but do not depend on the arrangement of the openings.

Development and Construction of Ground Reinforcement Method using Pressurized Injection Materials

Yuki KURAKAMI, Susumu NAKAJIMA, Masaaki BEPPU, Sumio YAZAKI

(Vol.37, No.6, 31-37, 2023.6)

A new method called Lotus anchor method was developed as a soil reinforcement method using grout injection. This method enables the construction of ground reinforcement with a diameter larger than the boring diameter (φ=115 mm) by pressurized injection. The pullout test results showed that the design pullout resistance can be evaluated reasonably by setting the reinforcement diameter twice than that of the boring diameter. It was also confirmed that the proper management of injection pressure and injection rate secures the safe construction. Using an ordinary soil reinforcement method, we need a large construction machine with a width of about 5 m, on the other hand only a width of just 3 m will do for the developed method. Moreover, using a small core drill machine, required space can be reduced to just a 1 m site width, allowing the construction in narrow place.

Improvement of Flame Retardancy of Seat Cushion Materials for Railway Vehicles Using Intumescent Flame Retardant

Tadashi TOYOHARA, Sho YAMANAKA, Mikiya ITO

(Vol.37, No.7, 1-7, 2023.7)

In order to further improve the flame retardancy of seat materials in railway vehicle, the authors investigated to apply new flame-retardant to it. During the selection stage of flame retardants, their attention was focused on intumescent flame-retardants. The intumescent flame-retardant expands and produces char foam during burning state, and the produced char foam plays a role of protect shield against rapid flame spread. Various test pieces using the flame-retardants were prepared to confirm their characteristics. As a result of the cone calorimeter fire tests, it was found that insertion of a resin containing intumescent flame-retardants into the existing seat cushions can improve the flame retardancy.

Application of Cylindrical Roller Bearings with Ribs to Gear Units of Railway Vehicles

Ken TAKAHASHI, Daisuke SUZUKI, Yoshiaki OKAMURA, Takafumi NAGATOMO

(Vol.37, No.7, 9-15, 2023.7)

Helical gears are commonly used in the gear units of railway vehicles in Japan, and a bearing type used for the gear units is a tapered roller bearing. In order to prevent seizure of bearings, this study examined the use of cylindrical roller bearings with ribs that allow a certain degree of axial displacement of inner rings and outer rings, and compared its performance with that of a conventional structure using tapered roller bearings through various rotating tests. The results showed that the temperature rise immediately after the start of rotation and torque of the pinion shaft are lower in cylindrical roller bearings with ribs than those in tapered roller bearings, through the rotation tests using an actual gear unit.

Estimation Method of Lateral Vibration Acceleration of Car Body used for Safety Evaluation of Railway Vehicles against Crosswind

Hiroyuki KANEMOTO, Yu HIBINO

(Vol.37, No.7, 17-25, 2023.7)

The critical wind speed of overturning is often evaluated by the "RTRI's detailed equation." In the equation, the lateral vibration inertia force of car bodies is considered as one of acting forces affecting overturning, and the lateral vibration acceleration is assumed from past running test results. This paper shows that the critical wind speed of overturning can be accurately calculated by using simulation results of the lateral vibration acceleration occurring at the center of gravity of a car body under strong crosswinds. In addition, a new method is proposed to estimate the lateral vibration acceleration using track alignment data.

Wind Tunnel Test to Reproduce Track Surfaces Flow When Shinkansen Trains Pass for Ballast and Ballast Screen Scattering

Tatsuya INOUE, Takashi NAKANO, Atsushi IDO

(Vol.37, No.7, 27-33, 2023.7)

Air flow is induced on track surfaces when Shinkansen trains pass. To prevent ballast scattering due to the air flow, measures such as ballast screens are taken on track surfaces. However, considering the extension of Shinkansen lines and speed up in the future, it is necessary to improve current measures to prevent ballast scattering and to develop new ballast screens. Therefore, in this study, we developed the wind tunnel test method that can be used for research on measures to prevent ballast scattering and studied the scattering phenomenon of objects.

Concept of Storage Battery Electricity Source Railcar and Power Supplying Procedure to e.m.u.-trains

Masamichi OGASA

(Vol.37, No.7, 35-41, 2023.7)

Here we propose a concept of a storage battery electricity source railcar to run e.m.u. (electric multiple unit)-trains on non-electrified lines of a middle distance beyond 100 km. This method has advantages in formation possibility as a train and in the total cost of the first few decades in some cases compared to the usual electrification method of a whole line. To embody a battery source car, a circuit configuration and a power supply method when connecting and releasing it to a train has been presented. The procedure of

replacing source cars at a nodal station is also specifically described, while preventing electric shocks.

Examination of Wireless Acceleration Measurement for Ballasted Track

Izumi KURITA, Satoko RYUO, Nagateru IWASAWA, Akiko KONO

(Vol.37, No.7, 43-50, 2023.7)

Railway operators examine dynamic characteristics of ballast vibration using wired sensors. To improve the efficiency of maintenance works in track. In terms of prevent disconnection of sensor cables during tamping works, wireless measurement of the vibration is required. In this research we discussed specifications of wireless sensors such as an operation pattern and a radio system. We evaluated the wireless characteristics of some buried wireless devices in a ballasted track and confirmed that RSSI which is a wireless indicator exceeds the minimum received sensitivity. Furthermore, we confirmed the behavior of the buried sensors during a road railer run over them.

Relationship between Levels of Urban Railway Services and Residential Location Preference in Metropolitan Area

Takuya WATANABE, Noriko FUKASAWA, Daiki OKUDA, Takamasa SUZUKI

(Vol.37, No.7, 51-58, 2023.7)

Railway operators are endeavoring to improve levels of their services in order to gain more residents nearby. However, no studies have been focusing on the relationship between levels of railway services and residential location preference in metropolitan areas. In this study, a questionnaire survey was conducted in metropolitan areas. We applied a conjoint analysis to the collected data and quantified the effect of each transportation services on residential location preference. We confirmed that the effects can be compared quantitatively among each transportation service. The result of the analysis suggests that railway services that affect residential location preference differ depending on resident's attributes such as where they live and/or how often they use rail.

Relevant Standards and Requirements of Coordination between Electric Railcars and Power Supply Systems

Takayuki NAKAMURA, Masataka AKAGI, Satoru HATSUKADE

(Vol.37, No.7, 59-64, 2023.7)

Coordination between electric railcars and power supply systems is essential to introduce new technical elements in onboard power conversion systems. The standard on the coordination is established in Europe, whereas there are no documents to rely upon in Japan. The European standard, which operates as a mandatory standard concretely designates technical specific values. Therefore, understanding the standard is essential of performing business abroad. The standard is also useful for performing business in Japan, in situations such as determination and assessment for new technical elements. Considering these circumstances, this paper explains the requirements regarding the coordination to be also useful for business in Japan.

August 2023 Vol. 64 No. 1 - No. 3

RTRI Develops a Dynamic Gauge and Twist Measurement Device TRACK²er

RTRI developed a dynamic gauge and twist measurement device TRACK²er. This device is capable of measuring track displacement caused by passing trains. Since this device can be mounted on a maintenance vehicle instead of using a track inspection car, it is possible to measure track displacement more easily, with lower cost.

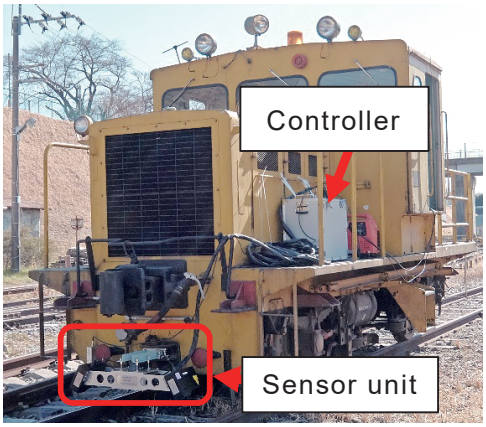

TRACK²er mounted on a maintenance vehicle

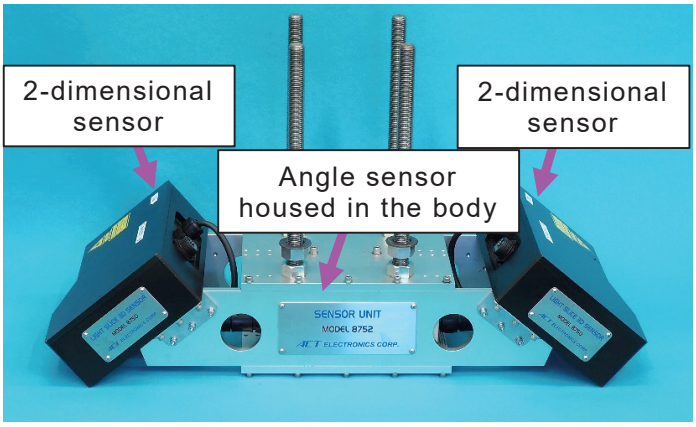

Sensor unit

QUARTERLY REPORT of RTRI

第 64 巻　第 3 号
2023 年 8 月 1 日　発行
監修・発行所：公益財団法人鉄道総合技術研究所
〒 185-8540　東京都国分寺市光町 2-8-38
発行人：芦谷公稔
問い合わせ：鉄道総研広報

Vol. 64, No. 3
Published date: 1 August 2023
Supervision/Publisher: Railway Technical Research Institute
Address: 2-8-38 Hikari-cho, Kokubunji-shi, Tokyo 185-8540, Japan
Issuer: Dr. Kimitoshi ASHIYA
Contact us: Public Relations, Railway Technical Research Institute
Mail Address: rtripr@rtri.or.jp

QUARTERLY REPORT of RTRI

RAILWAY TECHNICAL RESEARCH INSTITUTE

Printed in Japan